NASA/TM–2020-220568/Volume II/Part 2

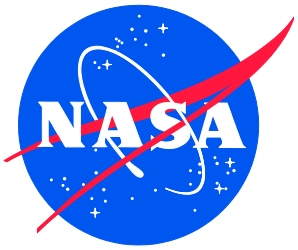

Nondestructive Evaluation (NDE) Methods and Capabilities Handbook

Volume II Appendices —Appendix E Volume 1

Patricia A. Howell, Editor
Langley Research Center, Hampton, Virginia

APPROVED FOR PUBLIC RELEASE

February 2020

NASA STI Program . . . in Profile

Since its founding, NASA has been dedicated to the advancement of aeronautics and space science. The NASA scientific and technical information (STI) program plays a key part in helping NASA maintain this important role.

The NASA STI program operates under the auspices of the Agency Chief Information Officer. It collects, organizes, provides for archiving, and disseminates NASA's STI. The NASA STI program provides access to the NTRS Registered and its public interface, the NASA Technical Reports Server, thus providing one of the largest collections of aeronautical and space science STI in the world. Results are published in both non-NASA channels and by NASA in the NASA STI Report Series, which includes the following report types:

- TECHNICAL PUBLICATION. Reports of completed research or a major significant phase of research that present the results of NASA Programs and include extensive data or theoretical analysis. Includes compilations of significant scientific and technical data and information deemed to be of continuing reference value. NASA counter-part of peer-reviewed formal professional papers but has less stringent limitations on manuscript length and extent of graphic presentations.

- TECHNICAL MEMORANDUM. Scientific and technical findings that are preliminary or of specialized interest, e.g., quick release reports, working papers, and bibliographies that contain minimal annotation. Does not contain extensive analysis.

- CONTRACTOR REPORT. Scientific and technical findings by NASA-sponsored contractors and grantees.

- CONFERENCE PUBLICATION. Collected papers from scientific and technical conferences, symposia, seminars, or other meetings sponsored or co-sponsored by NASA.

- SPECIAL PUBLICATION. Scientific, technical, or historical information from NASA programs, projects, and missions, often concerned with subjects having substantial public interest.

- TECHNICAL TRANSLATION. English-language translations of foreign scientific and technical material pertinent to NASA's mission.

Specialized services also include organizing and publishing research results, distributing specialized research announcements and feeds, providing information desk and personal search support, and enabling data exchange services.

For more information about the NASA STI program, see the following:

- Access the NASA STI program home page at *http://www.sti.nasa.gov*

- E-mail your question to help@sti.nasa.gov

- Phone the NASA STI Information Desk at 757-864-9658

- Write to:

NASA STI Information Desk
Mail Stop 148
NASA Langley Research Center
Hampton, VA 23681-2199

NASA/TM–2020-220568/Volume II/Part 2

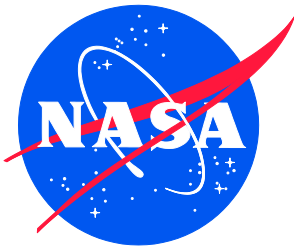

Nondestructive Evaluation (NDE) Methods and Capabilities Handbook

Volume II Appendices —Appendix E Volume 1

Patricia A. Howell, Editor
Langley Research Center, Hampton, Virginia

National Aeronautics and
Space Administration

Langley Research Center
Hampton, Virginia 23681-2199

February 2020

The material is based upon work supported by NASA under Award Nos. NNL09AA00A and 80LARC17C0004

Available from:

NASA STI Program / Mail Stop 148
NASA Langley Research Center
Hampton, VA 23681-2199
Fax: 757-864-6500

Table of Contents

E.1 Specimen #1: NASA-S-D 1
E.1.1 Method: Pulse-Echo Ultrasound Testing (PEUT) 1
E.2 Specimen #2: NASA-S-MP 5
E.2.1 Method: X-ray Computed Tomography (XCT) 6
E.2.2 Method: Pulse-Echo Ultrasound Testing (PEUT) 14
E.2.3 Method: Single-Sided Infrared (IR) Thermography (SSIR) 17
E.2.4 Method: Through-Transmission Infrared Thermography (TTIR) 20
E.3 Specimen #3: NASA-S-HP 23
E.3.1 Method: X-ray Computed Tomography (XCT) 24
E.3.2 Method: Pulse-Echo Ultrasound Testing (PEUT) 29
E.3.3 Method: Single-Sided Infrared (IR) Thermography (SSIR) 33
E.3.4 Method: Through-Transmission Infrared Thermography (TTIR) 37
E.4 Specimen #4: NASA-W5D – Not Tested 40
E.5 Specimen #5: NASA-W-20D – Not Tested 40
E.6 Specimen #6: NASA-W-35D – Not Tested 41
E.7 Specimen #7: NASA-W-IL-20D – Not Tested 41
E.8 Specimen #8: NASA-W-IL-20D – Not Tested 41
E.9 Specimen #9 – Not manufactured 41
E.10 Specimen #10: NASA-W-5MP 41
E.10.1 Method: X-ray Computed Tomography (XCT) 41
E.11 Specimen #11: NASA-W-IL-5D 47
E.11.1 Method: X-ray Computed Tomography (XCT) 48
E.12 Specimen #12: NASA-W-20MP 54
E.12.1 Method: X-ray Computed Tomography (XCT) 55
E.13 Specimen #13: NASA-W-IL-20MP 62
E.13.1 Method: X-ray Computed Tomography (XCT) 63
E.14 Specimen #14 – Not manufactured 66
E.15 Specimen #15 – Not manufactured 66
E.16 Specimen #16: NASA-RP-01D 66
E.16.1 Method: Guided Wave Ultrasound (GWUT) 67
E.17 Specimen – Not Manufactured 73
E.18 Specimen #18: NASA-RP-10D 73
E.18.1 Method: Guided Wave Ultrasound (GWUT) 74
E.19 Specimen #19: NASA-RP-20D 80
E.19.1 Method: Guided Wave Ultrasound (GWUT) 80
E.20 Specimen #20: NASA-RP-40D 86
E.20.1 Method: Pulse-Echo Ultrasound Testing (PEUT) 87
E.20.2 Method: Guided Wave Ultrasound (GWUT) 89

List of Figures

Figure E.1-1. Photographs of Specimen #1: NASA-S-D. 1
Figure E.1-2. PEUT setup in Test-Tech scanning tank. 2
Figure E.1-3. PEUT C-scans at 500 kHz for Steps 1–6. 3
Figure E.1-4. PEUT C-scans at 1.0 MHz for Steps 1–6. 4
Figure E.1-5. PEUT C-scans at 2.25 MHz for Steps 1–6. 5
Figure E.2-1. Photographs of Specimen #2: NASA-S-MP. 6
Figure E.2-2. XCT system components. 6
Figure E.2-3. Slice direction nomenclature 7
Figure E.2-4. Microfocus XCT system showing orientation of Specimen #2: NASA-S-MP 8

Figure E.2-5. Side view (X-Normal) of flat-bottom holes with filler. 9
Figure E.2-6. Profile of specimen displaying porosity defect. 9
Figure E.2-7. Y-normal direction view of specimen showing two locations of porosity in plane with each other. 10
Figure E.2-8. (Left) Manual porosity detection of Y-normal slice showing two locations of porosity. (Right) Porosity detection by CNN Segmentation of same slice. 12
Figure E.2-9. 3D visualization of the detected damage on Specimen #2 (NASA-S-MP). 13
Figure E.2-10. The developed CNN Model detected damage illustration on Specimen #2 (NASA-S-MP), which were missed by SMEs. 13
Figure E.2-11. PEUT setup in Test-Tech scanning tank. 14
Figure E.2-12. PEUT C-scans at 500 kHz for Steps 1–6. 15
Figure E.2-13. PEUT C-scans at 1.0 MHz for steps 1–6. 16
Figure E.2-14. PEUT C-scans at 2.25 MHz for Steps 1–6. 17
Figure E.2-15. Single-sided thermography schematic. 18
Figure E.2-16. Photo of single-sided thermography setup. 18
Figure E.2-17. Single-sided thermography image of Specimen #2. 19
Figure E.2-18. Intensity curve showing heat dispersion over time for each step of Specimen #2. 20
Figure E.2-19. TTIR schematic. 21
Figure E.2-20. Photo of TTIR setup. 21
Figure E.2-21. Temperature curve showing the dispersion of heat over time during image capture of Step 1. 22
Figure E.2-22. Histogram showing frequency of thermal diffusivity values. 22
Figure E.2-23. Image of thermal diffusivity post processing. 23
Figure E.3-1. Photographs of Specimen #3: NASA-S-HP. 24
Figure E.3-2. XCT system components. 24
Figure E.3-3. Slice direction nomenclature. 25
Figure E.3-4. Microfocus XCT system showing orientation of Specimen #3: NASA-S-HP. 25
Figure E.3-5. a) XCT scan of specimen #2 viewed from the z-direction. b) XCT scan viewed from the y-direction. 27
Figure E.3-6. XCT scan of Specimen #2 viewed from the x-direction. 27
Figure E.3-7. (Left) XCT scan viewed from the y-normal direction. (Right) Defect detection using CNN segmentation of the same slice. 28
Figure E.3-8. (Left) XCT scan viewed from the z-normal direction. (Right) Defect detection using CNN segmentation of the same slice (NASA-S-HP). 29
Figure E.3-9. PEUT setup in Test-Tech scanning tank. 30
Figure E.3-10. PEUT C-scans at 500 kHz for Steps 1–6. 31
Figure E.3-11. PEUT scans at 1.0 MHz for Steps 1–6. 32
Figure E.3-12. PEUT C-scans at 2.25 MHz for Steps 1–6. 33
Figure E.3-13. Single-side thermography schematic. 34
Figure E.3-14. Photo of single-sided thermography setup. 35
Figure E.3-15. Single-sided thermography image of Specimen #3. 36
Figure E.3-16. Intensity curve showing heat dispersion over time for each step of Specimen #3. 37
Figure E.3-17. TTIR schematic. 38
Figure E.3-18. Photo of TTIR setup. 38
Figure E.3-19. Temperature curve showing the dispersion of heat over time during image capture of Step 1. 39
Figure E.3-20. Histogram showing frequency of thermal diffusivity values. 39
Figure E.3-21. Image of thermal diffusivity post processing. 40
Figure E.10-1. Photographs of Specimen #10: NASA-W-5MP. 41
Figure E.10-2. XCT system components. 42

Figure E.10-3. Slice direction nomenclature. 43
Figure E.10-4. CT slices from the y-direction (bottom) and x-direction (top) showing porosity and delaminations within the sample. 44
Figure E.10-5. CT slices from the x-direction (left) and z-direction (right) showing close views of porosity and delaminations within the sample. 45
Figure E.10-6. (Top) XCT scan viewed from the y-normal direction. (Bottom) defect detection using CNN segmentation of the same slice of Specimen #10. 46
Figure E.10-7. Segmentation of a specimen from Figure E.10-5. 47
Figure E.11-1. Photographs of Specimen #11: NASA-W-IL-5D. 48
Figure E.11-2. XCT system components. 48
Figure E.11-3. Slice direction nomenclature. 49
Figure E.11-4. Specimen orientation within the detector. 49
Figure E.11-5. CT slices from the y-direction (bottom) and x-direction (top) showing porosity within the sample. 51
Figure E.11-6. XCT slices from the z-direction showing close views of porosity and within the sample. 52
Figure E.11-7. (Top) X-ray CT slice of specimen #11 in the x-normal view. (Bottom) CNN segmentation of same slice. 53
Figure E.11-8. (Left) X-ray CT slice of specimen #11 in the z-normal view. (Right) CNN segmentation results of same slice. 54
Figure E.12-1. Photographs of Specimen #12: NASA-W-20MP. 55
Figure E.12-2. XCT system components. 55
Figure E.12-3. Slice direction nomenclature. 56
Figure E.12-4. Specimen orientation within the system. 56
Figure E.12-5. CT slices from the y-direction showing porosity and delaminations within the sample. 58
Figure E.12-6. XCT slices from the z-direction showing close views of porosity and delaminations within the sample. 58
Figure E.12-7. XCT slices from the z-direction showing close views of porosity and delaminations within the sample. 59
Figure E.12-8. (Top) XCT slice from the z-normal direction showing porosity and delaminations within the sample. (Bottom) Segmentation of the same slice. 60
Figure E.12-9. (Top) XCT slices from the z-normal direction showing close views of porosity and delaminations within the sample. (Bottom) segmentation of a specimen from XCT slices from the z-normal direction showing the CT slice with both delaminations and porosity within the sample. 60
Figure E.12-10. (Top) XCT slices from the z-normal direction showing porosity and delaminations within the sample. (Bottom) segmentation results of the slice. 61
Figure E.12-11. (Left) CT slices from the y-normal direction showing porosity and delaminations within the sample. (Right) CNN segmentation results showing porosity and delaminations. 61
Figure E.12-12. (Left) CT slices from the x-normal direction showing porosity and delaminations within the sample. (Right) CNN segmentation results showing porosity and delaminations. 62
Figure E.13-1. Photographs of Specimen #12: NASA-W-IL-20MP. 63
Figure E.13-2. XCT system components. 63
Figure E.13-3. Slice direction nomenclature. 64
Figure E.13-4. Specimen orientation within apparatus. 64
Figure E.13-5. CT slices from the y-direction showing porosity and delaminations within the sample. 65
Figure E.13-6. XCT slices from the z-direction showing porosity and delaminations within the sample. 66

Figure E.13-7. XCT slices from the z-direction showing porosity and delaminations within the sample. 66
Figure E.16-1. Photographs of Specimen NASA-RP-01D. (a) overall view, and (b) side view. 67
Figure E.16.-2. Schematic design of the PZT-SLDV system. 67
Figure E.16-3. Experimental setup of the PZT-SLDV system. 68
Figure E.16-4. Experimental setup (a) scanning schematic design of W1 and W2, and (b) 2D area inspection. 69
Figure E.16-5. W1 wavefield on Outside at: (a) 24 μs, and (b) 35 μs. 69
Figure E.16-6. Energy maps of W1 on: (a) outside, and (b) inside. 70
Figure E.16-7. Inspection at bottom edge of W1: (a) wavefield at 28 μs, and (b) energy map within time range 20–30 μs. 70
Figure E.16-8. Energy maps of W2 on: (a) outside, and (b) inside. 71
Figure E.16-9. Energy maps of W2 on inside. 71
Figure E.16-10. Energy maps of C Part on: (a) outside, and (b) inside. 72
Figure E.16-11. Inspection summary of identified defects. 72
Figure E.18-1. Photographs of Specimen NASA-RP-10D. (a) overall view, (b) side view, and (c) specimen setup. 74
Figure E.18-2. Schematic design of the PZT-SLDV system. 75
Figure E.18-3. Experimental setup of the PZT-SLDV system. 75
Figure E.18-4. Experimental setup (a) scanning schematic of outside surface, and (b) scanning schematic design of inside surface. 76
Figure E.18-5. Wavefield at 45 μs of outside surface: (a) actuator at O_1, and (b) actuator at O_2. 77
Figure E.18-6. Wavefield imaging of outside surface: (a) actuator at O_1, and (b) actuator at O_2. 77
Figure E.18-7. Wavefield at 45 μs of inside surface: (a) actuator at O_1, and (b) actuator at O_2. 78
Figure E.18-8. Wavefield imaging of inside surface: (a) actuator at O_1, and (b) actuator at O_2. 78
Figure E.18-9. Inspection summary of identified defects. 79
Figure E.19-1. Photographs of Specimen NASA-RP-20D. (a) overall view, (b) side view, and (c) specimen setup. 80
Figure E.19-2. Schematic design of the PZT-SLDV system. 81
Figure E.19-3. Experimental setup of the PZT-SLDV system. 81
Figure E.19-4. Experimental setup (a) scanning schematic of outside surface, and (b) scanning schematic design of inside surface. 82
Figure E.19-5. Wavefield on inside at 45 μs of outside surface: (a) actuator at O_1, and (b) actuator at O_2. 83
Figure E.19-6. Wavefield imaging of outside surface: (a) actuator at O_1, and (b) actuator at O_2. 83
Figure E.19-7. Inspection results with actuator at O_3: (a) wavefield at 35 μs, and (b) wavefield image. 84
Figure E.19-8. Wavefield on inside at 45 μs of inside surface: (a) actuator at O_1, and (b) actuator at O_2. 84
Figure E.19-9. Wavefield imaging of inside surface: (a) actuator at O_1, and (b) actuator at O_2. 85
Figure E.19-10. Inspection summary of identified defects. 85
Figure E.20-1. Photographs of Specimen #20: NASA-RP-40D. 86
Figure E.20-2. Ultrasonic system components. 87
Figure E.20-3. (a) Surface flaws and (b) near surface void 88
Figure E.20-4. (a) Interior delaminations and (b) back-surface reflection. 89
Figure E.20-5. Photographs of Specimen NASA-RP-40D. 90
Figure E.20-6. Schematic design of the PZT-SLDV system. 90
Figure E.20-7. Experimental setup of the PZT-SLDV system. 90
Figure E.20-8. Experimental setup (a) scanning schematic design of W1 and (b) scanning schematic design of W2. 92
Figure E.20-9. Wavefield on outside at 45 μs: (a) W1, and (b) W2. 92
Figure E.20-10. Energy map of outside surface: (a) W1, and (b) W2. 92

Figure E.20-11. Wavefield on inside at 45 μs: (a) W1, and (b) W2. 93
Figure E.20-12. Wavefield on inside at 45 μs: (a) W1, and (b) W2. 94
Figure E.20-13. Inspection summary of identified defects. 94

List of Tables

Table E.1-1. Equipment settings for 0.5 MHz scan. 2
Table E.1-2. Equipment settings for 1.0 MHz scan. 2
Table E.1-3. Equipment settings for 2.25 MHz scan. 2
Table E.2-1. Data collection settings. 7
Table E.2-2. Equipment settings for 0.5 MHz scan. 14
Table E.2-3. Equipment settings for 1.0 MHz scan. 15
Table E.2-4. Equipment settings for 2.25 MHz scan. 15
Table E.2-5. Equipment settings for SSIR scan. 19
Table E.2-6. Equipment settings for TTIR scan. 22
Table E.3-1. Data collection settings. 26
Table E.3-2. Equipment settings for 0.5 MHz scan. 30
Table E.3-3. Equipment settings for 1.0 MHz scan. 30
Table E.3-4. Equipment settings for 2.25 MHz scan. 30
Table E.3-5. Equipment settings for SSIR scan. 35
Table E.3-6. Equipment settings for TTIR scan. 39
Table E.10-1. Data collection settings. 43
Table E.11-1. Data collection settings. 50
Table E.12-1. Data collection settings. 57
Table E-13-1. Data collection settings. 65
Table E.16-1. Equipment/device specifications. 68
Table E.16-2. Data collection settings. 68
Table E.16-3. Hybrid PZT-SLDV guided wave inspection rating. 73
Table E.18-1. Equipment/device specifications. 75
Table E.18-2. Data collection settings. 76
Table E.18-3. Hybrid PZT-SLDV guided wave inspection rating. 79
Table E.19-1. Equipment/device specifications. 81
Table E.19-2. Data collection settings. 82
Table E.19-3. Hybrid PZT-SLDV guided wave inspection rating. 86
Table E.20-1. Data collection settings. 87
Table E.20-2. Equipment/device specifications. 91
Table E.20-3. Data collection settings. 91
Table E.20-4. Hybrid PZT-SLDV guided wave inspection rating. 95

Nomenclature

μA	Microampere
μm	Micrometer/Micron
μs	Microseconds
1D	One-Dimensional
2D	Two-Dimensional
3D	Three-Dimensional
ABS	Acrylonitrile Butadiene Styrene
ACAD	Air Coupled Acoustic Drive
ACC	Advanced Composites Consortium
ACP	Advanced Composites Project
ACT	Air Coupled Transducer
ADR	Assisted Defect Recognition
AFP	Automated fiber placement
AISI	American Iron and Steel Institution
AMT	Active Microwave Thermography
ANSI	American National Standards Institute
APF	Automated Fiber Placement
ARC	Ames Research Center
ASME	American Society of Mechanical Engineers
ASNT	American Society of Nondestructive Testing
ASTM	American Society for Testing and Materials
ATL	Automated Tape Lay-Up
AWG	Arbitrary Waveform Generator
AWS	American Welding Society
BMS	Boeing Material Specification
BSI	British Standards Institution
BVID	Barely Visible Impact Damage
BW	Back Wall
C	Celsius
CAD	Computer-Aided Design
CAFA	Combined Analytical Finite Element Approach
CCD	Charge-coupled Device
CDRH	Center for Devices and Radiological Health
CFRP	Carbon Fiber Reinforced Polymer
CMOS	complementary metal oxide semiconductor
CNN	Convolutional Neural Network
CO_2	Carbon Dioxide
COPV	Composite Over-Wrap Pressure Vessel
CPV	Composite Pressure Vessel
CR	Computed Radiography
CST	Charge Simulation Technique
CT	Computed Tomography
CTE	Coefficient of Thermal Expansion
DAQ	Data Acquisition
dB	Decibel
dB/in	Decibels Per Inch
DDA	Digital Detector Array
DOF	Degree of Freedom
DR	Digital Radiography
DRC	Digital Radiography Center
ECT	Eddy Current Thermography
EFIT	Elastodynamic Finite Integration Technique

FBH	Flat-bottom holes
FD	Finite Difference
FDA	Food and Drug Administration
FEA	Finite Element Analysis
FEM	Finite Element Method
FEP	Fluorinated Ethylene Propylene
FLIR	Forward-looking Infrared
FMC	Full Matrix Capture
FOD	Foreign Object Debris
FOV	Field of View
ft-lbs	Foot Pounds
GE	General Electric
GHz	Gigahertz
GN_2	Gaseous Nitrogen
gsm	Grams per square meter
GWUT	Guided Wave Ultrasound
Hz	Hertz
ID	Inner Diameter
IDIQ	Indefinite Delivery/Indefinite Quantity
IEC	International Electrotechnical Commission
IML	Inner Mold Line
in	Inch
in/min	Inches per Minute
InSb	Indium Antimonide
ipm	Images per Minute
IR	Infrared
IRT	Infrared Thermography
ISTIS	*In Situ* Thermal Inspection System
J/cm^2	Joules Per Square Centimeter
K	Kelvin
KeV	Kiloelectron Volt
kg	Kilograms
kg/cm^2	kilogram per square centimeter
kHz	Kilohertz
kV	Kilovolts
kW	kilowatt
LaRC	Langley Research Center
LBI	Laser Bond Inspection
LMCO	Lockheed-Martin Company
LPS	Local Positioning System
LST	Line Scanning Thermography
LT	Lock-In Thermography
m^2	Square Meter
m^2/hr	Meters Square per Hour
mA	Miliampere
MECAD	Mechanically Coupled Acoustic Drive
MGBM	Multi-Gaussian Beam Model
MHz	Megahertz
mHz	Millihertz
mK	Millikelvin
mm	Millimeter
MPa	Megapascals
ms	Meter per Second
MS/s	Megasamples/second

msec	Millisecond
MSFC	Marshall Space Flight Center
NAS	National Aerospace Standard
NASA	National Aeronautics and Space Administration
Nd:Glass	Neodymium Glass Laser
NDE	Nondestructive Evaluation
NDI	Nondestructive Inspection
NDT	Nondestructive Test
NEDT	Noise Equivalent Differential Temperature
NGIS	Northrop Grumman Innovation Systems
nm	Nanometer
ns	Nanosecond
OEM	Original Equipment Manufacturer
OML	Outer Mold Line
ONR	Office of Naval Research
OSHA	Occupational Safety and Health Administration
PA	Phased Array
PCA	Principal Component Analysis
PEUT	Pulse Echo Ultrasound
PMC	Polymer Matrix Composite
PML	Perfectly Matched Layer
POC	Point of Contact
PoD	Probability of Detection
PPT	Pulsed-Phase Thermography
psi	Pounds Per Square Inch
PT	Pressure-Sensitive Tape
PTFE	Polytetraflouroethylene (Teflon™)
PVDF	polyvinylidene fluoride
PWI	Plane Wave Imaging
PW-UTC	Pratt Whitney – United Technology Corporation
PZT	Piezoelectric Sensors/Transducer
R&D	Research and Development
RAH	Refresh After Heat
RBH	Refresh Before Heat
RGB	Red, Green, and Blue
RMS	Root Mean Squared
ROI	Region of Interest
RPF	Release Ply Fabric
RSG	Rotated-Staggered Grid
RVE	Representative Volume Element
s	Seconds
SAE	Society of Automotive Engineers
SAFE	Semi-Analytical Finite Element
SAR	Synthetic Aperture Radar
sec	Seconds
SHM	Structural Health Monitoring
SLDV	Scanning Laser Doppler Vibrometer
SMAAART	Structures, Materials, Aerodynamics, Aerothermodynamics, and Acoustics Research and Technology
SME	Subject Matter Expert
SNR	Signal to Noise Ratio
SOFI	Spray on Foam Insulation
SoP	State-of-Practice
sq. ft/hr	square foot per hour

SSFT	Single-Side Flash Thermography
SSIR	Single-Sided Infrared Thermography
SVD	Singular Value Decomposition
TC2	Technical Challenge 2
TDRS	Time Domain Reflectometry Systems
TFM	Total Focus Method
Tg	Glass Transition Temperature
THz	Terahertz
TPS	Thermal Protection System
TSR	Thermographic Signal Reconstruction
TT	Through Transmission
TTIR	Through-Transmission Infrared Thermography
TTUT	Through-Transmission Ultrasound
TWI	Thermal Wave Imaging System
USC	University of South Carolina
UT	Ultrasound
VaRTM	Variation Resin Transfer Molding
VSHM	Visualized Structural Health Monitoring
XCT	X-ray Computed Tomography

Appendix E Individual Test Reports by Specimen (Sections 1-20)

★☆☆	Not Suitable for this Specimen
★★☆	Marginally suitable for this Specimen, or only provides qualitative information
★★★	Highly successful for this Specimen, including quantifiable information

E.1 Specimen #1: NASA-S-D

Structure	Material	Details	Dimensions (inches)	Partners Methods	
Uni-ply (0/90/45)	IM7/8552	Stepped Flat-bottom Hole Panel	14 × 8 × 1.5	NGIS	E.1.1 PEUT

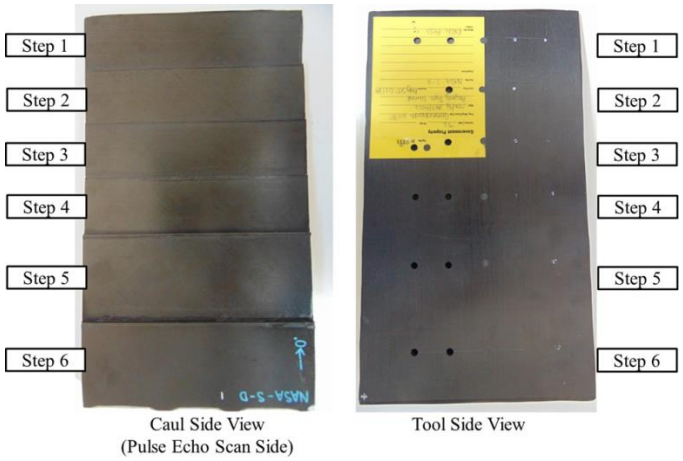

Figure E.1-1. Photographs of Specimen #1: NASA-S-D.

E.1.1 *Method: Pulse-Echo Ultrasound Testing (PEUT)*

E.1.1.1 Partner: Northrop Grumman Innovation Systems (NGIS)

E.1.1.2 Technique Applicability: ★★★

Water-coupled PEUT scans were performed to demonstrate the feasibility of detecting defects in thick carbon-composite laminates on a stepped-thickness panel with back-drilled flat-bottom holes and laminate thickness ranging from 0.1 to 1.0 inch. Scans were performed from the stepped side, since flat-bottom holes were drilled into the flat tool side, to determine detection dependency on both defect depth and diameter. Different frequencies including 0.5, 1.0, and 2.25 MHz were sampled to observe frequency dependence.

E.1.1.3 Laboratory Setup

PEUT scans performed in the Test-Tech 3-axis scanning tank used the water-squirter method. For each panel, use of optimum water nozzle and column diameter achieved optimal signal-to-noise ratio (SNR) and defect detection (if defects existed).

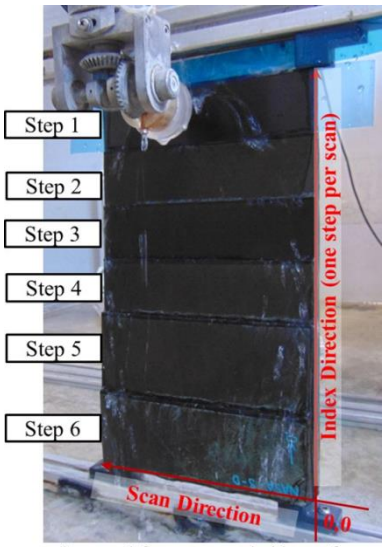

Figure E.1-2. PEUT setup in Test-Tech scanning tank.

E.1.1.4 Equipment List and Specifications:

- Test-Tech 3-axis scanning tank
- Olympus 5077PR Square Wave Pulser/Receiver
- Transducer Frequencies: 0.5, 1.0, and 2.25 MHz

E.1.1.5 Settings

Table E.1-1. Equipment settings for 0.5 MHz scan.

Transducer	Brand	Model	Freq. (MHz)	Element Dia. (in.)	Water Column Dia (in.)			Outer Dia. (in)		
Transmitter	GE	Benchmark	0.5	0.5	0.5					
Pulser/Receiver	PRF	Voltage	Freq. (MHz)		HPF	LPF (MHz)	Rtune	Ttune	Attn	Range
Olympus	Ext	200	0.5		Out	Full BW	N/A	N/A	N/A	N/A
	Gain (dB)	"-8 for Step 1		"-4 for Steps 2,3,4,5,6						

Table E.1-2. Equipment settings for 1.0 MHz scan.

Transducer	Brand	Model	Freq. (MHz)	Element Dia. (in.)	Water Column Dia (in.)			Outer Dia. (in)		
Transmitter	Sonic	IBK I-2	1	0.5	0.375					
Pulser/Receiver	PRF	Voltage	Freq. (MHz)		HPF	LPF (MHz)	Rtune	Ttune	Attn	Range
Olympus	Ext	400	1.0		Out	Full BW	N/A	N/A	N/A	N/A
	Gain (dB)	6 for Steps 1,2,3		9 for Steps 4,5,6						

Table E.1-3. Equipment settings for 2.25 MHz scan.

Transducer	Brand	Model	Freq. (MHz)	Element Dia. (in.)	Water Column Dia (in.)			Outer Dia. (in)		
Transmitter	KB-Aerotech	Alpha	2.25	0.5	0.25					
Pulser/Receiver	PRF	Voltage	Freq. (MHz)		HPF	LPF (MHz)	Rtune	Ttune	Attn	Range
Olympus	Ext	200	2-2.25		Out	Full BW	N/A	N/A	N/A	N/A
	Gain (dB)	6 for Steps 1,2,3,6		10 for Steps 4	14 for Steps 5					

E.1.1.6 Inspection Results

Snapshots of C-scans provided below show internal gates and laminate back-wall gates. Not all defects or back walls were detected for all measured frequencies. At higher frequencies, the thicker laminate was too attenuating. For lower frequencies on thinner laminate, internal and back-wall signals could not be temporally resolved.

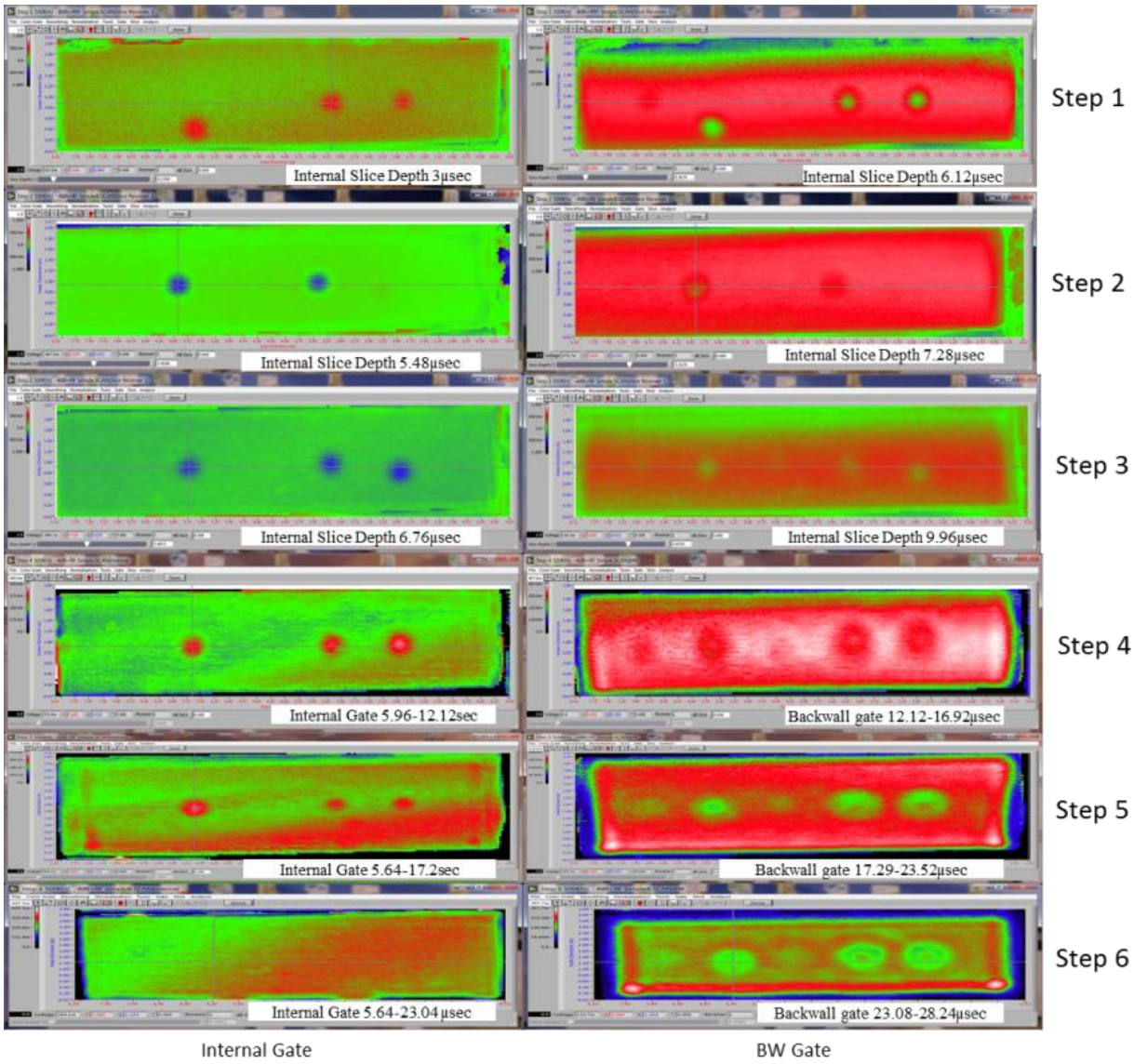

Figure E.1-3. PEUT C-scans at 500 kHz for Steps 1–6. Internal gate (left) and back-wall gate (right) C-scans shown.

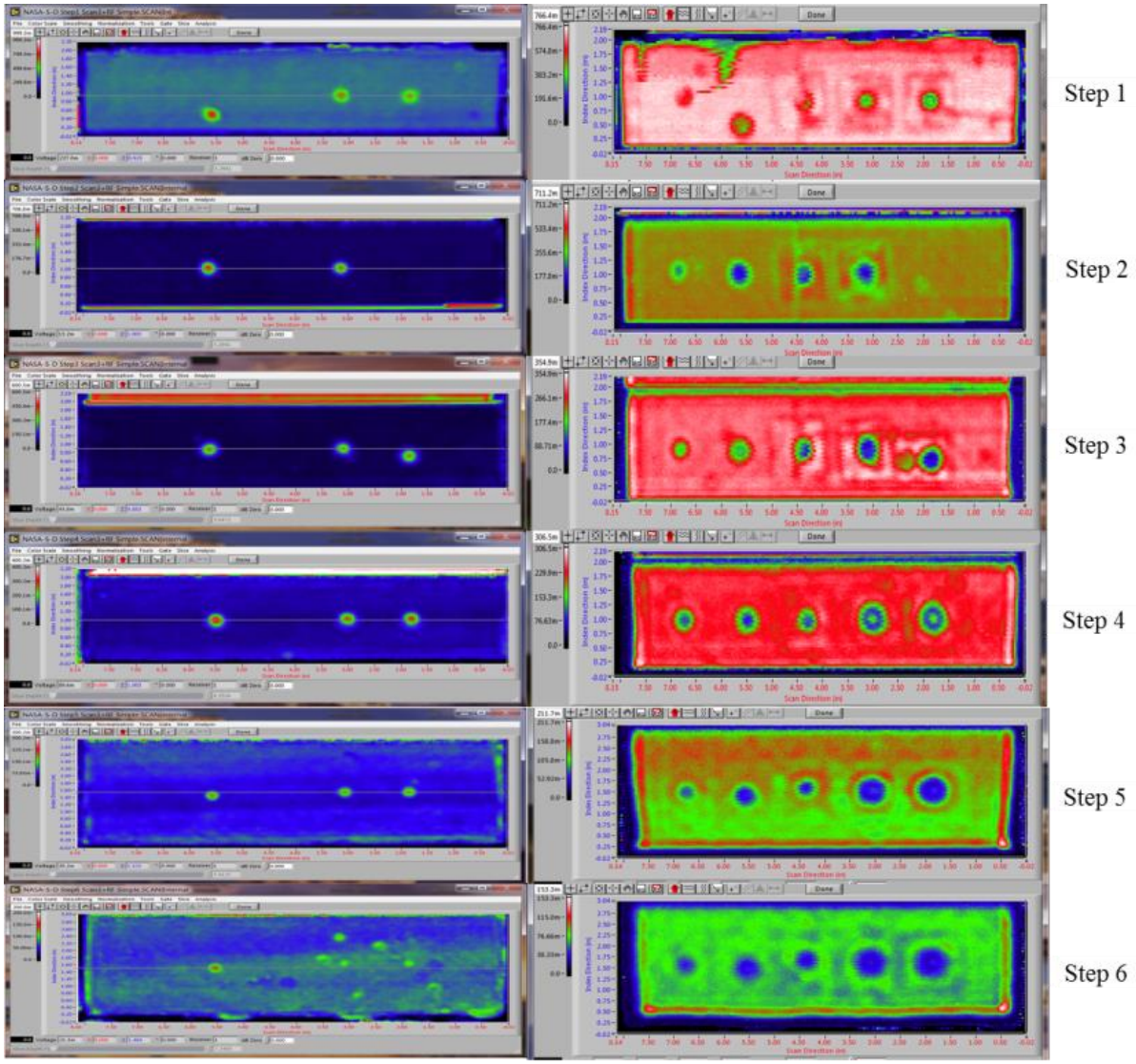

Figure E.1-4. PEUT C-scans at 1.0 MHz for Steps 1–6. Internal gate (left) and back-wall gate (right) C-scans shown.

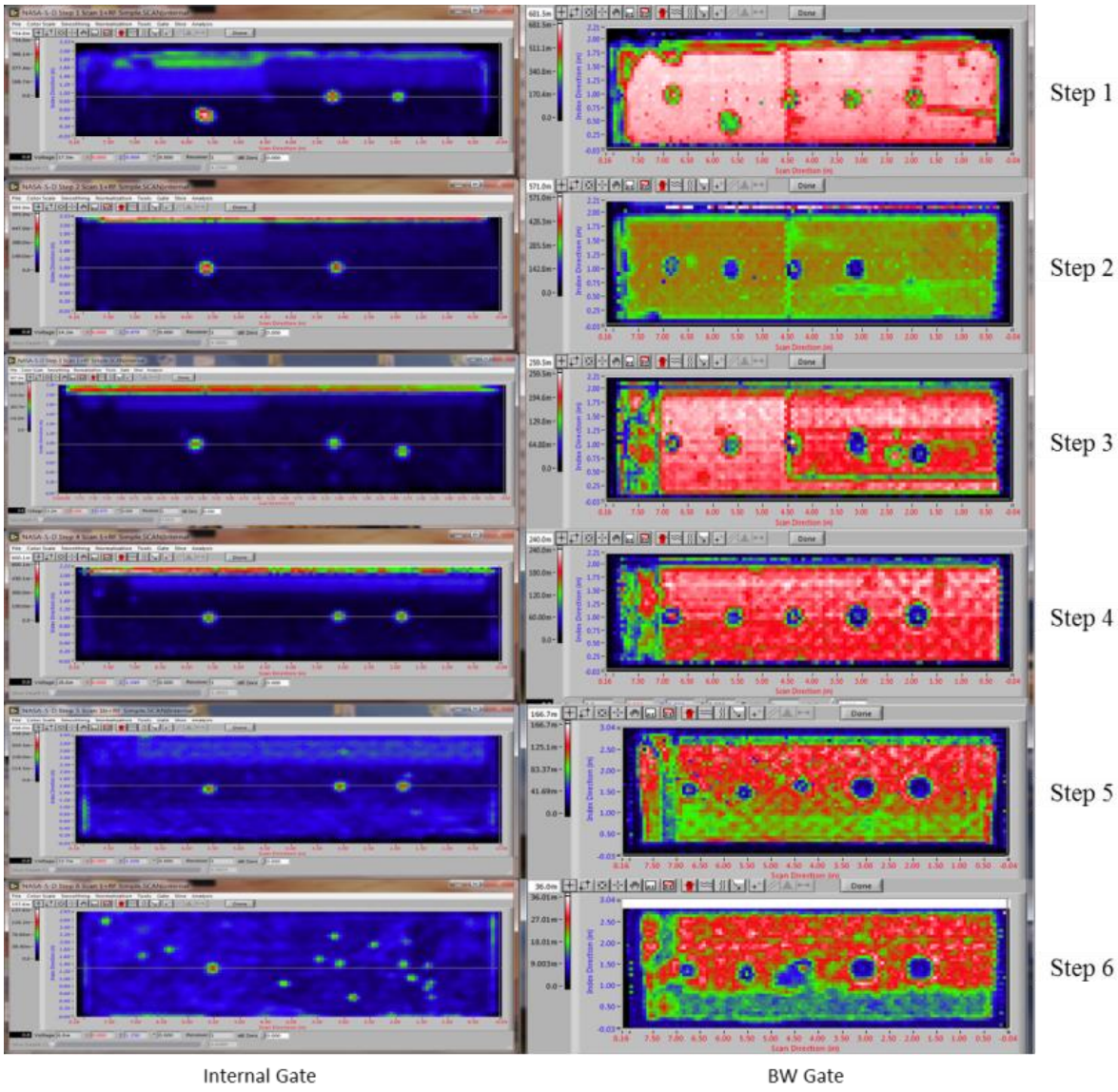

Figure E.1-5. PEUT C-scans at 2.25 MHz for Steps 1–6. Internal sate (left) and back-wall gate (right) C-scans shown.

E.1.1.7 References

[1] Workman, Gary L, and Doron Kishoni. Nondestructive Testing Handbook. Third. Edited by Patrick O Moore. Vol. 7. American Society for Nondestructive Testing (ANST), 2007.

E.2 Specimen #2: NASA-S-MP

Structure	Material	Details	Dimensions (inches)	Partner Methods	
Uni-ply (0/90/45)	IM7/8552	Step wedge with medium porosity Step heights: 0.1-1.0 inch	14 × 8 × 1.5	NASA	E.2.1 XCT
				NGIS	E.2.2 PEUT E.2.3 SSIR E.2.4 TTIR

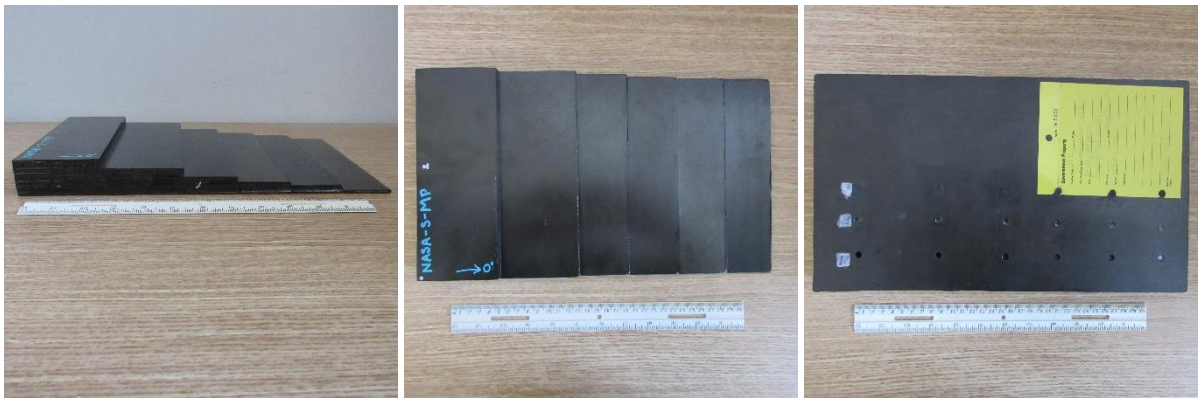

Figure E.2-1. Photographs of Specimen #2: NASA-S-MP.

E.2.1 *Method: X-ray Computed Tomography (XCT)*

E.2.1.1 Partner: NASA

E.2.1.2 Technique Applicability: ★★★

XCT is capable of imaging the medium porosity in this specimen.

E.2.1.3 Laboratory Setup

The microfocus XCT system at NASA LaRC is a commercially available X-Tek (now Nikon Metrology) system designed for high-resolution NDE inspections. The system is an advanced microfocus X-ray system, capable of resolving details down to 5 μm, and with magnifications up to 60X. Supplied as complete, the system is a large-dimension radiation enclosure with X-ray source, specimen manipulator, and an amorphous silica detector, as shown in Figure E.2-2. The imaging controls are housed in a separate control console. The detector, visible behind the specimen in Figure E.2-4b, is a Perkin-Elmer, 16-bit, amorphous-silicon digital detector with a 2000 × 2000-pixel array.

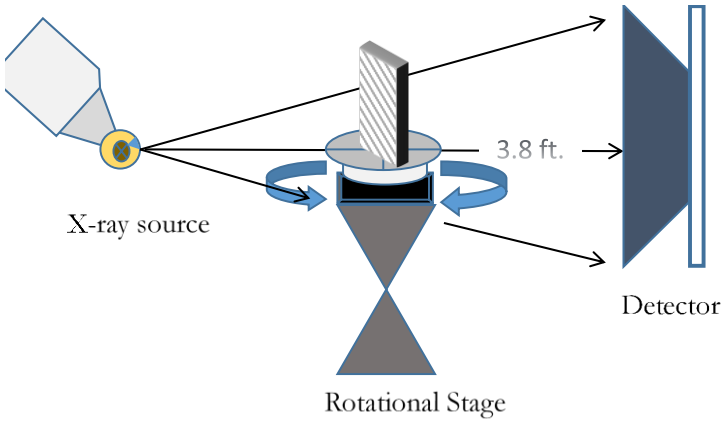

Figure E.2-2. XCT system components.

A consistent Cartesian coordinate system is used to define slice direction, as illustrated in Figure E.2-3. Slices normal to the X-, Y-, and Z-directions are shown in Figure E.2-3a, b, and c, respectively.

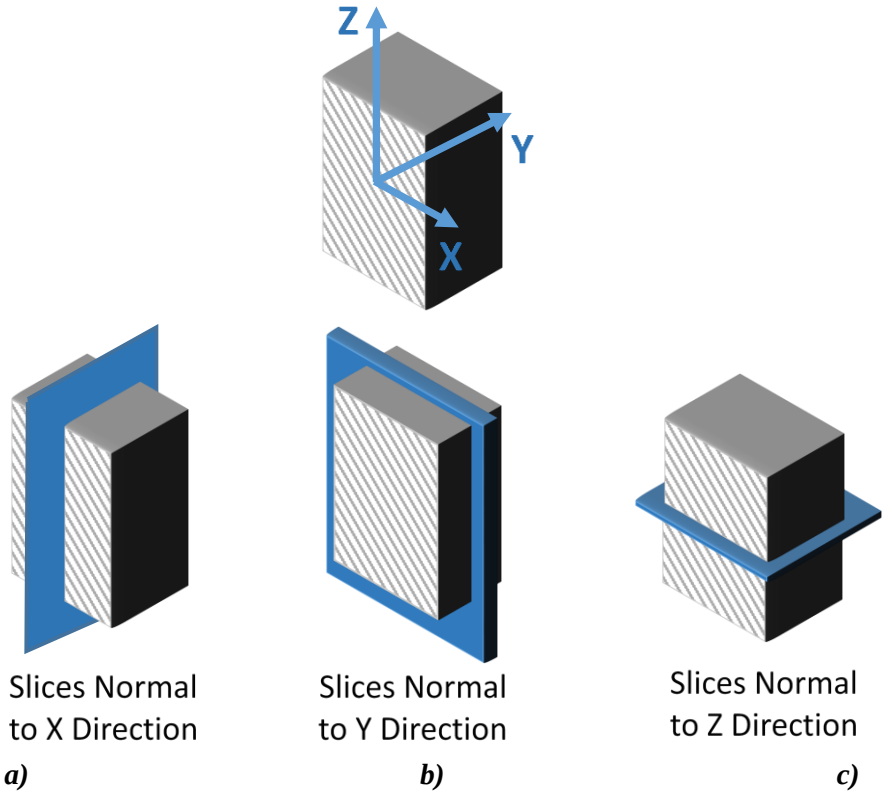

Figure E.2-3. Slice direction nomenclature.

E.2.1.4 Equipment List and Specifications:

X-Tek 225 CT System
225 kV microfocus X-ray source with 5-µm focal spot size
15 or 30 kg Capacity 5-axis fully programmable manipulator
Detector: Perkin Elmer XRD 1621 – 2000 × 2000 pixels with 200 µm pitch
10 µm spatial resolution for specimens 1.5 cm wide
Thin panels 10 × 10 inch – full volume 200 µm spatial resolution

E.2.1.5 Settings

Table E.2-1. Data collection settings.

Source Energy	120 kV
Current	90 µA
Magnification	1.65 X
Filter	NF
# Rotational angles	3142
Exposure time / frame	1.0 sec
Max Histogram Grey Level	22 K
# Averages	8
Resolution (µm)	114.894 µm
Array Dimensions (pixels)	Set 1: 1999 × 362 × 1998 Set 2: 1998 × 686 × 1997

The specimen is placed vertically (rotated about the smallest dimension) on the rotational stage located between the radiation source and the detector, as shown in Figure E.2-4a. In order to image

the bottom portion of the specimen, it is turned upside down and a second set of CT data is collected. The two datasets can then be merged in post-processing. The rotational stage is computer controlled and correlated to the position of the sample. As the sample is rotated the full 360° (~0.11° increments), the detector collects radiographs at each rotated angle as the X-ray path intersects the sample. Three-dimensional (3D) reconstruction of the collection of radiographs produces a volume of data observed along any plane in the volume. The closer the sample can be placed to the X-ray source, the higher the spatial resolution can be obtained.

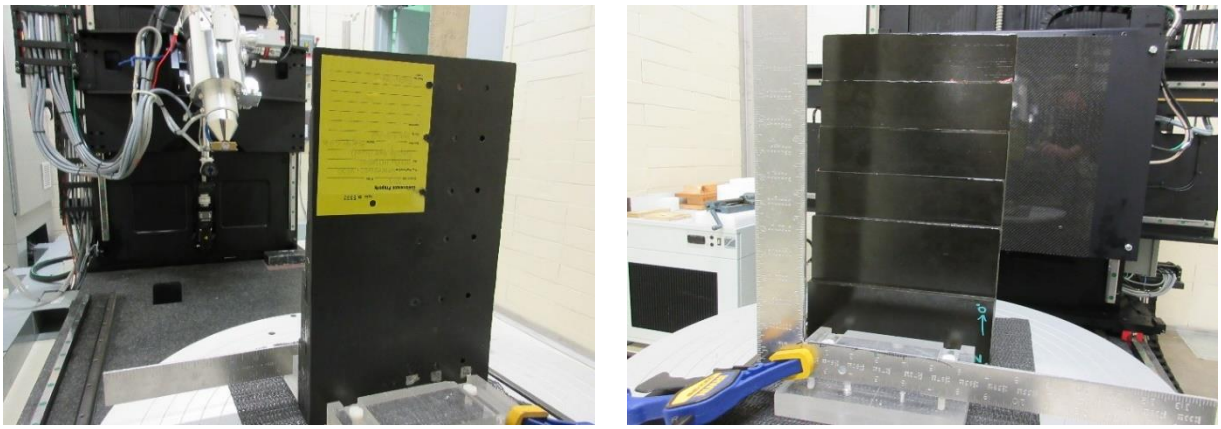

a) ***b)***

Figure E.2-4. Microfocus XCT system showing orientation of Specimen #2: NASA-S-MP.

E.2.1.6 Inspection Results

Section A

Specimen #2, NASA-S-MP, is a step wedge fabricated with an objective of achieving medium porosity. In addition, half of the specimen contains three flat-bottom holes at each step thickness that are backfilled with resin to mimic internal disbonds. XCT was performed on this specimen in NASA LaRC's large CT system with the settings defined in Section E.2.1.5. Two datasets were collected: the first with the specimen held by the thickest part of the wedge, and the second with the specimen rotated 180° and mounted with the thinnest step wedge clamped. This allows unimpeded inspection of the part hidden within the Plexiglas clamp. If desired, the datasets are stitched together in post-processing to view the entire specimen in a single volume.

The scan may be viewed as a volume (Figure E.2-5a), though defect analysis is best served through slice-by-slice images via axial directions seen in the following figures. Though the holes have been backfilled, they are clearly visible in both the volume and slice view. The dark regions represent gross porosity in the filling medium (Figure E.2-5b).

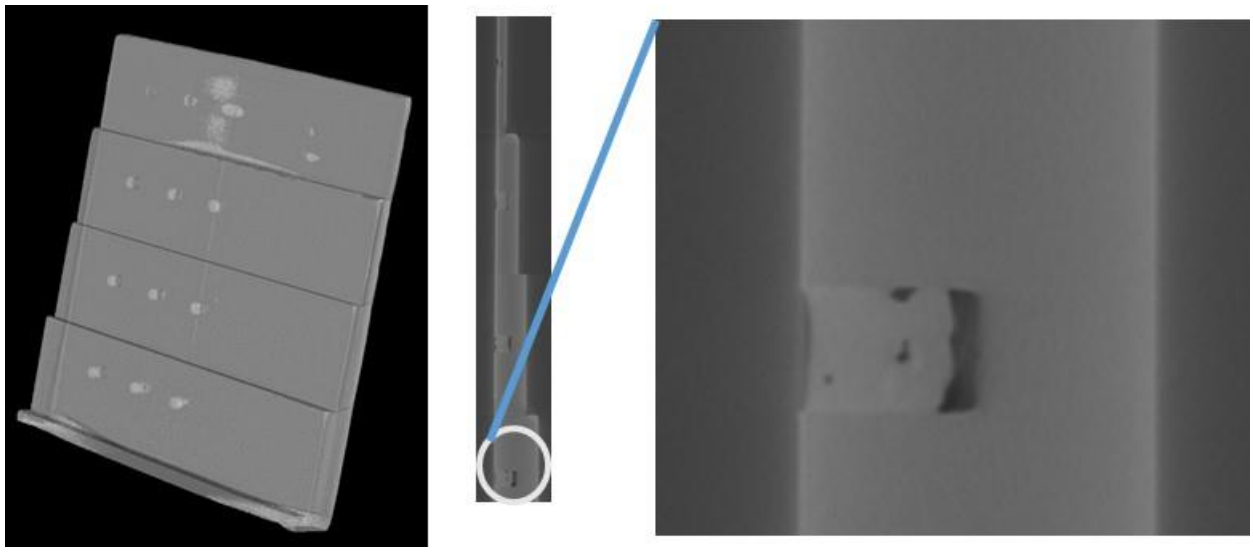

a) ***b)***

Figure E.2-5. Side view (X-Normal) of flat-bottom holes with filler.

Porosity is easily identified in views from all axis. Over 40 instances of porosity were detected through visual inspection of X-ray slices. Figure E.2-6 shows a slice from the x-direction with a porosity evident on the third step from the top of the material as indicated by the expanded view. The bulk material is represented by the clean and consistent grey medium making the contrast generated by an air pocket simple to detect.

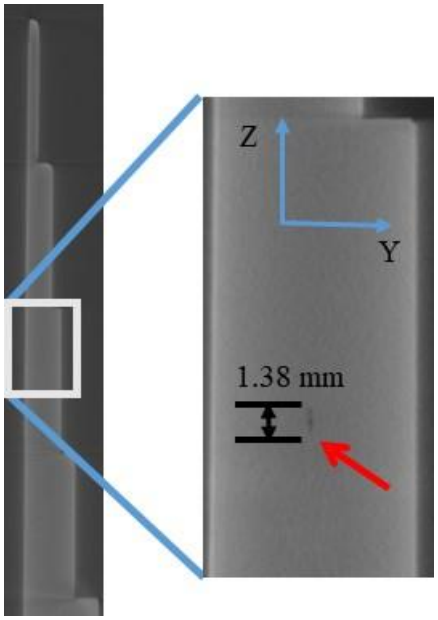

Figure E.2-6. Profile of specimen displaying porosity defect.

In comparison, FOD within the material shows up as bright spots due to the oftentimes-denser nature of the infringing material. Though FOD is not the subject of this report, FOD did show up periodically throughout the sample.

Figure E.2-7 shows two more instances of porosity occurring in plane with each other viewing the sample from the y-normal direction. The defects within this specimen occurred randomly throughout the sample following no apparent path.

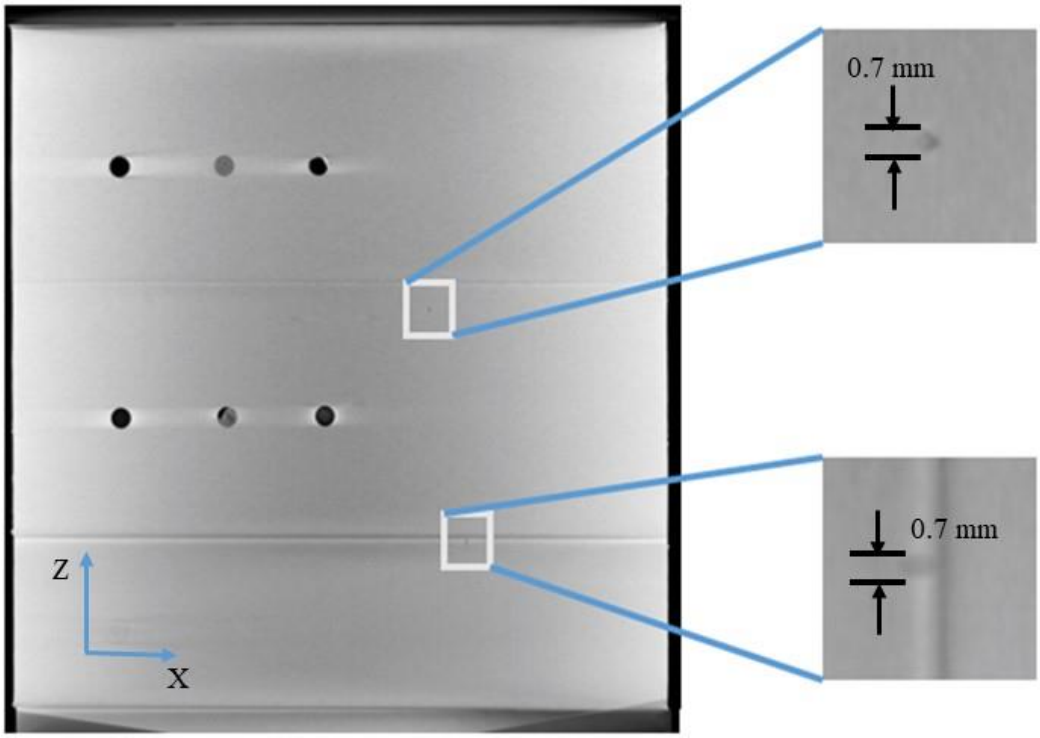

Figure E.2-7. Y-normal direction view of specimen showing two locations of porosity in plane with each other.

Section B

Semantic CT Image Segmentation Technique:

The developed semantic Computed Tomography (CT) image segmentation technique, originally designed at NASA LaRC, applies the Convolutional Neural Network (CNN) to identify and segment cracks and delamination in carbon fiber due to impact. The segmentation is done on the specimens' CT scan grayscale images. This method was first developed by D. T. Delelegn [1] as his master's thesis and then improved as a NASA white paper.

There are two implemented CNN models, each identifying the two damage types separately (i.e., crack and delamination). The first model easily identifies delamination, whereas the second is optimized to detect cracks and 'linear-type' damage. Each model prediction outputs are floating numbers between (0,1) indicating how likely an area is damaged. Class label one representing a highest damage prediction certainty while zero for a no-damage area. To seek the most damaged area in the material, this probabilistic prediction value of an area-damage indication is used.

The prediction is done on the CT images with a 4 × 4 window (patch) size. Then, the predicted class labels for each patch from the two models are combined as the Red (crack) and the Green (delamination) channels of the Red, Green, and Blue (RGB) color model representing the two damage types in different colors. For further reading, refer D.T. Delelegn [1].

This segmentation technique is able to easily point out cracks or linear damage that are collocated with a delamination. This is because the prediction of the two models are represented in the different channels of the RGB color model.

While originally developed to detect impact damage, RGB application to ACP Handbook standards (porosity, delamination, Automated fiber placement (AFP) defects, etc.) with varying degrees of success.

Here, the method is applied to handbook Specimen #2, a step specimen intended to contain medium porosity, with steps ranging from 0.1 to 1.0 inch. The specimen also contained flat-bottom holes drilled from the back surface of the sample intended to simulate disbonds or material loss. As seen in the standard XCT analysis above, the intended 'medium' porosity is described as 'light' porosity. The porosity and flat-bottom holes are detected, but especially for the porosity, this process is time consuming. Use of the image segmentation CNN analysis technique can dramatically reduce the analysis time and may result in findings that are more accurate.

Segmentation Output:

The segmentation algorithm accurately detected the intentional holes as expected. In addition, the two main porosity areas are detected. However, one of the two transitioning edges of the specimen was also detected as being damaged. As seen in Figure E.2-8, the magnified views of the two porosity areas reveal that the left region of interest (ROI) has darker pixel brightness that formed a linear structure within the area compared to the surrounding area pixels, which is what the model was developed for. As a result, there should be a close assessment of the model predictions for each image and care should be taken before reaching at a conclusion.

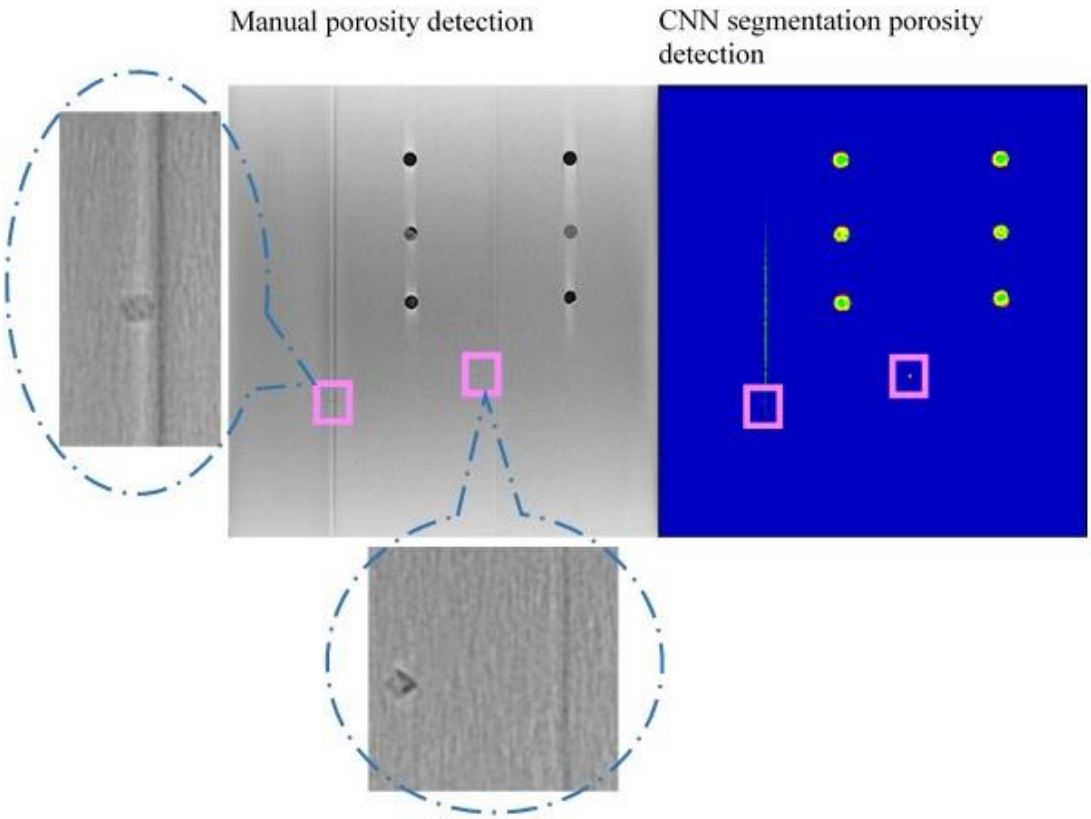

Figure E.2-8. (Left) Manual porosity detection of Y-normal slice showing two locations of porosity. (Right) Porosity detection by CNN Segmentation of same slice.

Figure E.2-9 is the 3D damage representation that was observed near the image shown in Figure E.2-7. As can be seen, the right-side porosity in Figure E.2-8 is more pronounced than the one of the left. This visual information can used to assess and compare the intensity of defects within a specimen.

During the prediction of the CT images, the model was able to detect surface delamination and porosity that were not noticed by the subject matter experts (SMEs), which later confirmed to be defects after a close examination. This encounter was a lesson to take a closer look at the predictions even if they have what looks like false positive prediction areas see Figure E.2-10.

In conclusion, the major benefit of implementing this kind of CT image analysis is to understand and visualize the extent of damage. This analysis gives SMEs a second, closer look at the CT images, which can be very valuable in cases like Figure E.2-10.

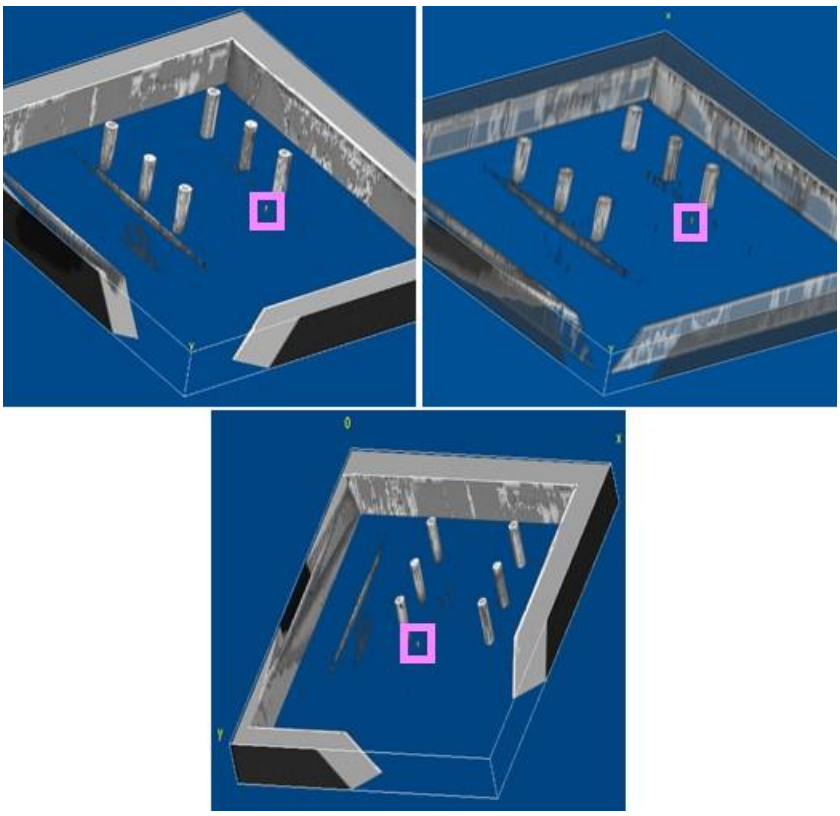

Figure E.2-9. 3D visualization of the detected damage on Specimen #2 (NASA-S-MP).

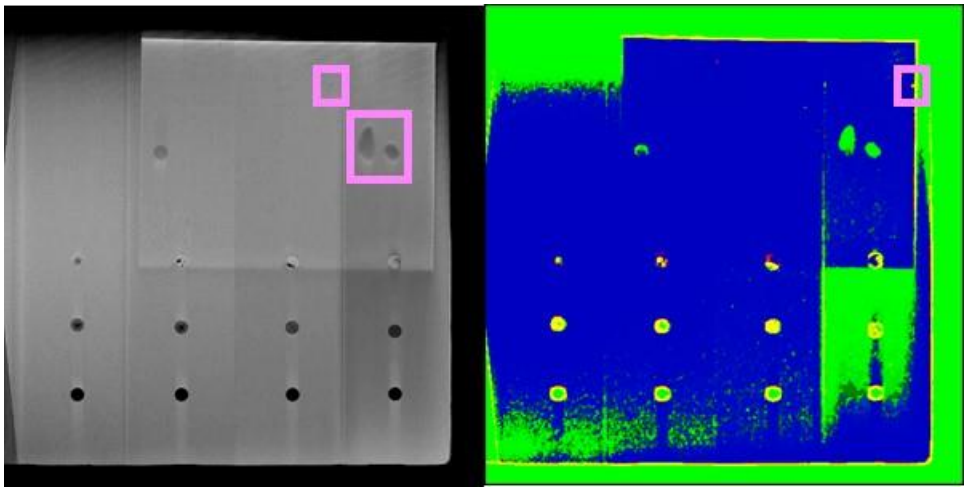

Figure E.2-10. The developed CNN Model detected damage illustration on Specimen #2 (NASA-S-MP), which were missed by SMEs.

E.2.1.7 References

[1] Delelegn, Desalegn Temesgen, "Non-destructive Evaluation for Composite Material," Master of Science Thesis, Old Dominion University, August 2018

E.2.2 *Method: Pulse-Echo Ultrasound Testing (PEUT)*

E.2.2.1 Partner: NGIS

E.2.2.2 Technique Applicability: ★★★

Water-coupled PEUT scans were performed to demonstrate the feasibility of detecting defects in thick carbon-composite laminates on a stepped-thickness panel with back-drilled flat-bottom holes and laminate thickness ranging from 0.1 to 1.0 inch. Scans performed from the flat-tool side determine detection dependency on both defect depth and diameter. Different frequencies including 0.5, 1.0, and 2.25 MHz were sampled to observe frequency dependence.

E.2.2.3 Laboratory Setup

PEUT scans performed in the Test-Tech 3-axis scanning tank used the water-squirter method (see Figure E.2-11). For each panel, use of optimum water nozzle and column diameter achieved optimal SNR and defect detection (if defects existed).

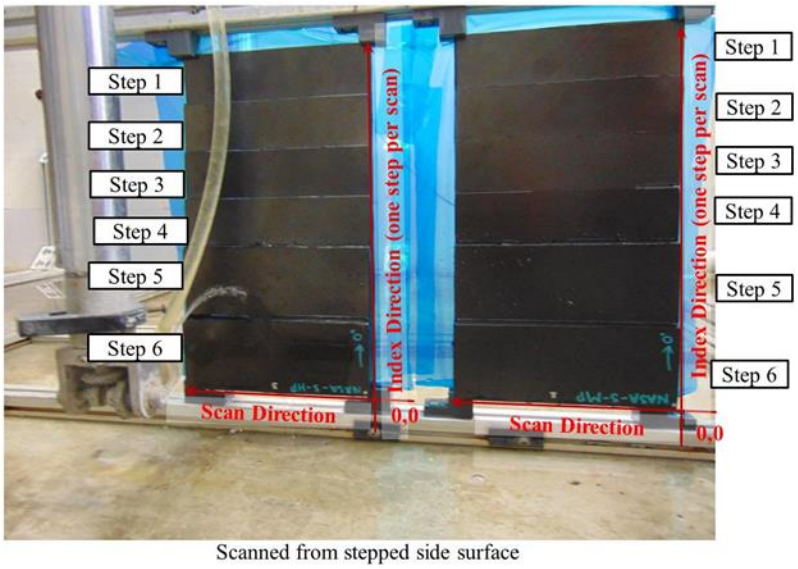

Scanned from stepped side surface

Figure E.2-11. PEUT setup in Test-Tech scanning tank.

E.2.2.4 Equipment List and Specifications:

- Test-Tech 3-axis scanning tank
- Olympus 5077PR Square Wave Pulser/Receiver
- Transducer Frequencies: 0.5, 1.0, and 2.25 MHz

E.2.2.5 Settings

Table E.2-2. Equipment settings for 0.5 MHz scan.

Transducer	Brand	Model	Freq. (MHz)	Element Dia. (in.)	Water Column Dia (in.)			Outer Dia. (in)		
Transmitter	GE	Benchmark	0.5	0.5	0.5			0.5		
Pulser/Receiver	PRF	Voltage	Freq. (MHz)		HPF	LPF (MHz)	Rtune	Ttune	Attn	Range
Olympus	Ext	400	0.5		Out	Full BW	N/A	N/A	N/A	N/A
	Gain (dB)	"-14 for Steps 1-6								

Table E.2-3. Equipment settings for 1.0 MHz scan.

Transducer	Brand	Model	Freq. (MHz)	Element Dia. (in.)	Water Column Dia (in.)			Outer Dia. (in)		
Transmitter	Sonic	IBK I-2	1	0.5	0.375			0.5		
Pulser/Receiver	PRF	Voltage	Freq. (MHz)		HPF	LPF (MHz)	Rtune	Ttune	Attn	Range
Olympus	Ext	400	1.0		Out	Full BW	N/A	N/A	N/A	N/A
	Gain (dB)	3 for Steps 1-6								

Table E.2-4. Equipment settings for 2.25 MHz scan.

Transducer	Brand	Model	Freq. (MHz)	Element Dia. (in.)	Water Column Dia (in.)			Outer Dia. (in)		
Transmitter	KB-Aerotech	Alpha	2.25	0.25	0.25					
Pulser/Receiver	PRF	Voltage	Freq. (MHz)		HPF	LPF (MHz)	Rtune	Ttune	Attn	Range
Olympus	Ext	200	2-2.25		Out	Full BW	N/A	N/A	N/A	N/A
	Gain (dB)	10 for Steps 1-6								

E.2.2.6 Inspection Results

Snapshots of C-scans are provided below that show internal gates and laminate back-wall gates. Not all defects or back walls were detected for all measured frequencies. At higher frequencies, the thicker laminate was too attenuating. For lower frequencies on thinner laminate, internal and back-wall signals could not be temporally resolved.

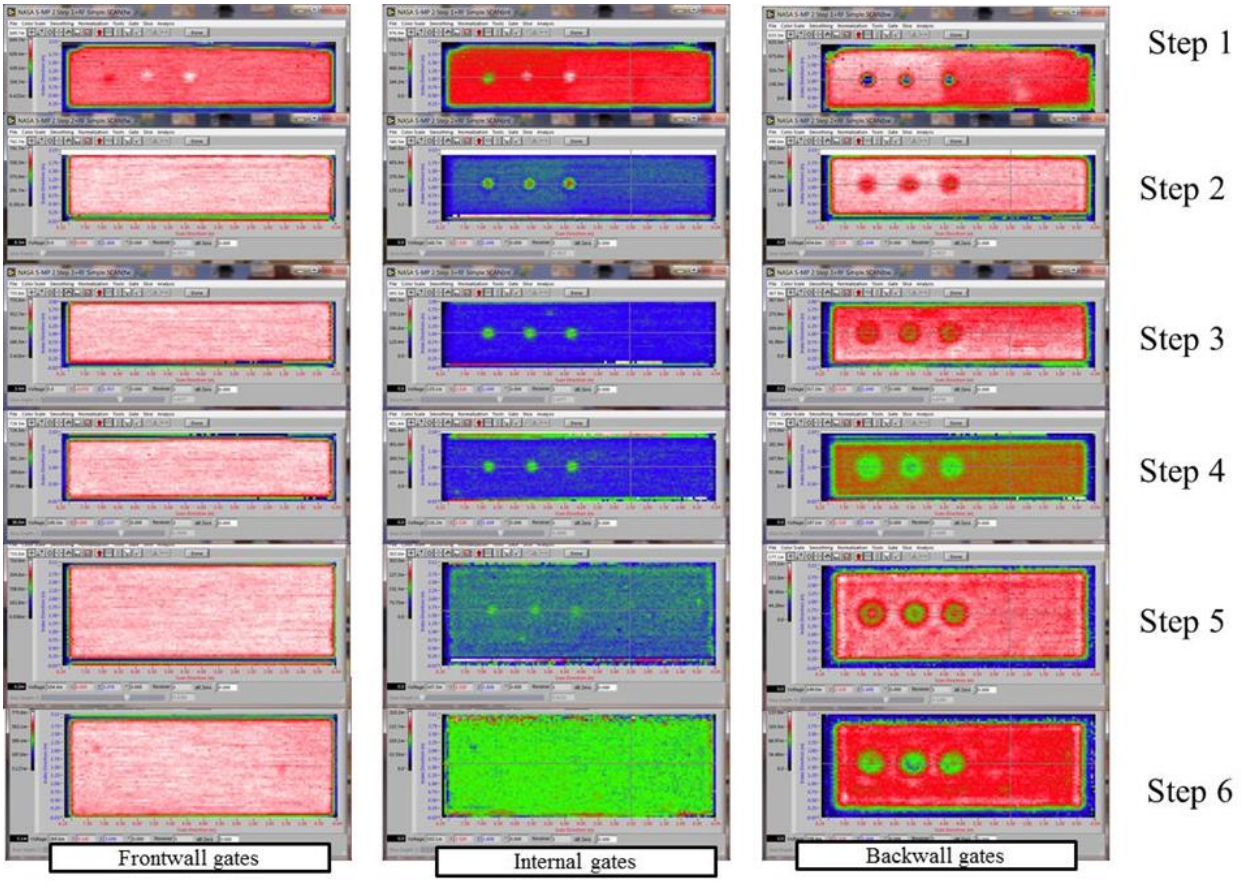

Figure E.2-12. PEUT C-scans at 500 kHz for Steps 1–6.
Front-wall gate (left), internal gate (center), and back-wall gate (right) C-scans shown.

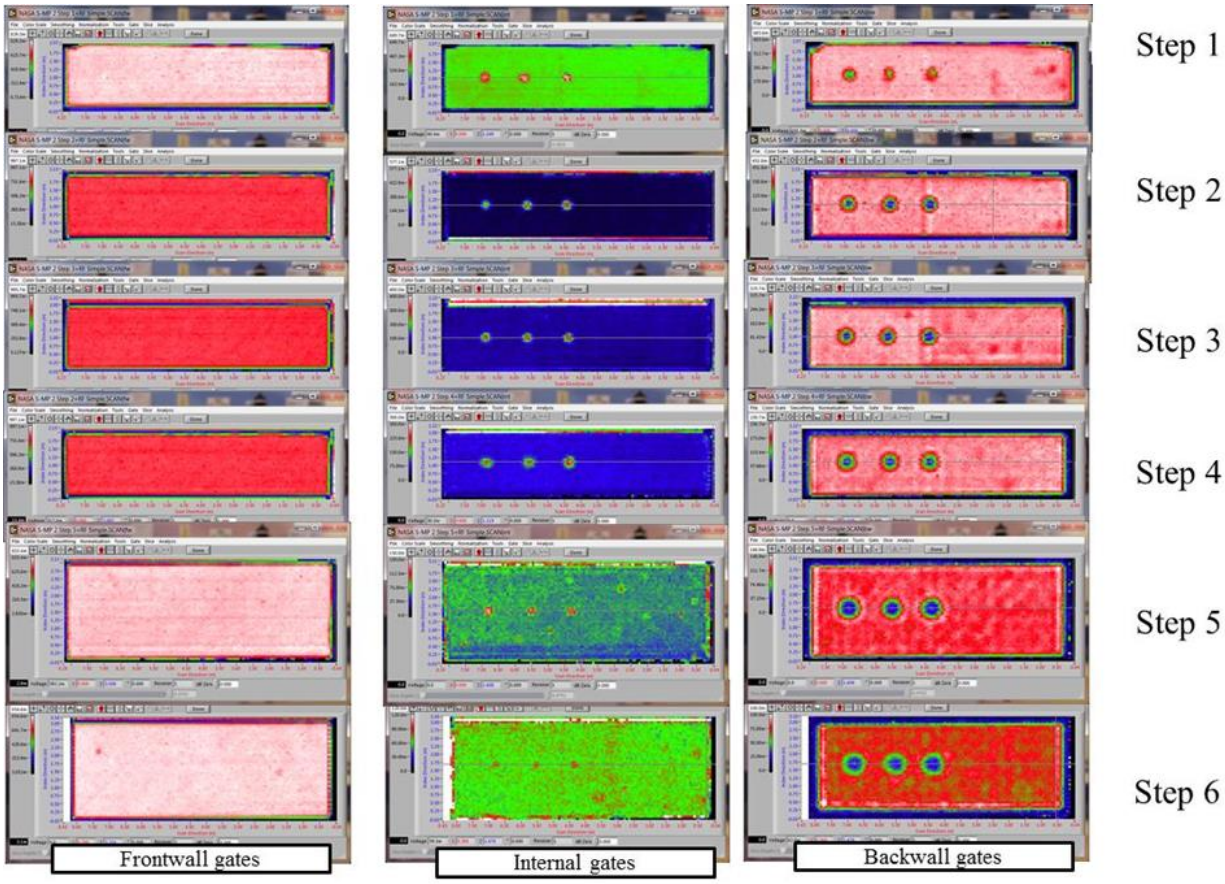

Figure E.2-13. PEUT C-scans at 1.0 MHz for steps 1–6.
Front-wall gate (left), internal gate (center), and back-wall gate (right) C-scans shown.

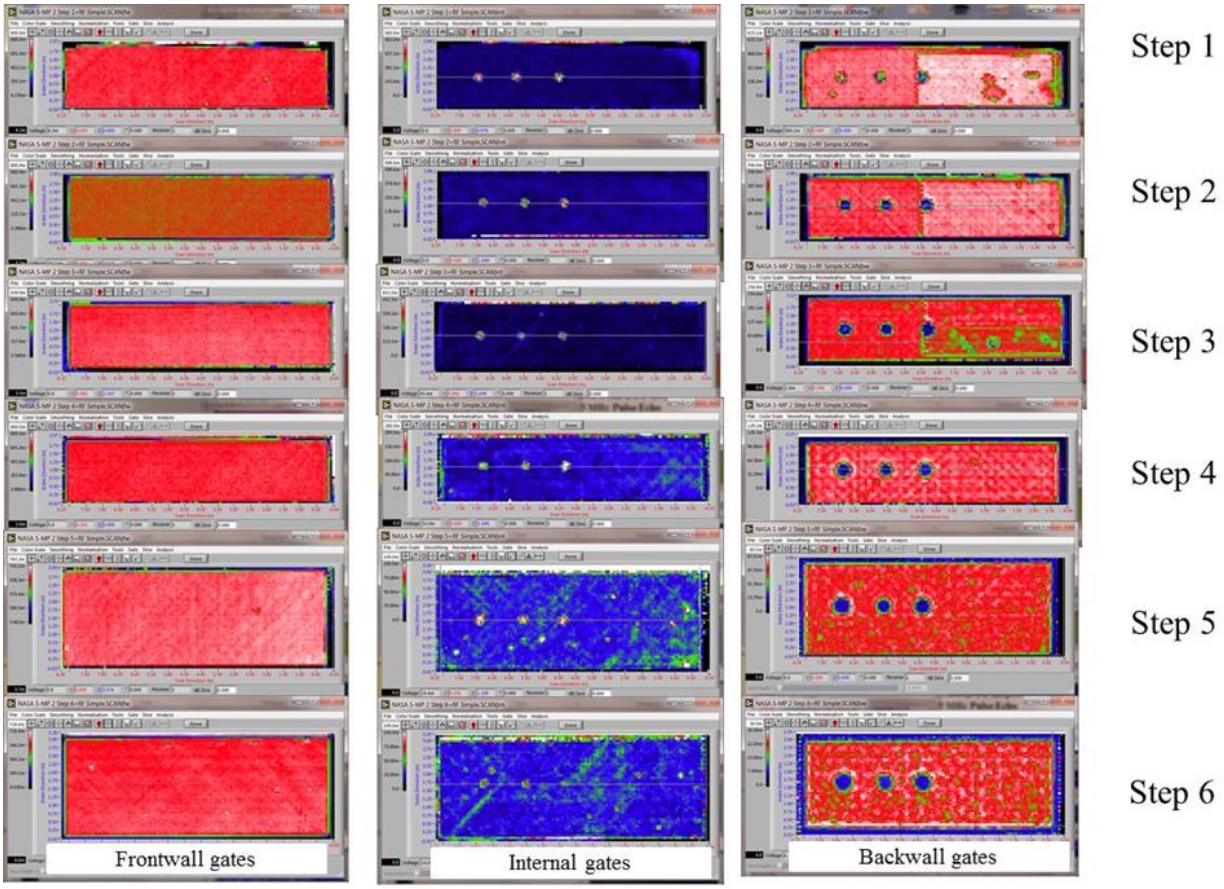

Figure E.2-14. PEUT C-scans at 2.25 MHz for Steps 1–6.
Front-wall gate (left), internal gate (center), and back-wall gate (right) C-scans shown.

E.2.2.7 References

[1] Workman, Gary L, and Doron Kishoni. Nondestructive Testing Handbook. Third. Edited by Patrick O Moore. Vol. 7. American Society for Nondestructive Testing (ANST), 2007.

E.2.3 *Method: Single-Sided Infrared (IR) Thermography (SSIR)*

E.2.3.1 Partner: NGIS

E.2.3.2 Technique Applicability: ★☆☆

The thermal response produced by single-sided thermographic inspection is dominated by factors other than porosity. It was found that slight variations in thickness and localized thermal property variation dominated the surface temperature compared to material's porosity. For this reason, single-sided inspection is not recommend as a technique for discriminating porosity.

E.2.3.3 Laboratory Setup

Single-Sided Thermography images were acquired using a Forward-looking Infrared (FLIR) SC6000 camera setup. The thermal camera is mounted to the back of the flash hood and mounted in a fixed location on an optical table. The panel is held vertically within a fixture that slides across a linear track between captures in order to ensure total coverage. Paper light shields were constructed for the fixture to block flash spillover around the edges of the panel.

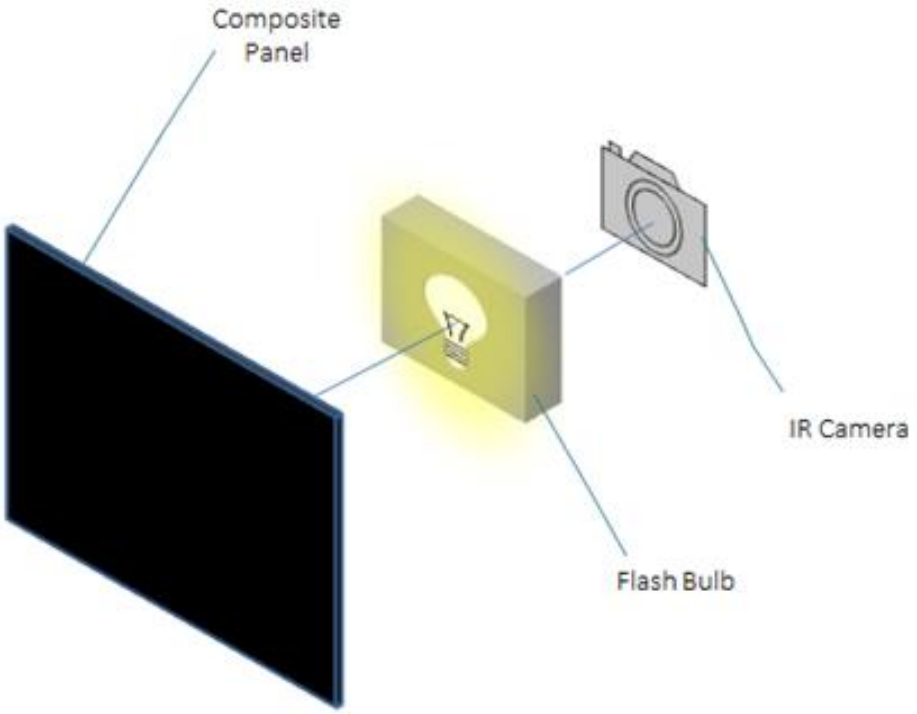

Figure E.2-15. Single-sided thermography schematic.

Figure E.2-16. Photo of single-sided thermography setup.

E.2.3.4 Equipment List and Specifications:

- FLIR SC6000 camera, mid-wavelength IR sensor (3.0–5.0 µm)
- Flash power supplies, hood, and lamps
- EchoTherm® V8 Software

E.2.3.5 Settings

Table E.2-5. Equipment settings for SSIR scan.

Flash Duration (ms)	30
Capture Elapsed Time (s)	12.06
Camera Frequency (Hz)	37.92
Integration Time (s)	2

E.2.3.6 Inspection Results

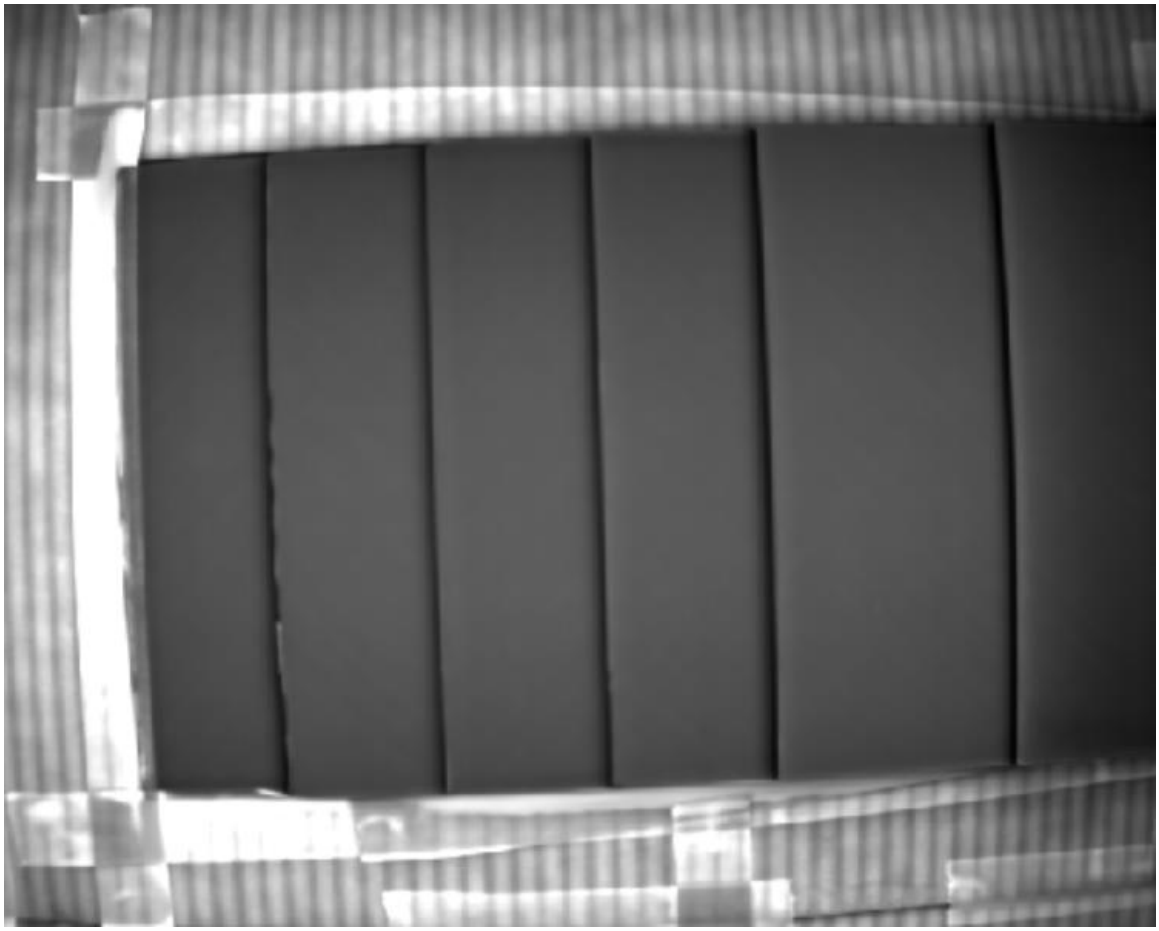

Figure E.2-17. Single-sided thermography image of Specimen #2.

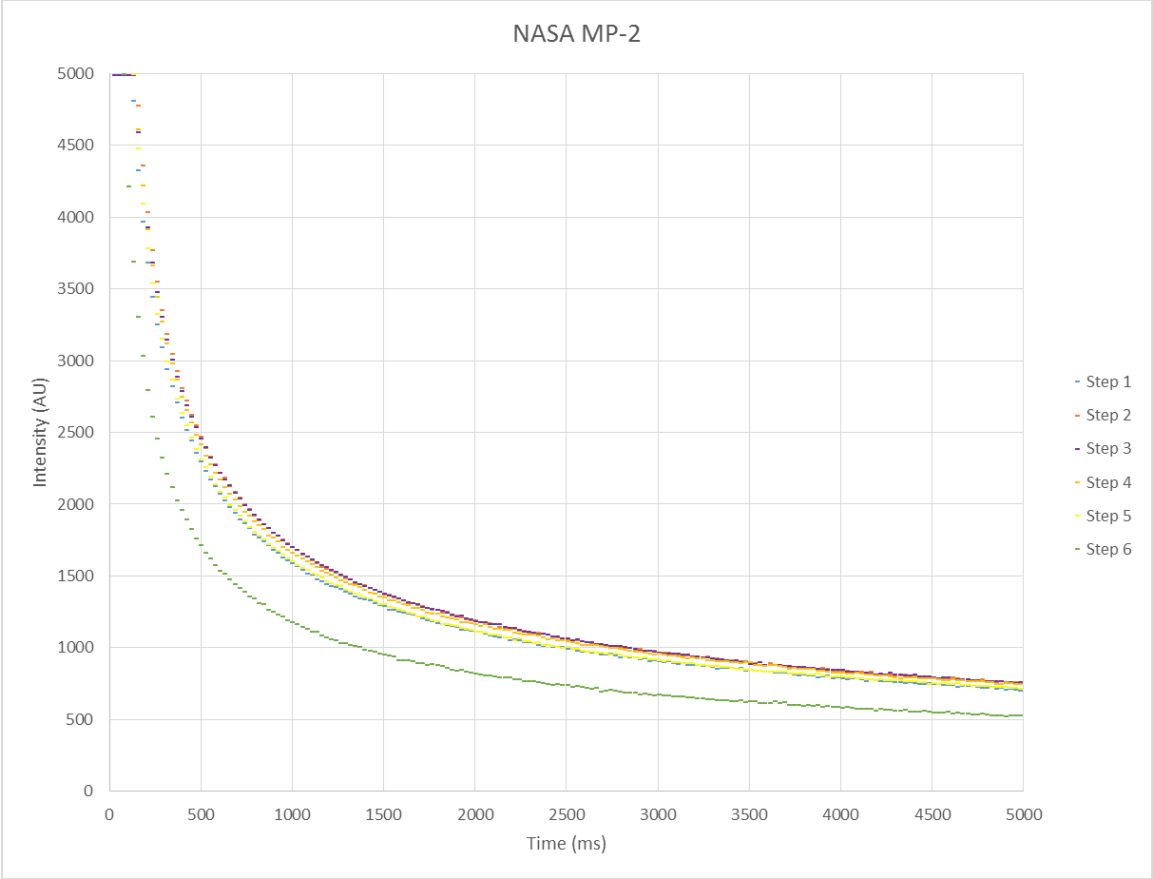

Figure E.2-18. Intensity curve showing heat dispersion over time for each step of Specimen #2.

E.2.3.7 References

[1] W.J. Parker; R.J. Jenkins; C.P. Butler; G.L. Abbott (1961). "Method of Determining Thermal Diffusivity, Heat Capacity and Thermal Conductivity". *Journal of Applied Physics*. 32 (9): 1679. :1961JAP....32.1679P. doi:10.1063/1.1728417

E.2.4 *Method: Through-Transmission Infrared Thermography (TTIR)*

E.2.4.1 Partner: NGIS

E.2.4.2 Technique Applicability: ★★☆

E.2.4.3 Laboratory Setup:

TTIR images were acquired using a FLIR SC6000 IR camera setup. The flash hood is mounted in a fixed location on an optical table. The thermal camera is mounted on a tripod with the panel between it and the flash hood. The panel is held vertically within a fixture that slides across a linear track between captures in order to ensure total coverage. Paper light shields were constructed for the fixture to block flash spillover around the edges of the panel.

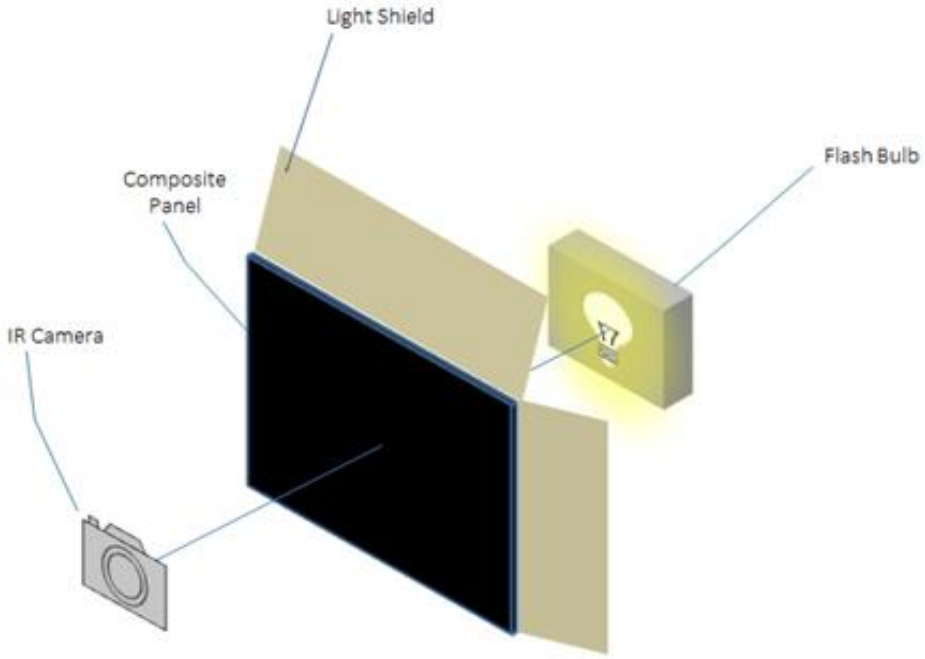

Figure E.2-19. TTIR schematic.

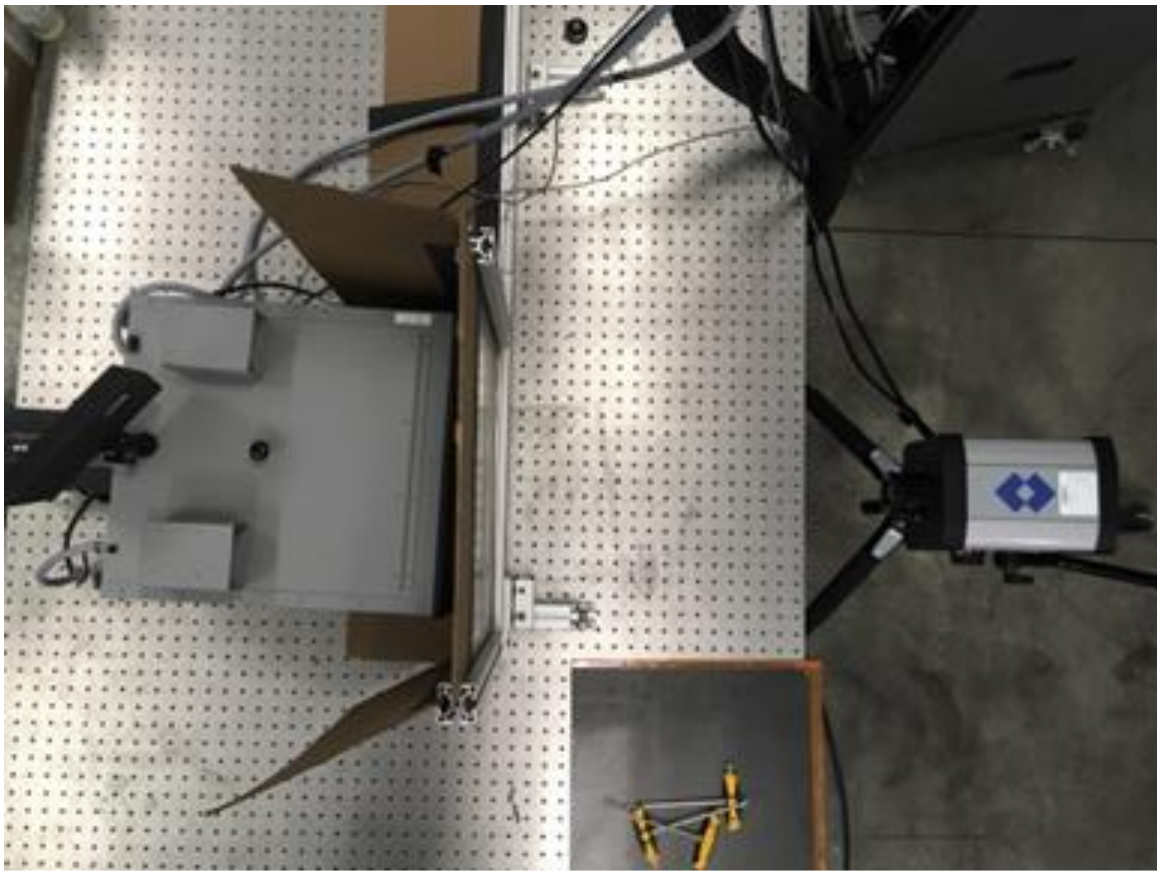

Figure E.2-20. Photo of TTIR setup.

E.2.4.4 Equipment List and Specifications:

- FLIR SC6000 IR camera, mid wavelength IR sensor (3.0–5.0 µm)
- Flash power supplies, hood, and lamps
- EchoTherm® V8 Software

E.2.4.5 Settings

Table E.2-6. Equipment settings for TTIR scan.

Panel Thickness (mm)	3.37 (Step 1)
Flash Duratio (ms)	30
Capture Elapsed Time (s)	34.85
Camera Frequency (Hz)	4.39
Integration Time (s)	2

E.2.4.6 Inspection Results

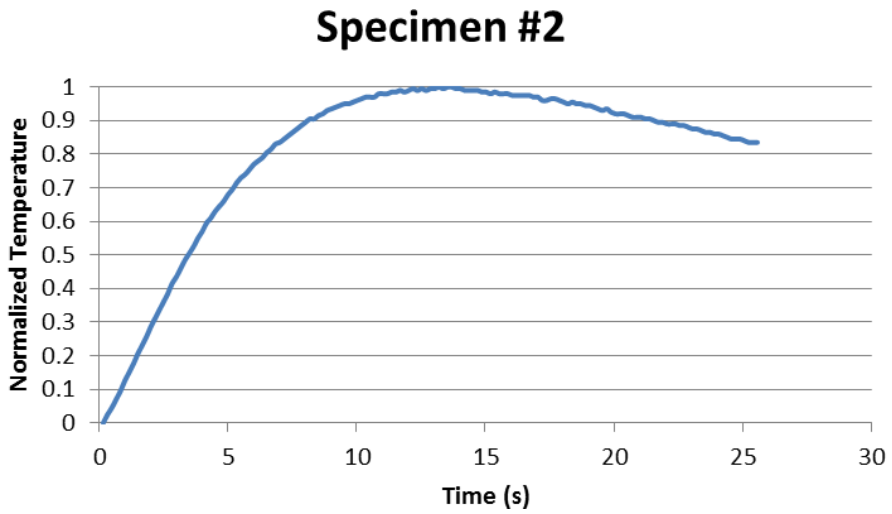

Figure E.2-21. Temperature curve showing the dispersion of heat over time during image capture of Step 1.

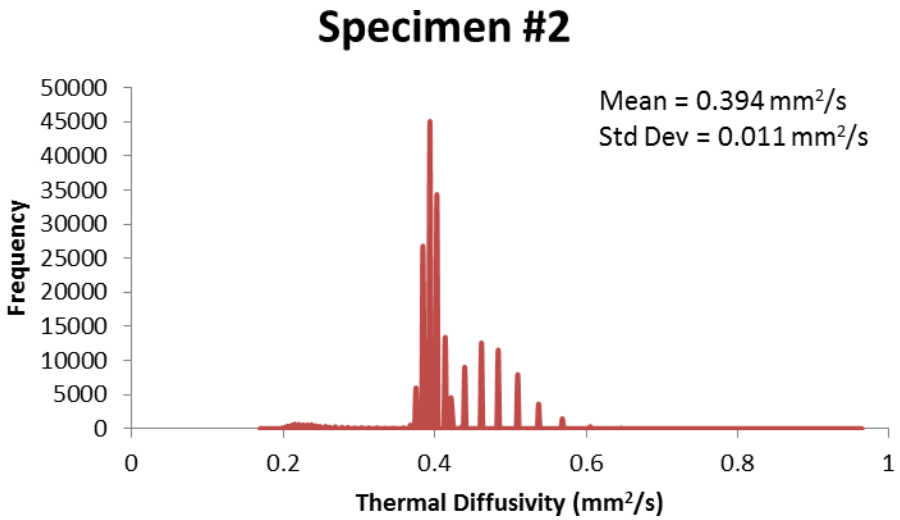

Figure E.2-22. Histogram showing frequency of thermal diffusivity values. Tighter point spread shows consistent porosity throughout Step 1 of panel and a low standard deviation shows low porosity levels.

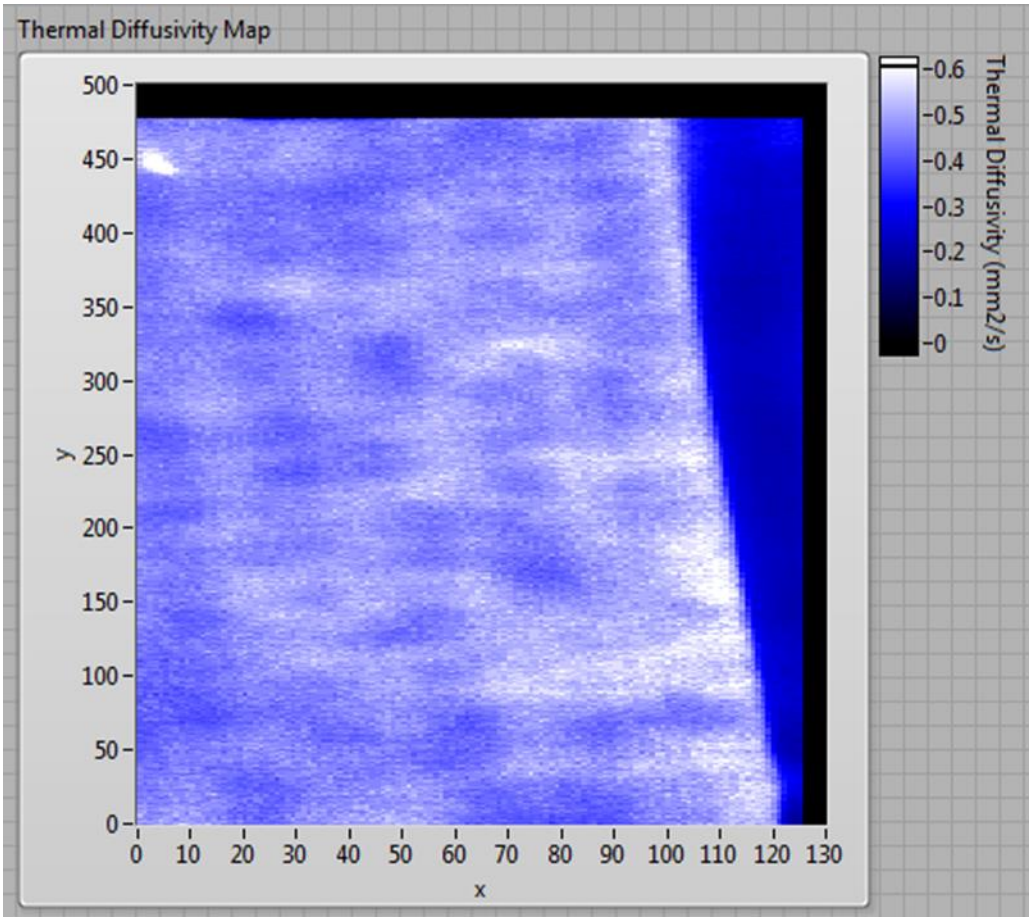

Figure E.2-23. Image of thermal diffusivity post processing. Dark spots represent low diffusivity and show indications of porosity. White spot in top left corner represents a flat-bottom hole.

E.2.4.7 References

[1] W.J. Parker; R.J. Jenkins; C.P. Butler; G.L. Abbott (1961). "Method of Determining Thermal Diffusivity, Heat Capacity and Thermal Conductivity". *Journal of Applied Physics*. 32 (9): 1679. Bibcode:1961JAP....32.1679P. doi:10.1063/1.1728417

E.3 Specimen #3: NASA-S-HP

Structure	Material	Details	Dimensions (inches)	Partner Methods	
Uni-ply (0/90/45)	IM7/8552	Step with high porosity Step heights: 0.1-1.0 inch	14 × 8 × 1.5	NASA	E.3.1 XCT
				NGIS	E.3.2 PEUT E.3.3 SSIR E.3.4 TTIR

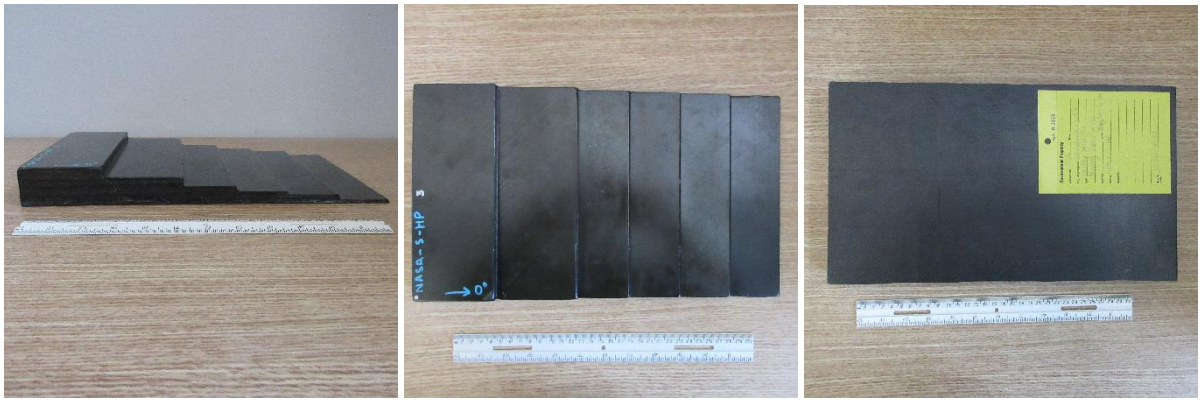

Figure E.3-1. Photographs of Specimen #3: NASA-S-HP.

E.3.1 *Method: X-ray Computed Tomography (XCT)*

E.3.1.1 Partner: NASA

E.3.1.2 Technique Applicability: ★★★

XCT is capable of imaging the high porosity in this specimen.

E.3.1.3 Laboratory Setup

The microfocus XCT system at NASA LaRC is a commercially available Avonix (Nikon C2) Metrology System designed for high-resolution NDE inspections. The system is an advanced microfocus X-ray system, capable of resolving details down to 5 μm, and with magnifications up to 60X. Supplied as complete, the system is a large-dimension radiation enclosure with X-ray source, specimen manipulator, and an amorphous silica detector, as shown in Figure E.3-2. The imaging controls are housed in a separate control console. The detector, visible behind the specimen in Figure E.3-4b, is a Perkin-Elmer, 16-bit, amorphous-silicon digital detector with a 2000 × 2000-pixel array.

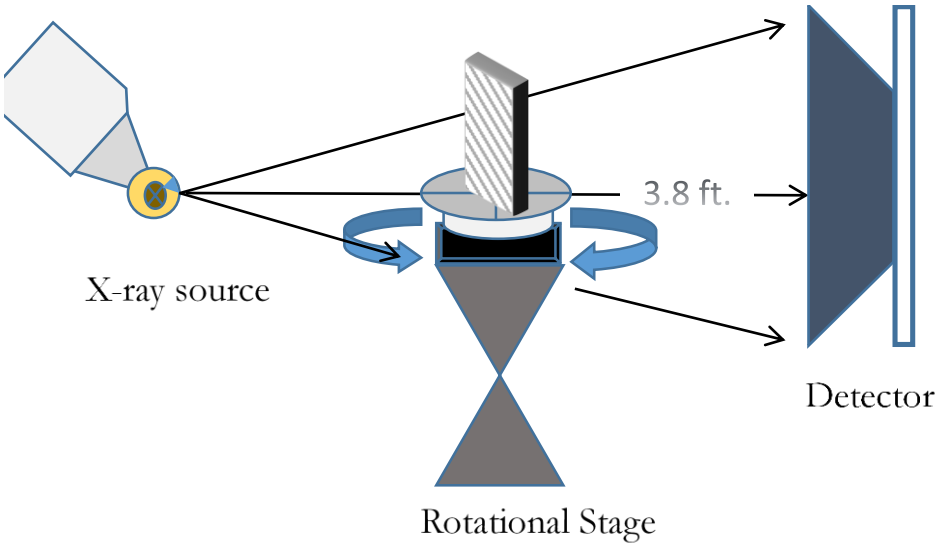

Figure E.3-2. XCT system components.

A consistent Cartesian coordinate system is used to define slice direction as illustrated in Figure E.3-3. Slices normal to the X-, Y-, and Z-directions are shown in Figure E.3-3a, b, and c, respectively.

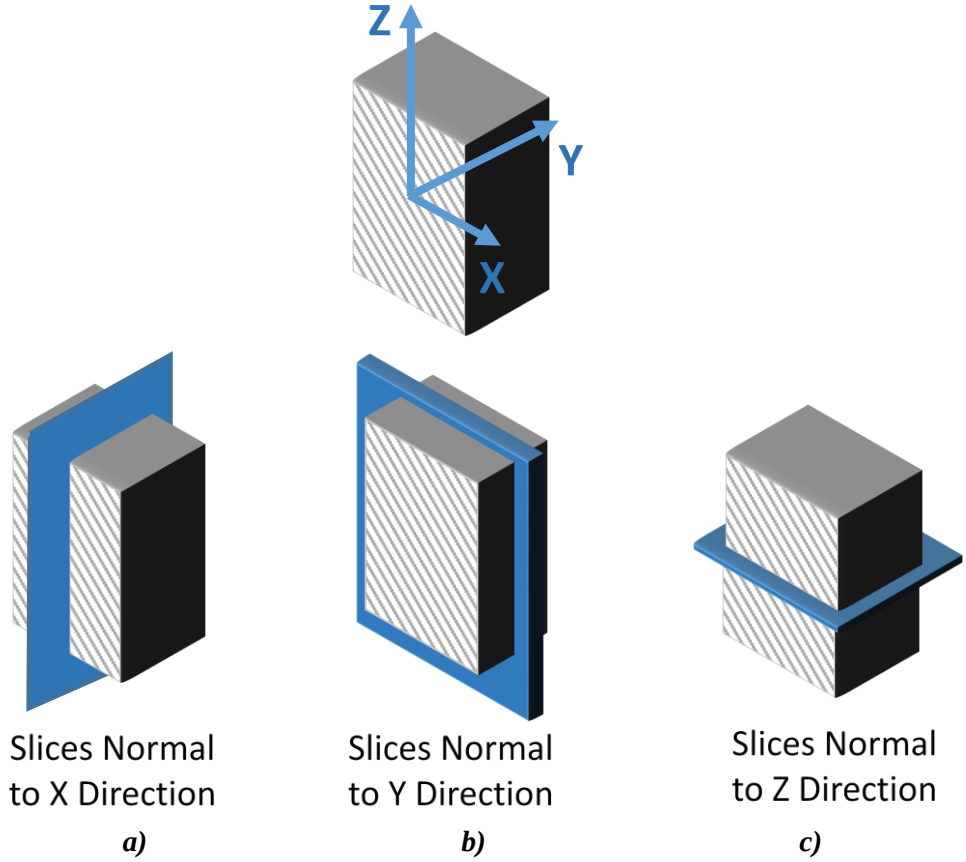

a) ***b)*** ***c)***

Figure E.3-3. Slice direction nomenclature.

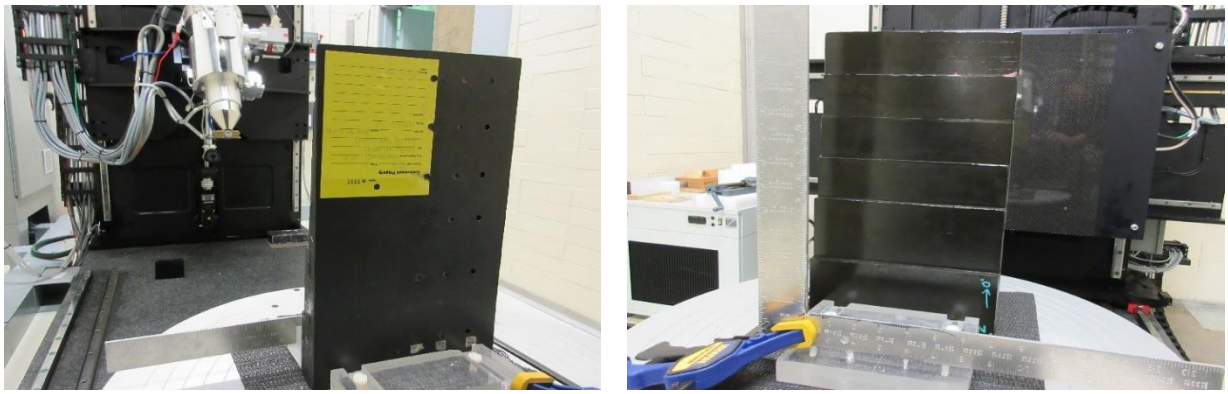

a) ***b)***

Figure E.3-4. Microfocus XCT system showing orientation of Specimen #3: NASA-S-HP.

E.3.1.4 Equipment List and Specifications:

- Avonix 225 CT System
- 225 kV microfocus X-ray source with five µm focal spot size
- 15 or 30 kg Capacity, 5-axis, fully programmable manipulator
- Detector: Perkin Elmer XRD 1621 – 2000 × 2000 pixels with 200 µm pitch

- 10 μm spatial resolution for specimens 1.5 cm wide
- Thin panels 10 × 10 inch – full volume 200 μm spatial resolution

E.3.1.5 Settings

Table E.3-1. Data collection settings.

Source Energy	120 kV
Current	90 μA
Magnification	1.75 X
Filter	NF
# Rotational angles	3142
Exposure time / frame	1.0 sec
Max Histogram Grey Level	22 K
# Averages	8
Resolution (μm)	114.894 μm
Array Dimensions (pixels)	Set 1: 1999 × 362 × 1998 Set 2: 1998 × 686 × 1997

The specimen is placed vertically (rotated about the smallest dimension) on the rotational stage located between the radiation source and the detector. The rotational stage is computer controlled and correlated to the position of the sample. As the sample is rotated the full 360° (~0.11° increments), the detector collects radiographs at each rotated angle as the X-ray path intersects the sample. 3D reconstruction of the collection of radiographs produces a volume of data observed along any plane in the volume. The closer the sample is placed to the X-ray source, the higher the spatial resolution that can be obtained.

E.3.1.6 Inspection Results

Section A

Specimen #3, NASA-S-HP, is a step wedge fabricated with an objective of achieving high porosity. In addition. XCT was performed on this specimen in NASA LaRC's large CT system with the settings defined in Section E.3.1.5. Two datasets were collected: the first with the specimen held by the thickest part of the wedge, and the second with the specimen rotated 180° and mounted with the thinnest step wedge clamped. This allows unimpeded inspection of the part hidden within the Plexiglas® clamp. If desired, the datasets are stitched together in post-processing to view the entire specimen in a single volume.

Porosity is identified in views from all axis (Figure E.3-5 and Figure E.3-6). The view along the y-direction shows the different fiber directions due to the specimen being slightly out of plane of the viewing direction. The high porosity desired in this specimen was achieved, as there are countless areas of defects through nearly all slices of the scan. The porosity in this case is represented by the darker regions peppered throughout the sample. As well as gross porosity, there are delaminations present throughout the specimen. Figure E.3-5 and Figure E.3-6 show the same delamination viewed from the z- and y-direction of the sample. There were instances of FOD that showed up as bright spots due to the oftentimes-denser nature of the infringing material.

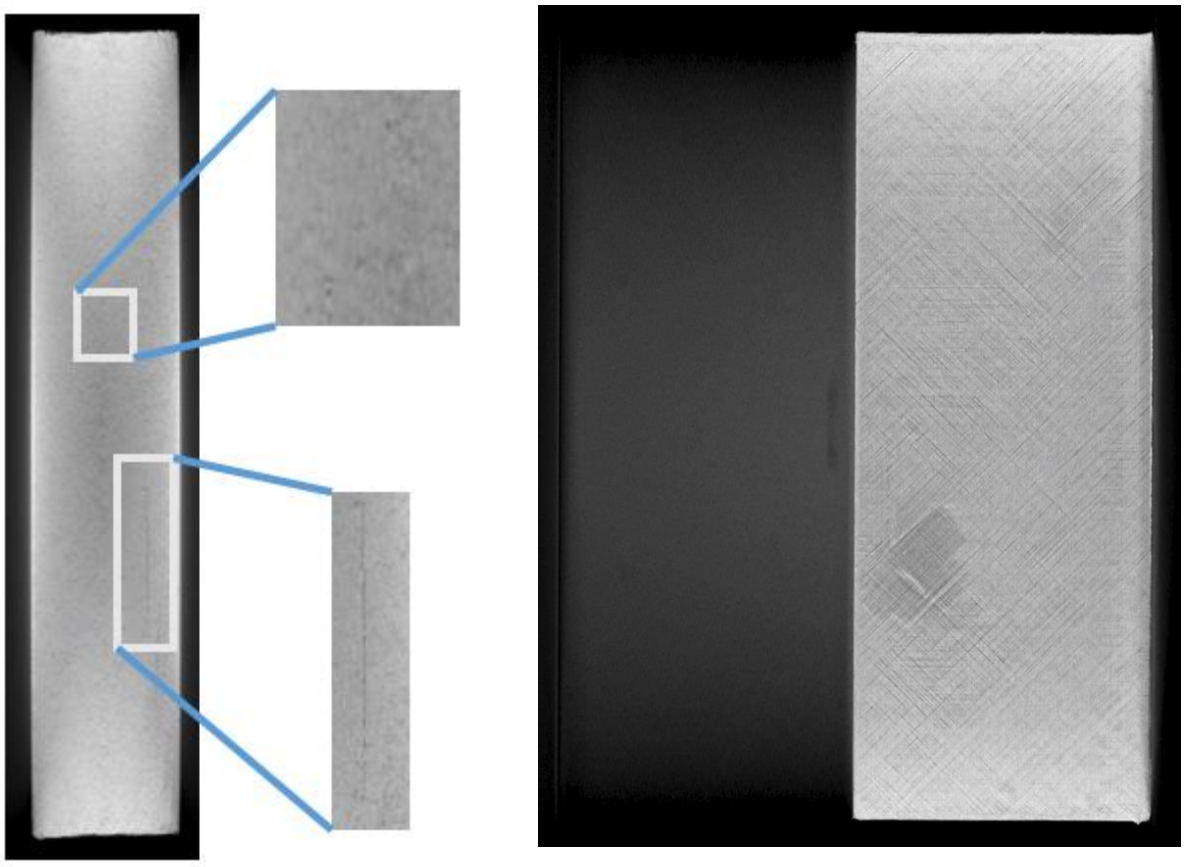

a) ***b)***

Figure E.3-5. a) XCT scan of specimen #2 viewed from the z-direction. b) XCT scan viewed from the y-direction.

In Figure E.3-6, the extensive porosity is seen once again along with several instances of small delaminations. These delaminations and porosity cause a slight bowing in the specimen, which exacerbates the out-of-plane effect seen in Figure E.3-5 and Figure E.3-6.

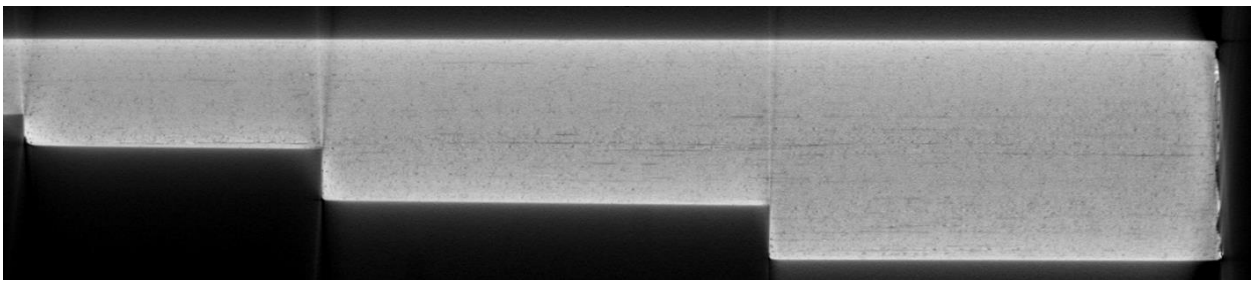

Figure E.3-6. XCT scan of Specimen #2 viewed from the x-direction.

Section B

Semantic CT Image Segmentation Technique:

The semantic CT image segmentation technique, originally designed at NASA LaRC, applies the CNN to identify and segment cracks and delamination in carbon fiber due to impact. The segmentation is done on the specimens' CT scan grayscale images. This method was first developed by D.T. Delelegn [1] as his master's thesis and then improved as a NASA white paper.

There are two implemented CNN models, each identifying the two damage types separately (i.e., crack and delamination). The first model easily identifies delamination, whereas the second is optimized to detect cracks and 'linear-type' damage. Each model prediction outputs are floating numbers between (0,1) indicating how likely an area is damaged. Class label one representing a highest damage prediction certainty while zero for a no-damage area. To seek the most damaged area in the material, this probabilistic prediction value of an area-damage indication is used.

The prediction is done on the CT images with a 4 × 4 window (patch) size. Then, the predicted class labels for each patch from the two models are combined as the Red (crack) and the Green (delamination) channels of the RGB color model representing the two damage types in different colors. For further reading, refer D.T. Delelegn [1].

This segmentation technique is able to easily point out cracks or linear damage that are collocated with a delamination. This is because that the prediction of the two models are represented in the different channels of the RGB color model.

While originally developed to detect impact damage, the method was applied to ACP Handbook standards (porosity, delamination, AFP defects, etc.) with varying degrees of success. Here, the method is applied to handbook specimen #3, which is a 14 × 8 × 1.5-inch step configuration with medium porosity, which is easily identified in the delaminations shown in Figures E.3-7 and E.3-8.

Segmentation Output:

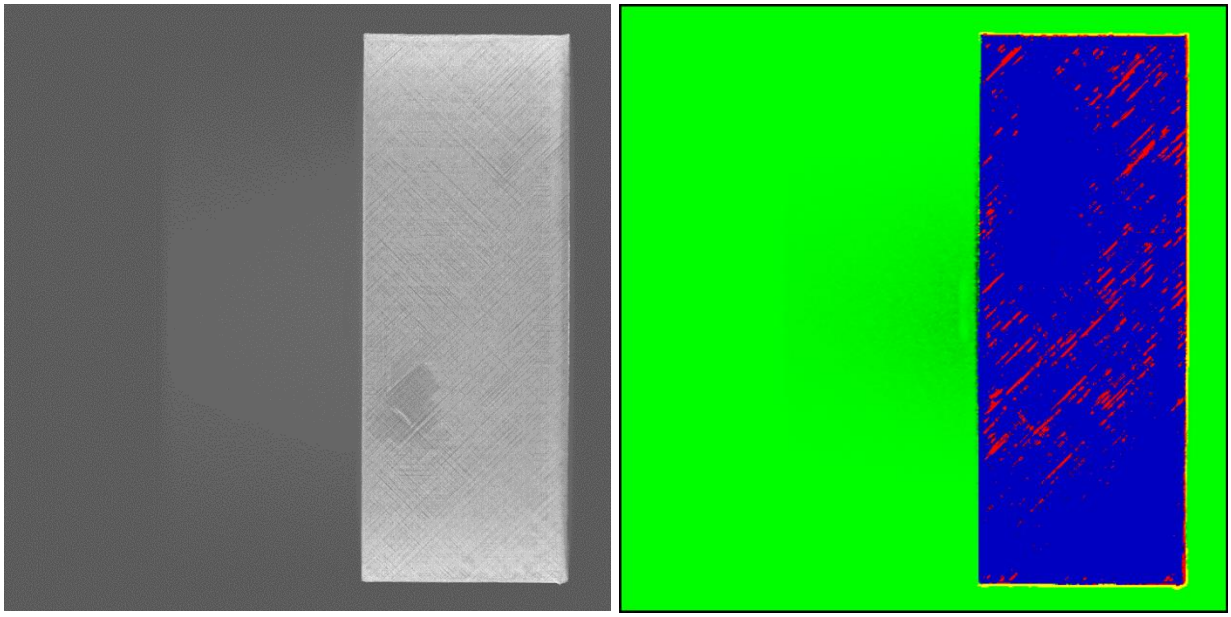

Figure E.3-7. (Left) XCT scan viewed from the y-normal direction. (Right) Defect detection using CNN segmentation of the same slice.

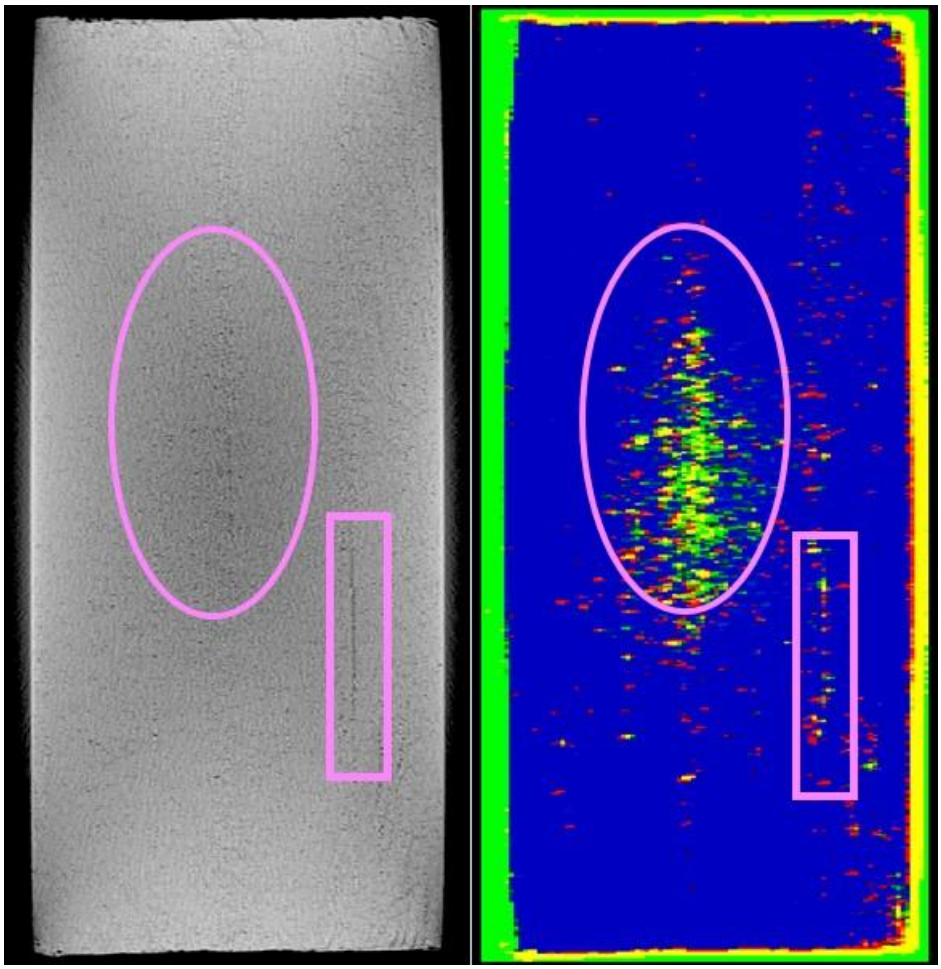

Figure E.3-8. (Left) XCT scan viewed from the z-normal direction. (Right) Defect detection using CNN segmentation of the same slice (NASA-S-HP).
The region of porosity within drawn oval was missed by SMEs.

E.3.1.7 References

[1] Delelegn, Desalegn Temesgen, "Non-destructive Evaluation for Composite Material," Master of Science Thesis, Old Dominion University, August 2018

E.3.2 *Method: Pulse-Echo Ultrasound Testing (PEUT)*

E.3.2.1 Partner: NGIS

E.3.2.2 Technique Applicability: ★★☆

PEUT scans were performed to demonstrate the feasibility of detecting defects on the stepped panel since the flat-tool side contained flat-bottom holes. Frequencies above 500 kHz were not effective for penetrating sample at thicker steps due to material attenuation.

E.3.2.3 Laboratory Setup

PEUT scans performed in the Test-Tech 3-axix scanning tank used the water-squirter method (see Figure E.3-9). For each panel, use of optimum water nozzle and column diameter achieved optimal SNR and defect detection (if defects existed).

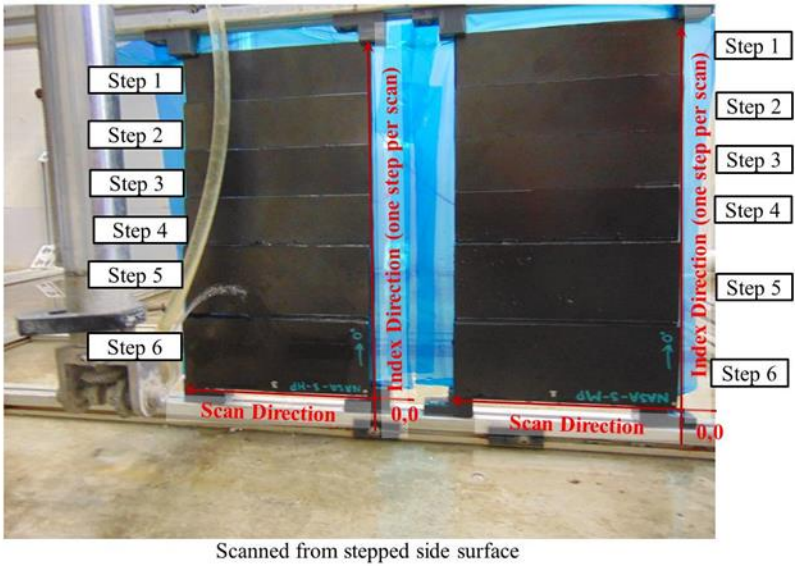

Figure E.3-9. PEUT setup in Test-Tech scanning tank.

E.3.2.4 Equipment List and Specifications:

- Test-Tech 3-axis scanning tank
- Olympus 5077PR Square Wave Pulser/Receiver
- Transducer Frequencies: (0.5, 1.0, and 2.25 MHz)

E.3.2.5 Settings

Table E.3-2. Equipment settings for 0.5 MHz scan.

Transducer	Brand	Model	Freq. (MHz)	Element Dia. (in.)	Water Column Dia (in.)			Outer Dia. (in)		
Transmitter	GE	Benchmark	0.5	0.5	0.5			0.5		
Pulser/Receiver	PRF	Voltage	Freq. (MHz)		HPF	LPF (MHz)	Rtune	Ttune	Attn	Range
Olympus	Ext	400	0.5		Out	Full BW	N/A	N/A	N/A	N/A
	Gain (dB)	"-14 for Steps 1-6								

Table E.3-3. Equipment settings for 1.0 MHz scan.

Transducer	Brand	Model	Freq. (MHz)	Element Dia. (in.)	Water Column Dia (in.)			Outer Dia. (in)		
Transmitter	Sonic	IBK I-2	1	0.5	0.375			0.5		
Pulser/Receiver	PRF	Voltage	Freq. (MHz)		HPF	LPF (MHz)	Rtune	Ttune	Attn	Range
Olympus	Ext	400	1.0		Out	Full BW	N/A	N/A	N/A	N/A
	Gain (dB)	3 for Steps 1,2,6		0 for Steps 3,4,5						

Table E.3-4. Equipment settings for 2.25 MHz scan.

Transducer	Brand	Model	Freq. (MHz)	Element Dia. (in.)	Water Column Dia (in.)			Outer Dia. (in)		
Transmitter	KB-Aerotech	Alpha	2.25	0.25	0.25					
Pulser/Receiver	PRF	Voltage	Freq. (MHz)		HPF	LPF (MHz)	Rtune	Ttune	Attn	Range
Olympus	Ext	200	2-2.25		Out	Full BW	N/A	N/A	N/A	N/A
	Gain (dB)	10 for Steps 1-6								

E.3.2.6 Inspection Results

Not all back-wall signals were detected for all measured frequencies as shown below. For higher frequency PEUT (1 and 2.25 MHz), thicker step panels were too thick and attenuating. Scans were performed and data quality was verified by producing C-scans for the different panels as shown below.

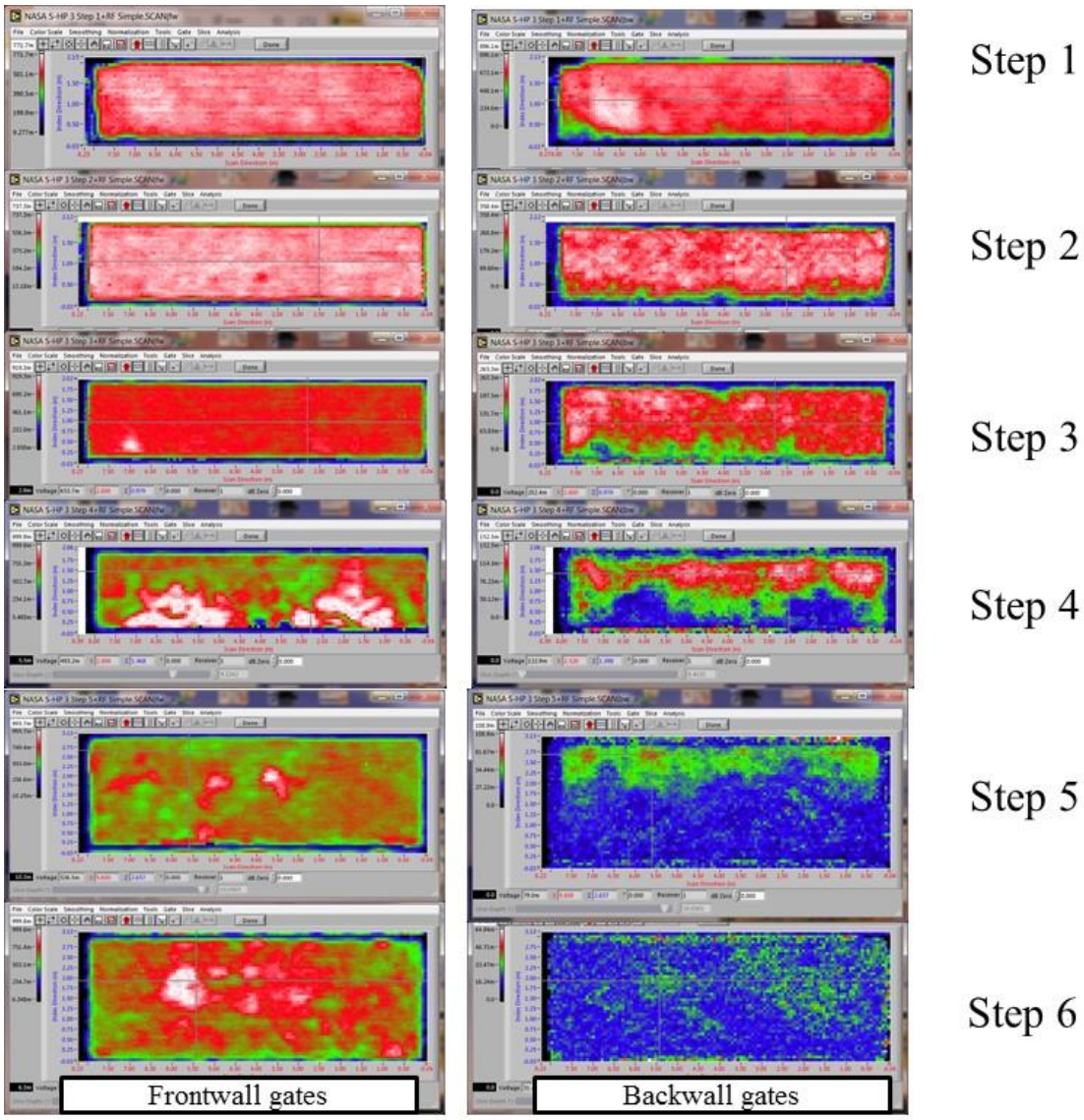

Figure E.3-10. PEUT C-scans at 500 kHz for Steps 1–6.

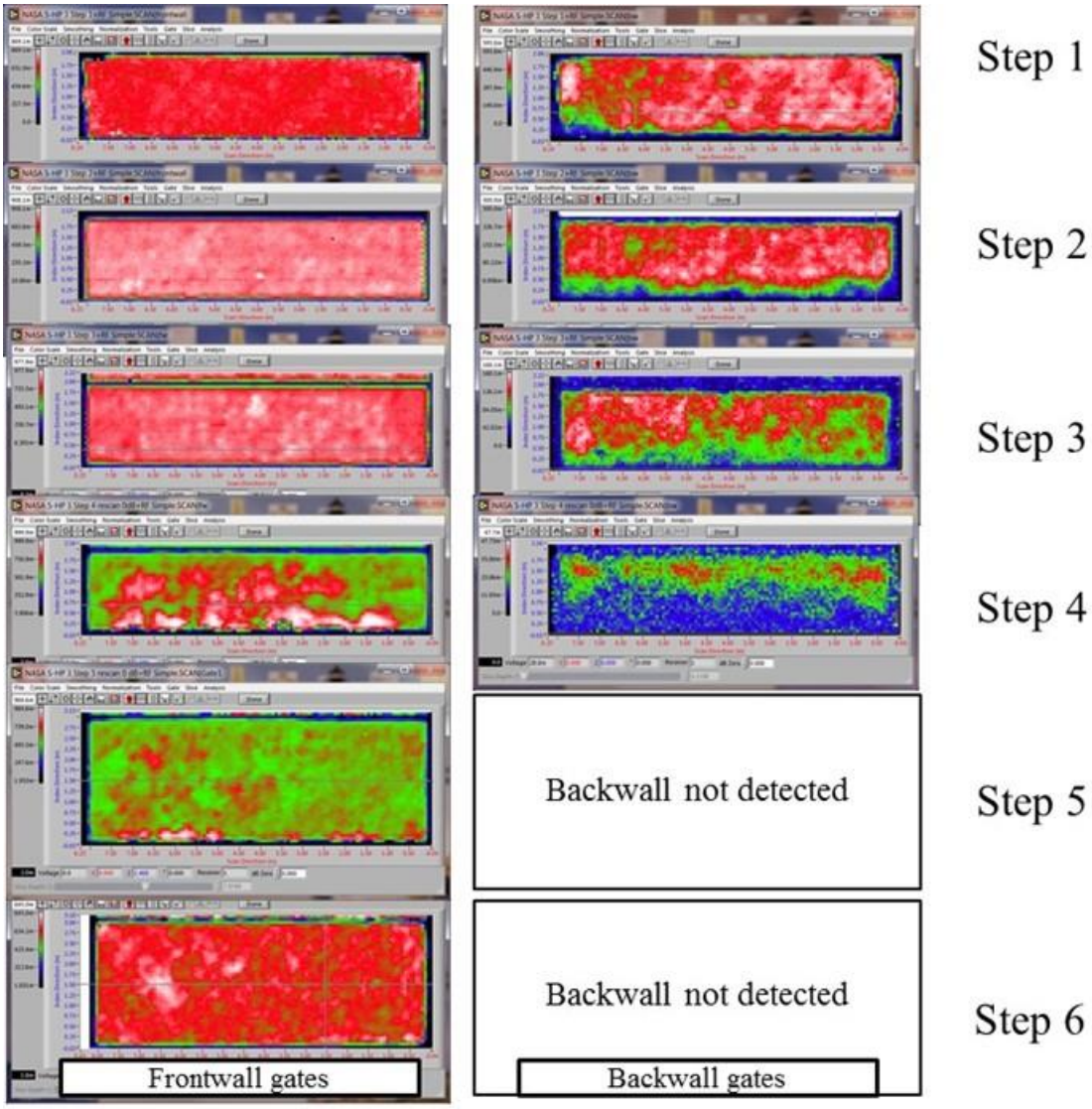

Figure E.3-11. PEUT scans at 1.0 MHz for Steps 1–6.

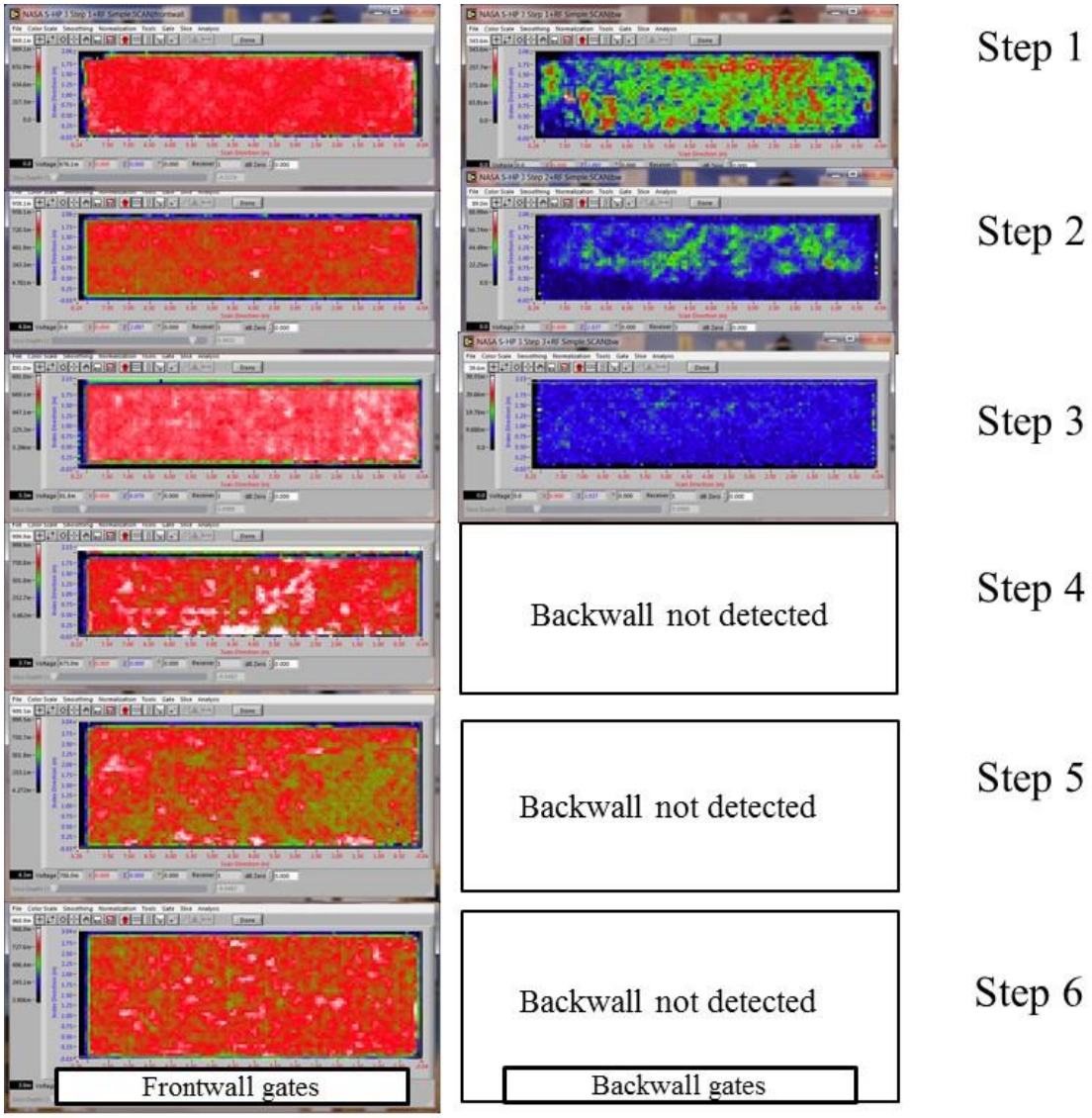

Figure E.3-12. PEUT C-scans at 2.25 MHz for Steps 1–6.

E.3.2.7 References

[1] Workman, Gary L, and Doron Kishoni. Nondestructive Testing Handbook. Third. Edited by Patrick O Moore. Vol. 7. American Society for Nondestructive Testing (ANST), 2007.

E.3.3 *Method: Single-Sided Infrared (IR) Thermography (SSIR)*

E.3.3.1 Partner: NGIS

E.3.3.2 Technique Applicability: ★☆☆

The thermal response produced by single-sided thermographic inspection is dominated by factors other than porosity. It was found that slight variations in thickness and localized thermal property variation dominated the surface temperature compared to material's porosity. For this reason, single-sided inspection is not recommend as a technique for discriminating porosity.

E.3.3.3 Laboratory Setup

Single-Sided Thermography images were acquired using a FLIR SC6000 IR camera setup. The thermal camera is mounted to the back of the flash hood and mounted in a fixed location on an optical table. The panel is held vertically within a fixture that slides across a linear track between captures in order to ensure total coverage. Paper light shields were constructed for the fixture to block flash spillover around the edges of the panel.

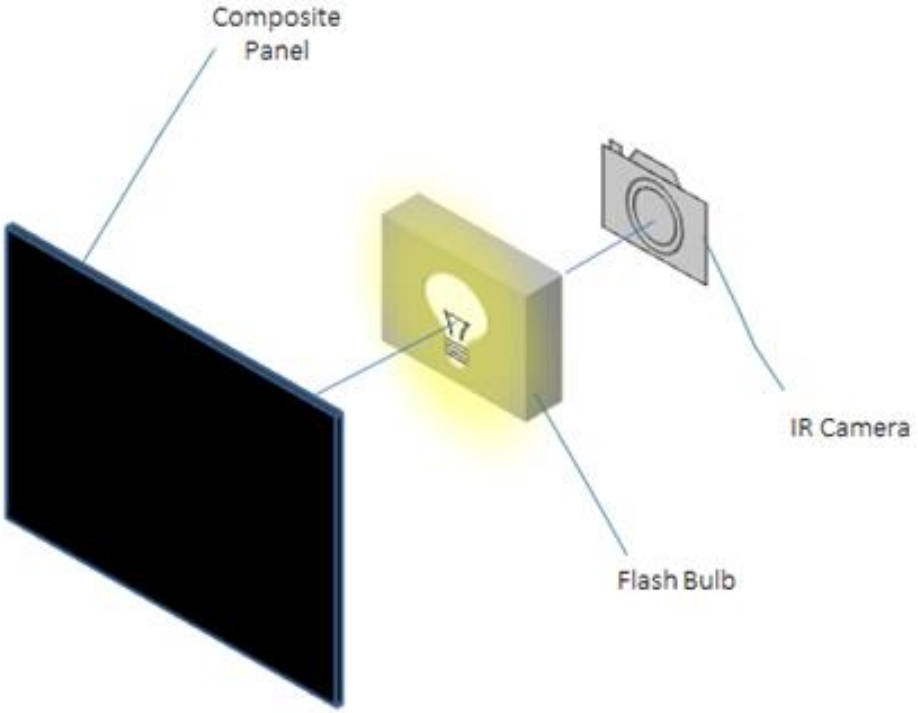

Figure E.3-13. Single-side thermography schematic.

Figure E.3-14. Photo of single-sided thermography setup.

E.3.3.4 Equipment List and Specifications:

- FLIR SC6000 IR camera, mid wavelength IR sensor (3.0–5.0 µm)
- Flash power supplies, hood, and lamps
- EchoTherm® V8 Software

E.3.3.5 Settings

Table E.3-5. Equipment settings for SSIR scan.

Flash Duration (ms)	30
Capture Elapsed Time (s)	7.95
Camera Frequency (Hz)	37.92
Integration Time (s)	2

E.3.3.6 Inspection Results

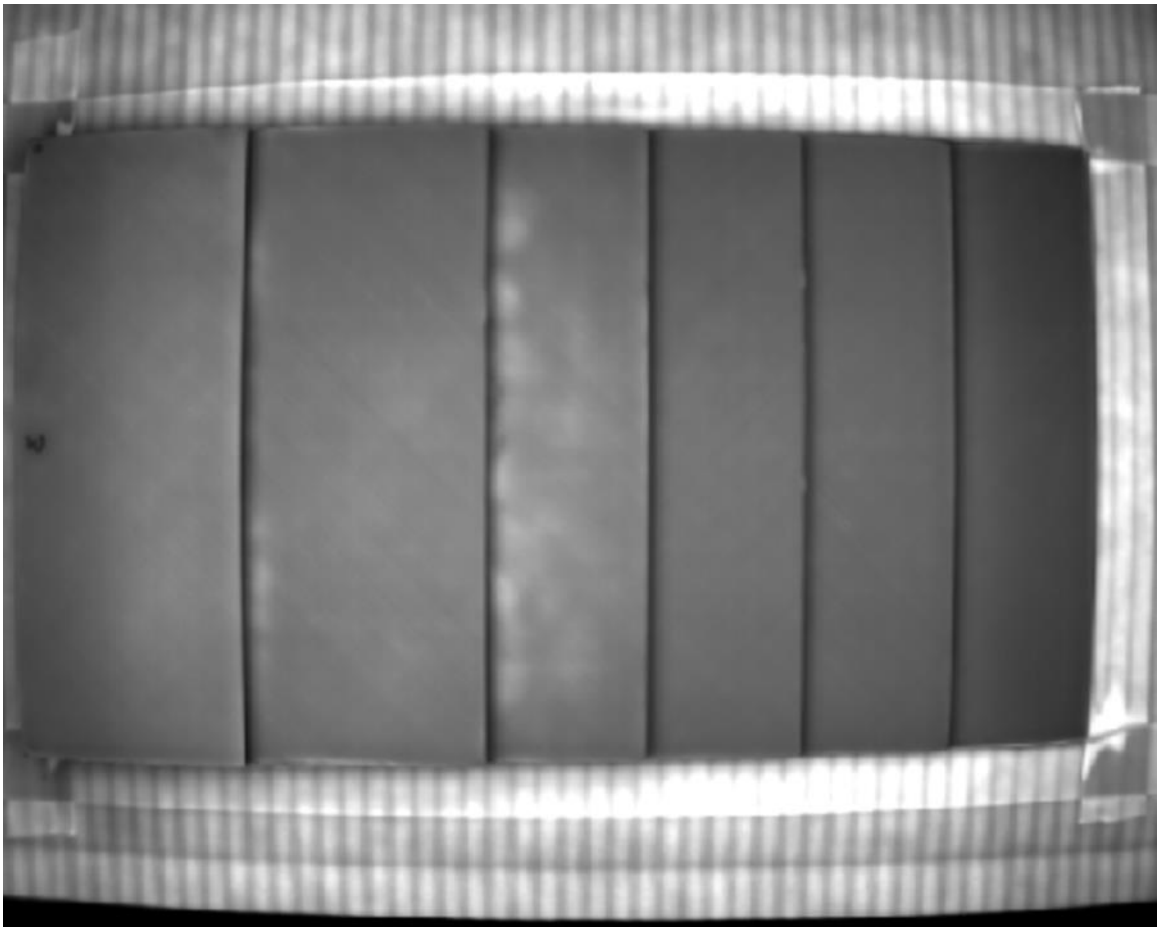

Figure E.3-15. Single-sided thermography image of Specimen #3.

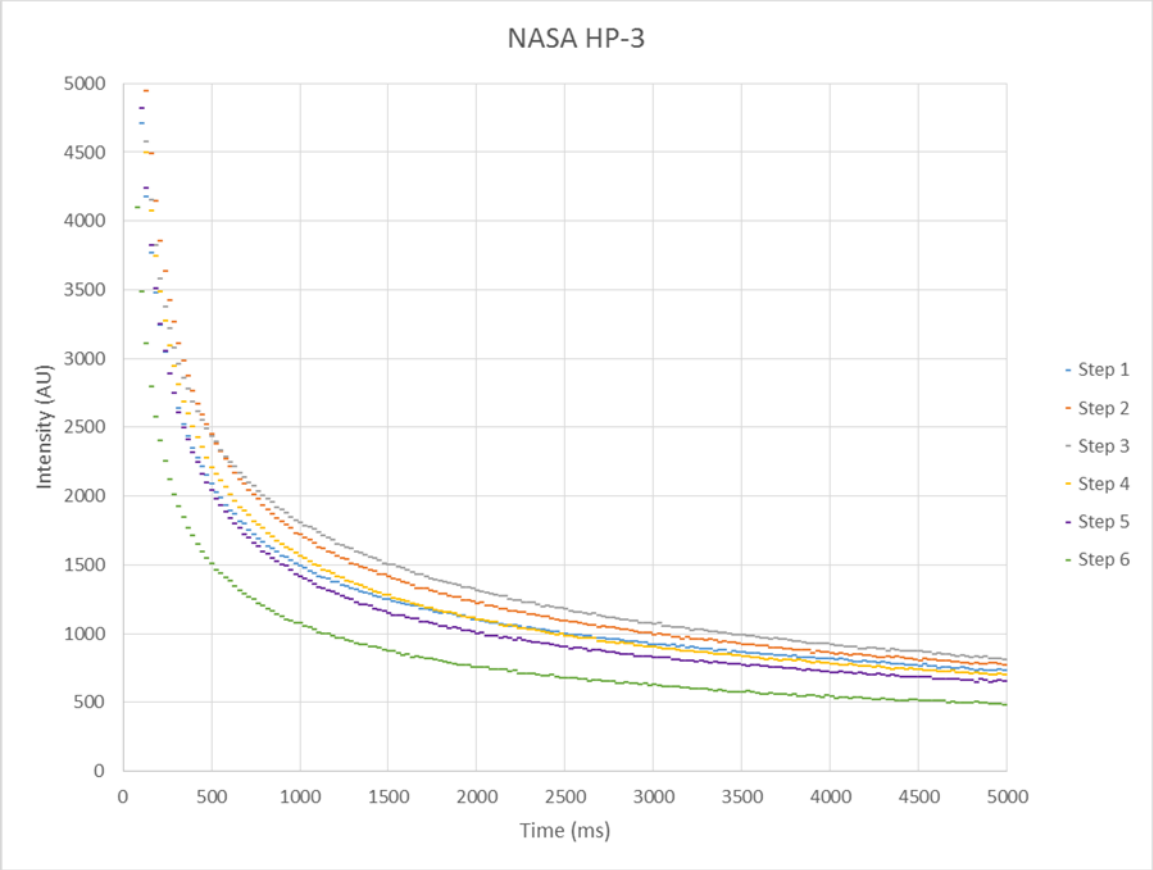

Figure E.3-16. Intensity curve showing heat dispersion over time for each step of Specimen #3.

E.3.3.7 References

[1] W.J. Parker; R.J. Jenkins; C.P. Butler; G.L. Abbott (1961). "Method of Determining Thermal Diffusivity, Heat Capacity and Thermal Conductivity". Journal of Applied Physics. 32 (9): 1679. Bibcode:1961JAP....32.1679P. doi:10.1063/1.1728417

E.3.4 *Method: Through-Transmission Infrared Thermography (TTIR)*

E.3.4.1 Partner: NGIS

E.3.4.2 Technique Applicability: ★★☆

E.3.4.3 Laboratory Setup

TTIR images were acquired using a FLIR SC6000 IR camera setup. The flash hood is mounted in a fixed location on an optical table. The thermal camera is mounted on a tripod with the panel between it and the flash hood. The panel is held vertically within a fixture that slides across a linear track between captures in order to ensure total coverage. Paper light shields were constructed for the fixture to block flash spillover around the edges of the panel.

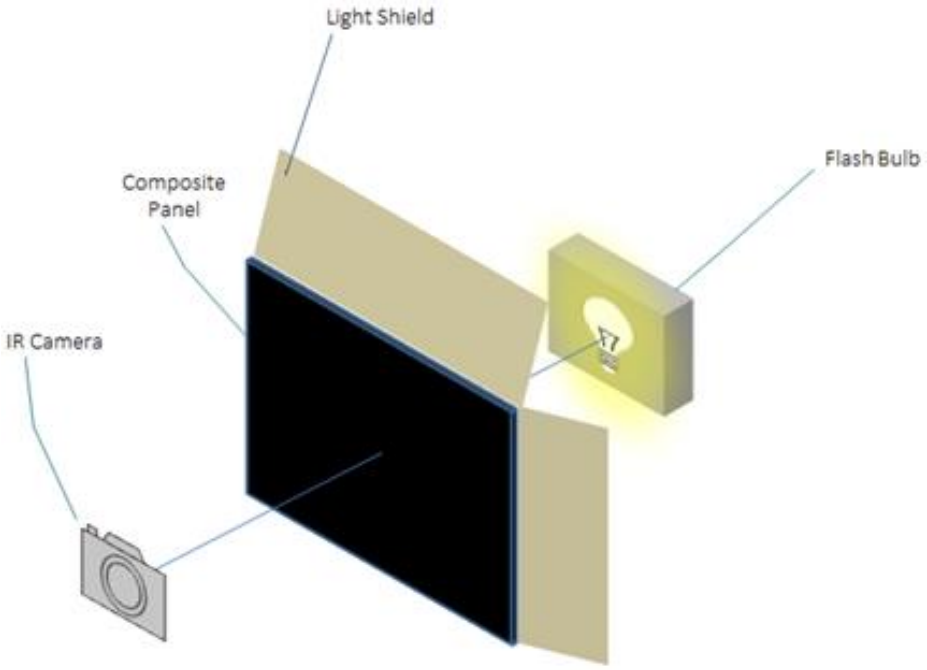

Figure E.3-17. TTIR schematic.

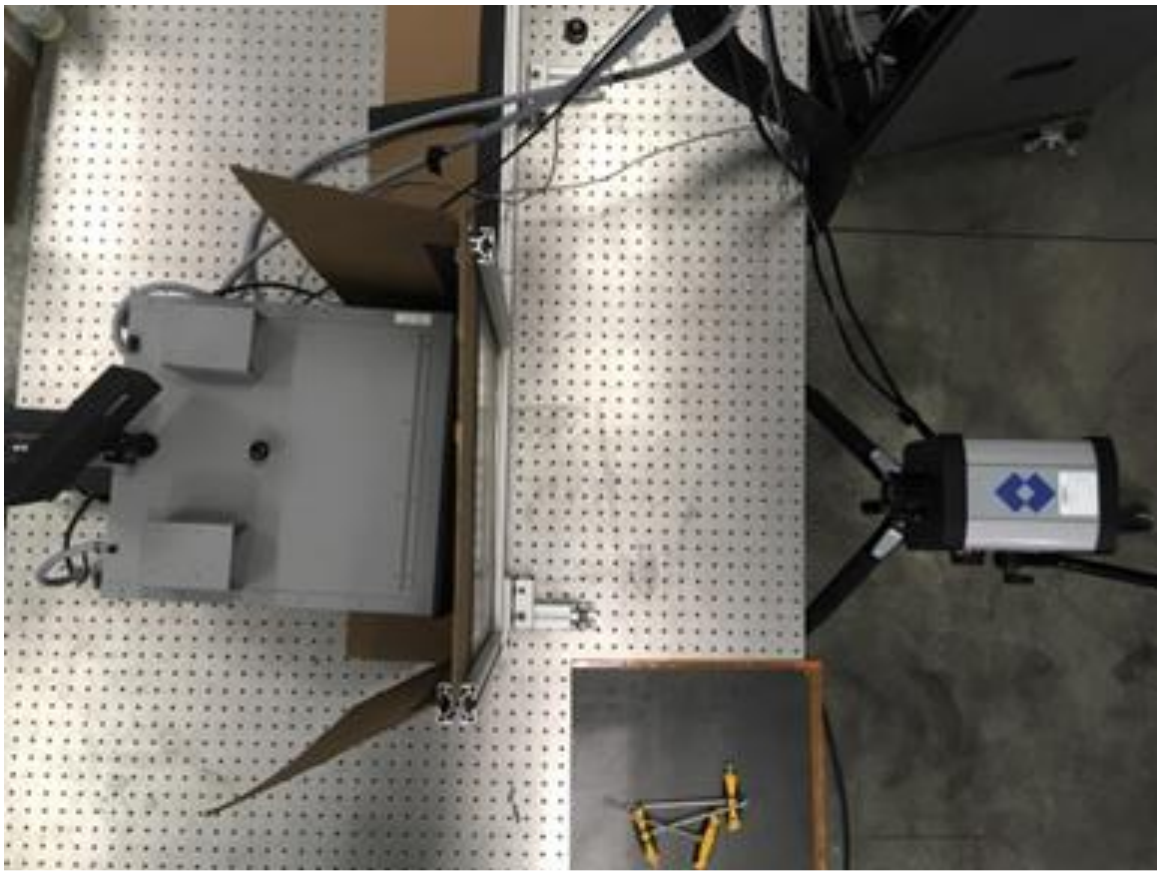

Figure E.3-18. Photo of TTIR setup.

E.3.4.4 Equipment List and Specifications:

- FLIR SC6000 IR camera, mid wavelength IR sensor (3.0–5.0 µm)
- Flash power supplies, hood, and lamps
- EchoTherm® V8 Software

E.3.4.5 Settings

Table E.3-6. Equipment settings for TTIR scan.

Panel Thickness (mm)	3.41 (Step 1)
Flash Duration (ms)	30
Capture Elapsed Time (s)	19.85
Camera Frequency (Hz)	6.56
Integration Time (s)	2

E.3.4.6 Inspection Results

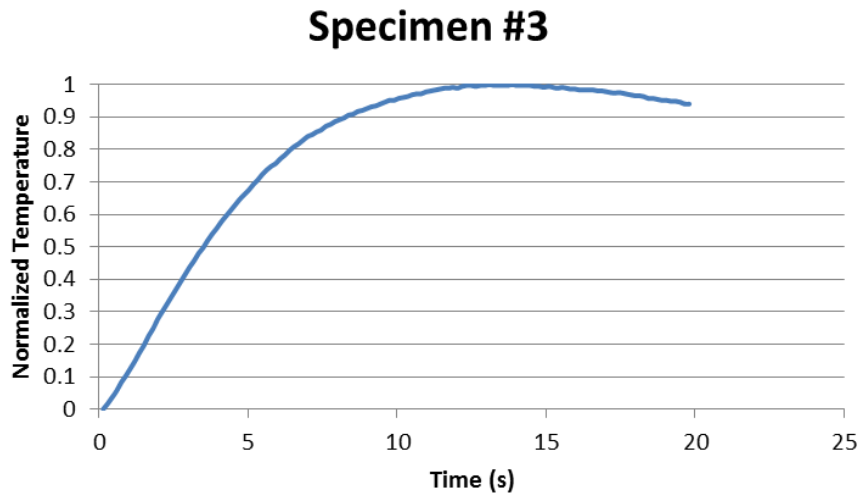

Figure E.3-19. Temperature curve showing the dispersion of heat over time during image capture of Step 1.

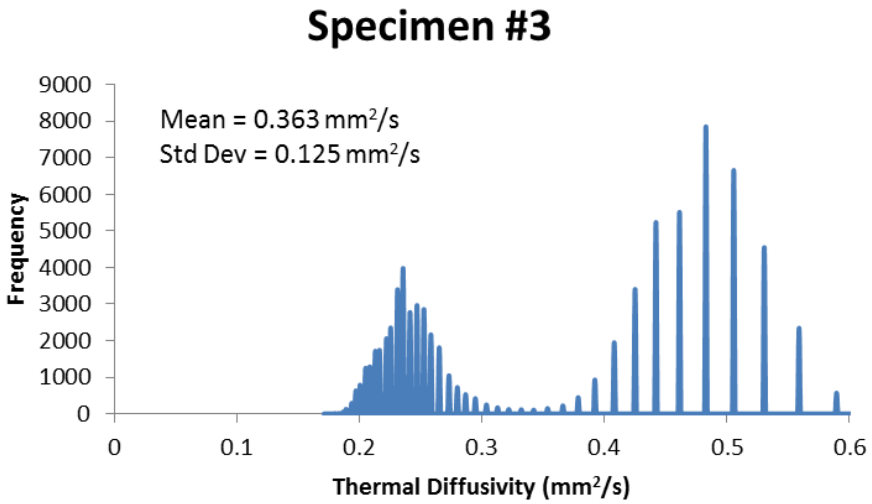

Figure E.3-20. Histogram showing frequency of thermal diffusivity values. Expansive point spread shows inconsistent levels of porosity throughout Step 1 of the panel and a higher standard deviation shows high porosity levels.

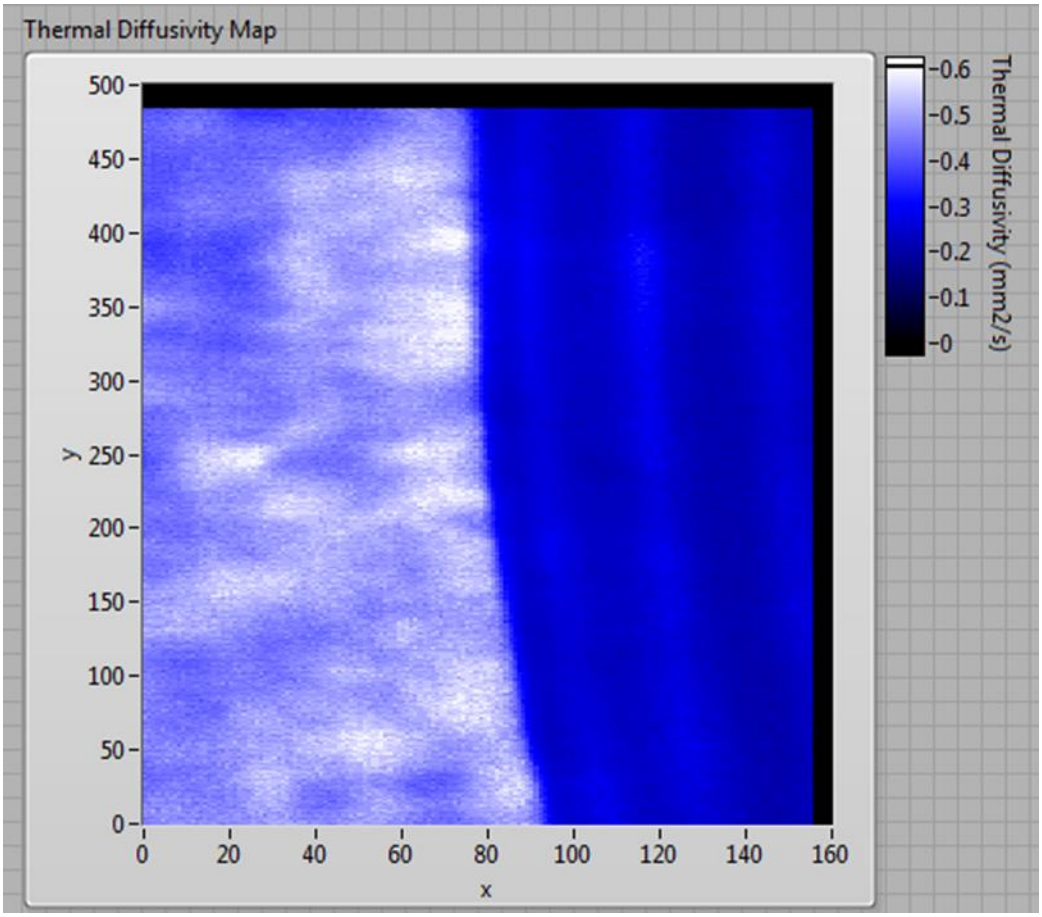

Figure E.3-21. Image of thermal diffusivity post processing. Dark patches show areas of high porosity. Smooth blue area starting at x = 85 is overlap with thicker step.

E.3.4.7 References

[1] W.J. Parker; R.J. Jenkins; C.P. Butler; G.L. Abbott (1961). "Method of Determining Thermal Diffusivity, Heat Capacity and Thermal Conductivity". Journal of Applied Physics. 32 (9): 1679P.

E.4 Specimen #4: NASA-W5D – Not Tested

Structure	Material	Details	Dimensions (inches)	Partner Methods
NASA-W-5D	IM7/8552	Height: 0.25–1.0 inch, 5° slope, delaminations start-end of slope	12 × 3 × 1.5	Not tested

E.5 Specimen #5: NASA-W-20D – Not Tested

Structure	Material	Details	Dimensions (inches)	Partner Methods
NASA-W-20D	IM7/8552	Height: 0.25–1.0 inch, 20° slope, delaminations start-end of slope	12 × 3 × 1.1	Not tested

E.6 Specimen #6: NASA-W-35D – Not Tested

Structure	Material	Details	Dimensions (inches)	Partner Methods
NASA-W-35D	IM7/8552	Height: 0.25–1.0 inch, 35° slope, delaminations start-end of slope	12 × 7 × 1.5	Not tested

E.7 Specimen #7: NASA-W-IL-20D – Not Tested

Structure	Material	Details	Dimensions (inches)	Partner Methods
NASA-W-IL-5D	IM7/8552	Height: 0.25–1.0 inch, 5° slope, delaminations start-end of slope	12 × 3 × 1.5	Not tested

E.8 Specimen #8: NASA-W-IL-20D – Not Tested

Structure	Material	Details	Dimensions (inches)	Partner Methods
NASA-W-IL-20D	IM7/8552	Height: 0.25–1.0 inch, 20° slope, delaminations start-end of slope	12 × 3 × 1.1	Not tested

E.9 Specimen #9 – Not manufactured

E.10 Specimen #10: NASA-W-5MP

Structure	Material	Details	Dimensions (inches)	Partner Methods	
Uni-ply (0/90/45)	IM7/8552	Wedge Interleaved 5° with medium porosity	12 × 3 × 1.5	NASA	E.10.1 XCT

Figure E.10-1. Photographs of Specimen #10: NASA-W-5MP.

E.10.1 *Method: X-ray Computed Tomography (XCT)*

E.10.1.1 Partner: NASA

E.10.1.2 Technique Applicability: ★★★

XCT is capable of imaging the medium porosity in this specimen.

E.10.1.3 Laboratory Setup

The microfocus XCT system at NASA LaRC is a commercially available Avonix (Nikon C2) Metrology System designed for high-resolution NDE inspections. The system is an advanced microfocus X-ray system, capable of resolving details down to 5 μm, and with magnifications up to 60X. Supplied as complete, the system is a large-dimension radiation enclosure with X-ray source, specimen manipulator, and an amorphous silica detector, as shown in Figure E.10-2. The imaging controls are housed in a separate control console. The detector is a Perkin-Elmer, 16-bit, amorphous-silicon digital detector with a 2000 × 2000-pixel array.

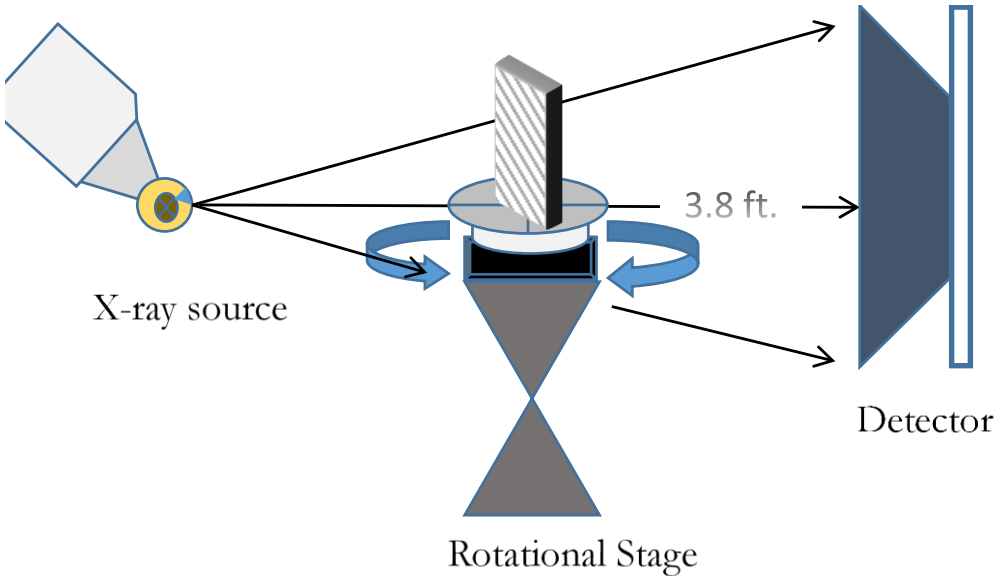

Figure E.10-2. XCT system components.

A consistent Cartesian coordinate system is used to define slice direction as illustrated in Figure E.10-3. Slices normal to the X-, Y-, and Z-directions are shown in Figure E. 10-3a, b, and c, respectively.

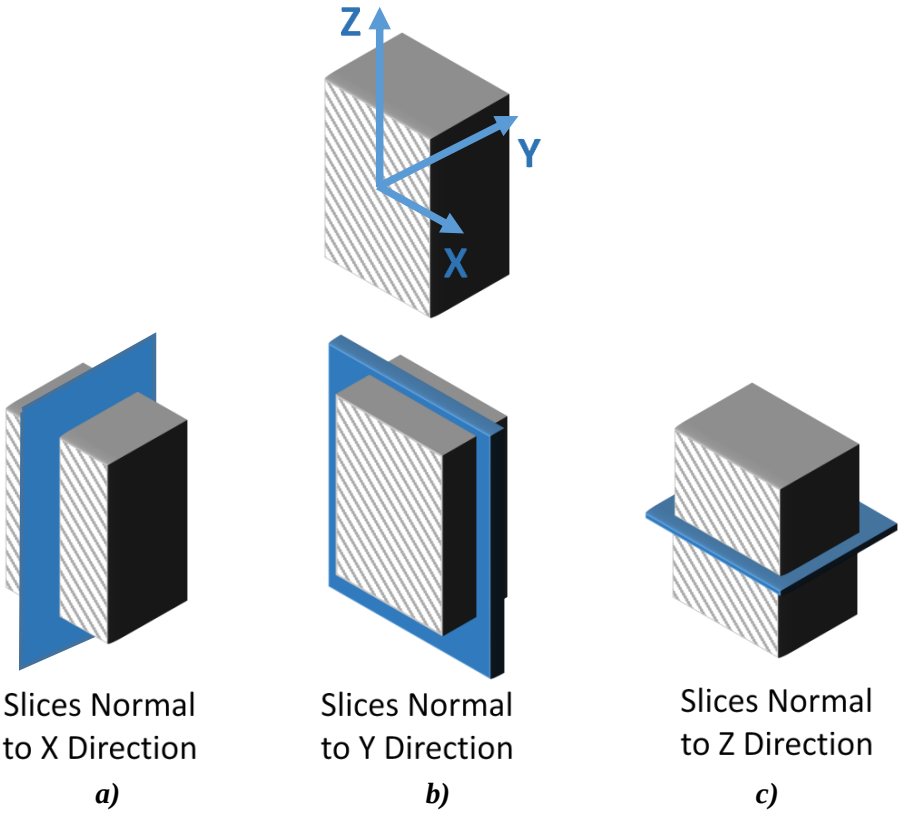

Figure E.10-3. Slice direction nomenclature.

E.10.1.4 Equipment List and Specifications:

- Avonix 225 CT System
- 225 kV microfocus X-ray source with 5 µm focal spot size
- 15 or 30 kg Capacity, 5-axis, fully programmable manipulator
- Detector: Perkin Elmer XRD 1621 – 2000 × 2000 pixels with 200 µm pitch
- 10 µm spatial resolution for specimens 1.5 cm wide
- Thin panels 10 × 10 inches – full volume 200 µm spatial resolution

E.10.1.5 Settings

Table E.10-1. Data collection settings.

Source Energy	150 kV
Current	50 µA
Magnification	1.65 X
Filter	NF
# Rotational angles	3142
Exposure time / frame	1.0 sec
Max Histogram Grey Level	30 K
# Averages	8
Resolution (µm)	120.947 µm
Array Dimensions (pixels)	Set 1: 1999 × 362 × 1998 Set 2: 1998 × 686 × 1997

The specimen is placed vertically (rotated about the smallest dimension) on the rotational stage located between the radiation source and the detector. The rotational stage is computer controlled and correlated to the position of the sample. As the sample is rotated the full 360° (~0.11° increments), the detector collects radiographs at each rotated angle as the X-ray path intersects the sample. 3D reconstruction of the collection of radiographs produces a volume of data that is viewed along any plane in the volume. The closer the sample is placed to the X-ray source, the higher the spatial resolution that can be obtained.

E.10.1.6 Inspection Results

Section A

Specimen #10, NASA-W-5MP, is a wedge panel fabricated from IM7/8552, with an objective of achieving medium porosity. XCT was performed on this specimen in NASA LaRC's CT system with the settings defined in Section E.10.1.5. Several instances of delaminations and gross porosity are easily viewed in the CT slices corresponding to the different viewing directions, as highlighted in Figure E.10-4.

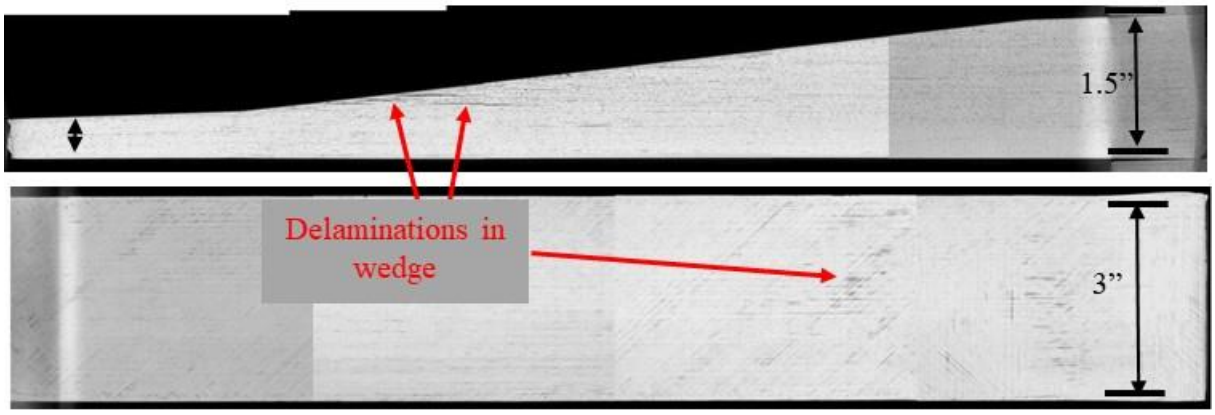

Figure E.10-4. CT slices from the y-direction (bottom) and x-direction (top) showing porosity and delaminations within the sample.

From XCT analysis, there are a multitude of confirmed porosity spots within the specimen. This porosity, though still seen in the y-direction are most readily identified in the x and z directions as shown in Figure E.10.5. The darker regions represent air gaps as the bulk material is much denser and therefore shows up lighter on the images. The porosity pervades nearly all slices of the specimen when viewed from these directions.

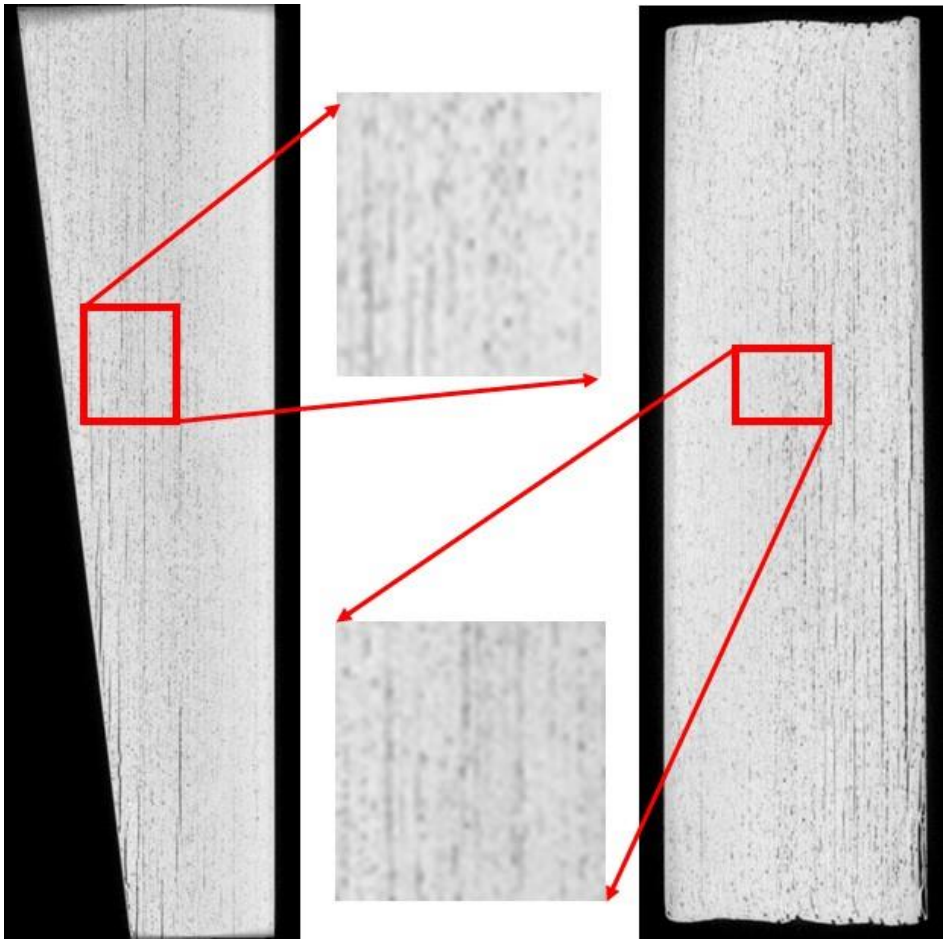

Figure E.10-5. CT slices from the x-direction (left) and z-direction (right) showing close views of porosity and delaminations within the sample.

Section B

Semantic CT Image Segmentation Technique:

The developed semantic CT image segmentation technique, originally designed at NASA LaRC, applies the CNN to identify and segment cracks and delamination in carbon fiber due to impact. The segmentation is done on the specimens' CT scan grayscale images. This method was first developed by D.T. Delelegn [1] as his master's thesis and then improved as a NASA white paper.

There are two implemented CNN models, each identifying the two damage types separately (i.e., crack and delamination). The first model easily identifies delamination, whereas the second is optimized to detect cracks and 'linear-type' damage. Each model prediction outputs are floating numbers between (0,1) indicating how likely an area is damaged. Class label one representing a highest damage prediction certainty while zero for a no-damage area. To seek the most damaged area in the material, this probabilistic prediction value of an area-damage indication is used.

The prediction is done on the CT images with a 4 × 4 window (patch) size. Then, the predicted class labels for each patch from the two models are combined as the Red (crack) and the Green (delamination) channels of the RGB color model representing the two damage types in different colors. For further reading, refer D.T. Delelegn [1].

This segmentation technique is able to easily point out cracks or linear damage that are collocated with a delamination. This is because that the prediction of the two models are represented in the different channels of the RGB color model.

While originally developed to detect impact damage, the method was applied to ACP Handbook standards (porosity, delamination, AFP defects, etc.) with varying degrees of success. Here, the method is applied to handbook specimen #10, which is a 12 × 3 × 1.5-inch wedge configuration with medium porosity, which is easily identified in the delaminations shown in Figures E.10-6 and E.10-7.

Segmentation Output:

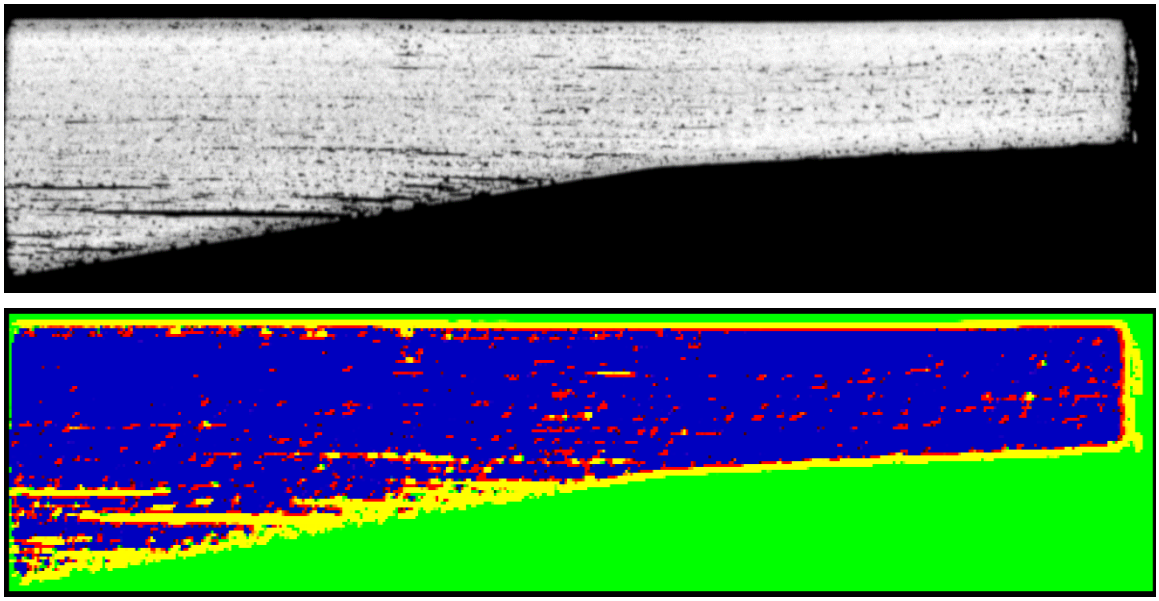

Figure E.10-6. (Top) XCT scan viewed from the y-normal direction. (Bottom) defect detection using CNN segmentation of the same slice of Specimen #10.

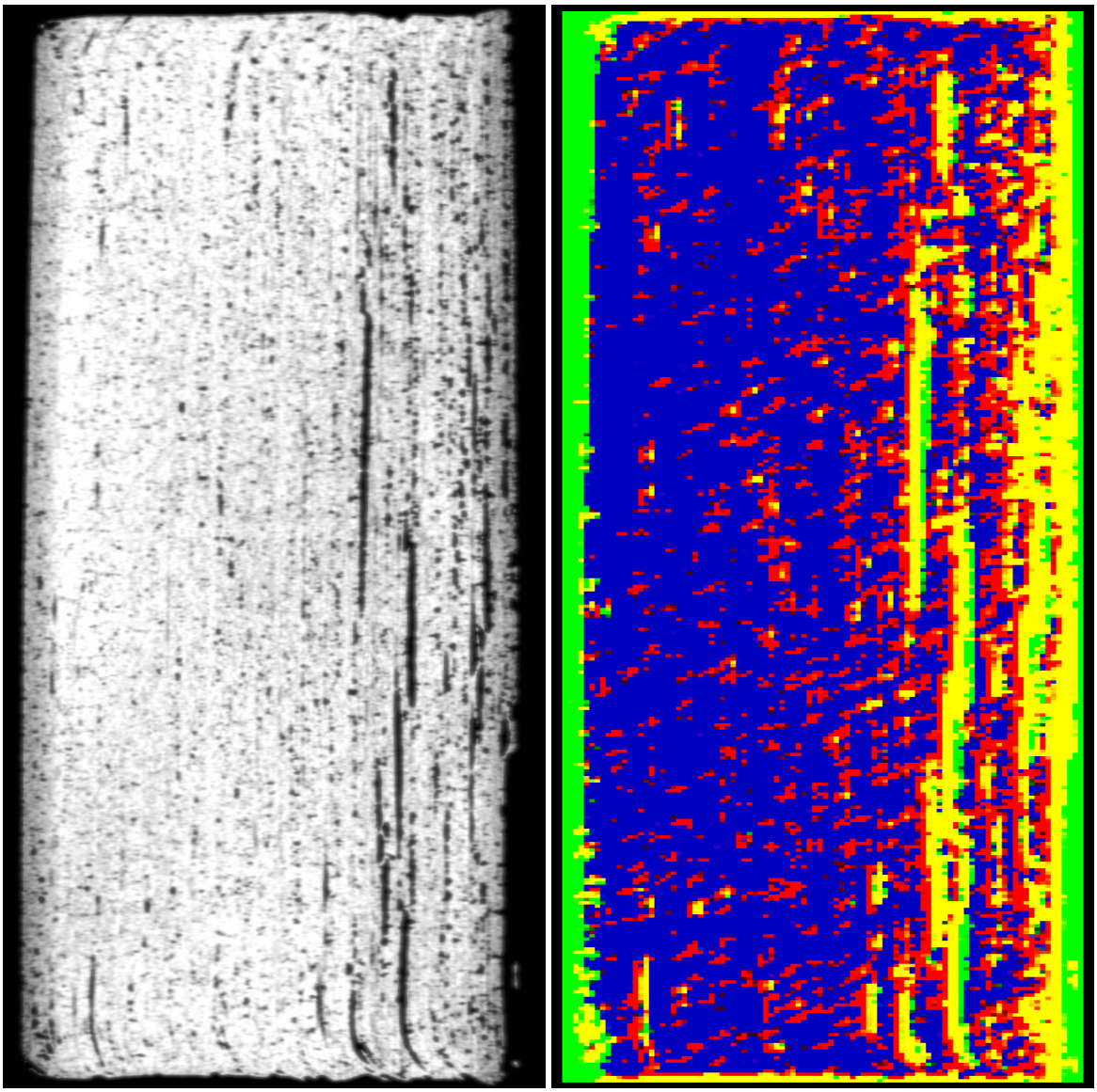

Figure E.10-7. Segmentation of a specimen from Figure E.10-5.

E.10.1.7 References

[1] Delelegn, Desalegn Temesgen, "Non-destructive Evaluation for Composite Material," Master of Science Thesis, Old Dominion University, August 2018

E.11 Specimen #11: NASA-W-IL-5D

Structure	Material	Details	Dimensions (inches)	Partner Methods	
Uni-ply (0/90/45)	IM7/8552	Wedge Step 5° with defects	12 × 3 × 1.5	NASA	E.11.1 XCT

Figure E.11-1. Photographs of Specimen #11: NASA-W-IL-5D.

E.11.1 *Method: X-ray Computed Tomography (XCT)*

E.11.1.1 Partner: NASA

E.11.1.2 Technique Applicability: ★★★

XCT is capable of imaging the medium porosity in this specimen.

E.11.1.3 Laboratory Setup

The microfocus XCT system at NASA LaRC is a commercially available Avonix (Nikon C2) Metrology System designed for high-resolution NDE inspections. The system is an advanced microfocus X-ray system, capable of resolving details down to 5 μm, and with magnifications up to 60X. The system is supplied as a complete, large-dimension radiation enclosure, with X-ray source, specimen manipulator, and an amorphous silica detector as shown in Figure E.11-2. The imaging controls are housed in a separate control console. The detector is a Perkin-Elmer, 16-bit, amorphous-silicon digital detector with a 2000 × 2000-pixel array

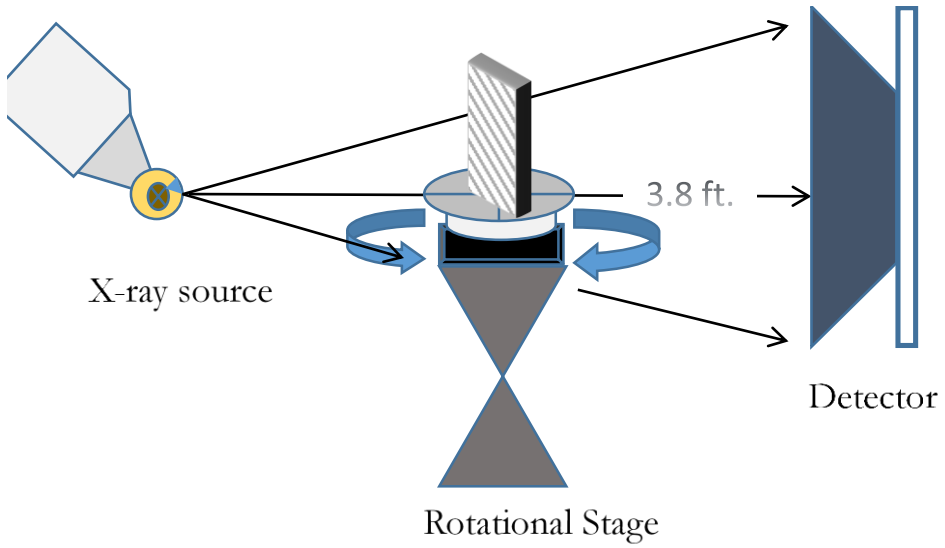

Figure E.11-2. XCT system components.

A consistent Cartesian coordinate system is used to define slice direction as illustrated in Figure E.11-3. Slices normal to the X-, Y-, and Z-directions are shown in Figure E.11-3a, b, and c, respectively.

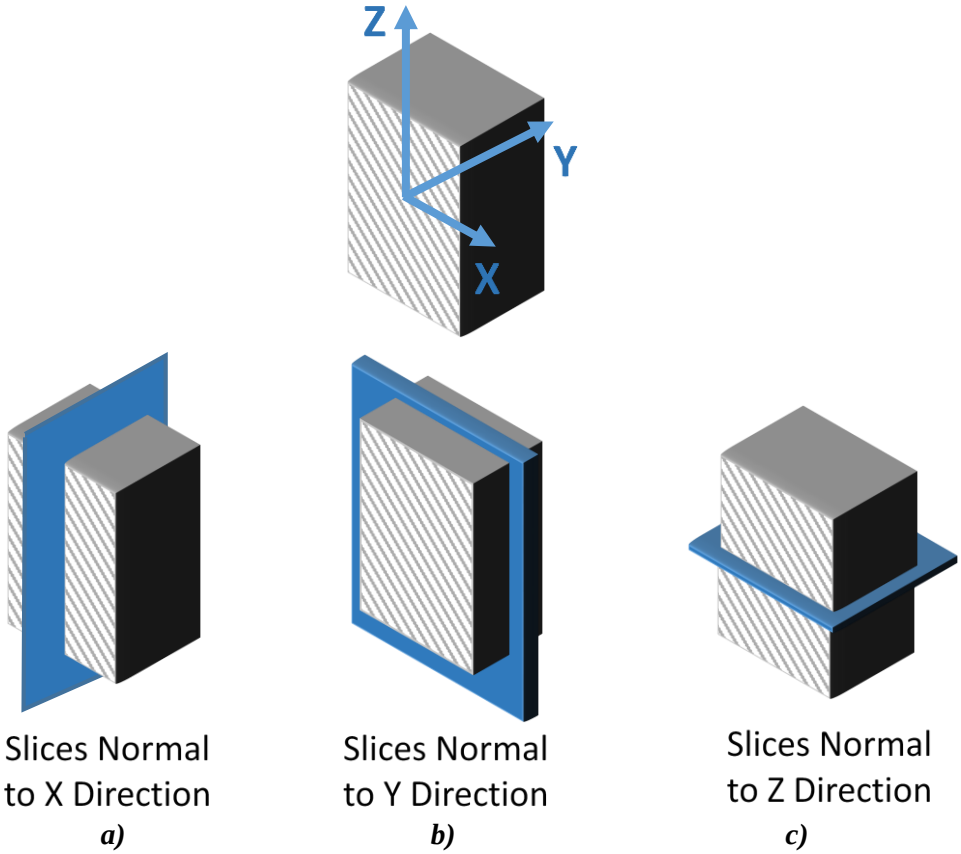

Figure E.11-3. Slice direction nomenclature.

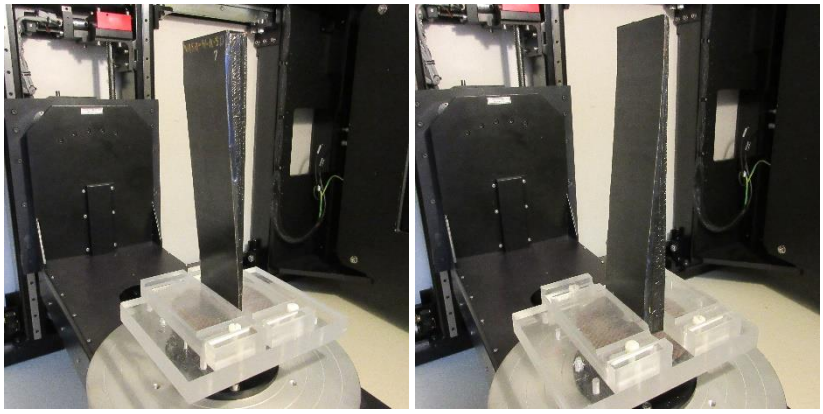

Figure E.11-4. Specimen orientation within the detector.

E.11.1.4 Equipment List and Specifications:

- Avonix 225 CT System
- 225 kV microfocus X-ray source with 5 µm focal spot size
- 15 or 30 kg Capacity, 5-axis, fully programmable manipulator
- Detector: Perkin Elmer XRD 1621 – 2000 × 2000 pixels with 200 µm pitch
- 10 µm spatial resolution for specimens 1.5 cm wide
- Thin panels 10 × 10 inches – full volume 200 µm spatial resolution

E.11.1.5 Settings

Table E.11-1. Data collection settings.

Source Energy	150 kV
Current	50 µA
Magnification	1.65 X
Filter	NF
# Rotational angles	3142
Exposure time / frame	1.0 sec.
Max Histogram Grey Level	30 K
# Averages	8
Resolution (µm)	120.947 µm
Array Dimensions (pixels)	Set 1: 1999 × 362 × 1998 Set 2: 1998 × 686 × 1997

The specimen is placed vertically (rotated about the smallest dimension) on the rotational stage located between the radiation source and the detector. The rotational stage is computer controlled and correlated to the position of the sample. As the sample is rotated the full 360° (~0.11° increments), the detector collects radiographs at each rotated angle as the X-ray path intersects the sample. Three-dimensional reconstruction of the collection of radiographs produces a volume of data that can then be viewed along any plane in the volume. The closer the sample can be placed to the X-ray source, the higher the spatial resolution that can be obtained.

E.11.1.6 Inspection Results

Section A

Specimen #11, NASA-W-5MP, is a wedge panel fabricated from IM7/8552, with an objective of achieving medium porosity. XCT was performed on this specimen in NASA LaRC's CT system with the settings defined in Section E.11.1.5. Several instances porosity are easily viewed in the CT slices corresponding to the different viewing directions, as highlighted in Figure E.11-5.

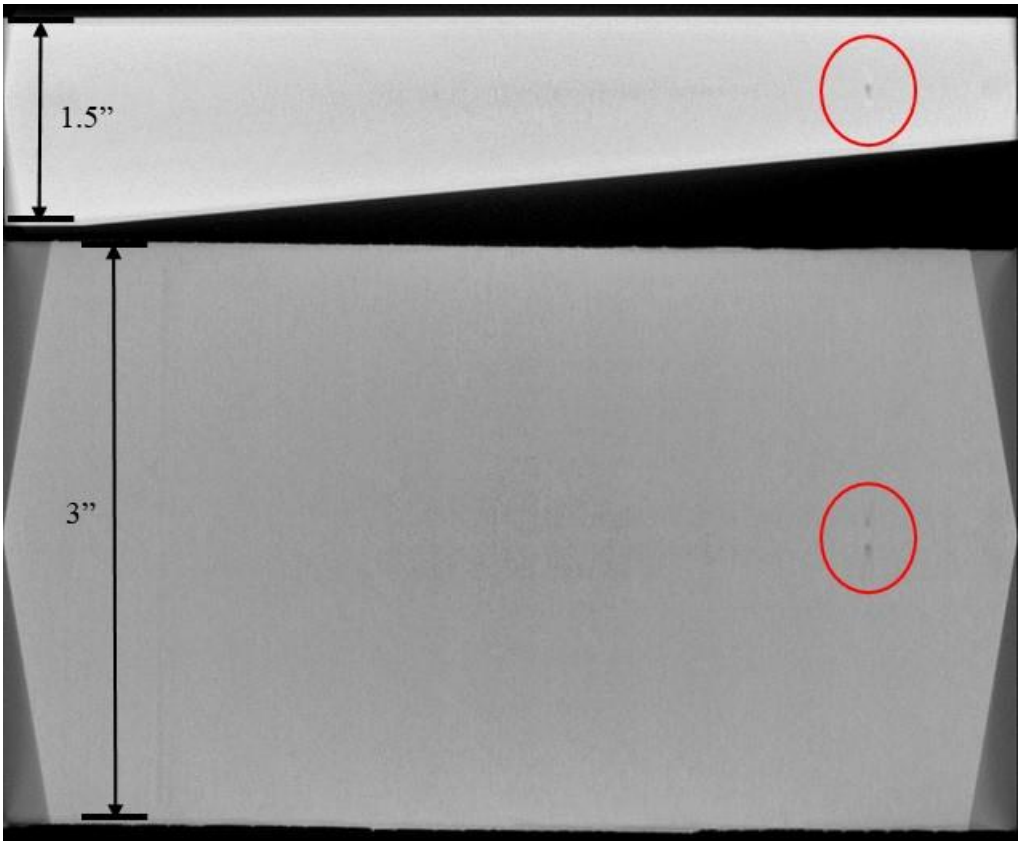

Figure E.11-5. CT slices from the y-direction (bottom) and x-direction (top) showing porosity within the sample.

From XCT analysis, there are over 10 instances of confirmed porosity spots within the specimen. The darker regions represent air gaps as the bulk material is much denser. The porosity is detected at all depths in the specimen as shown in Figure E.11-6.

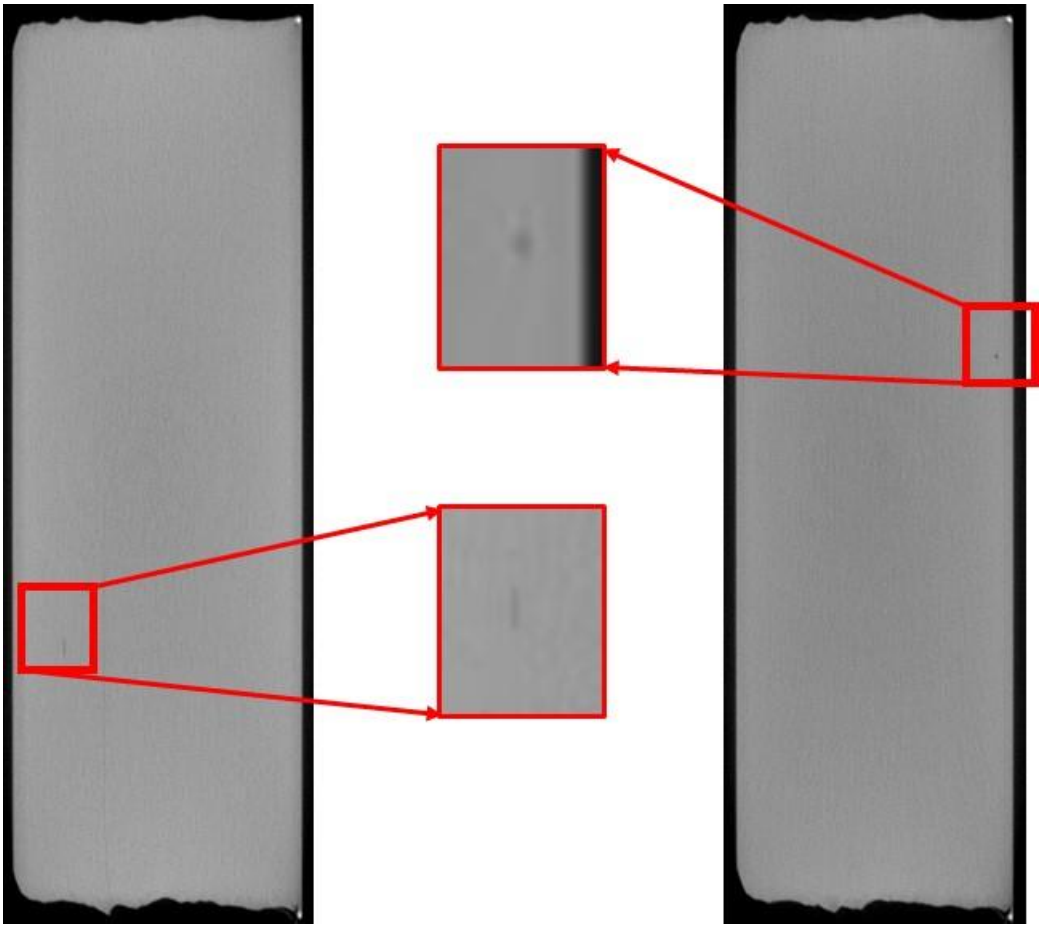

Figure E.11-6. XCT slices from the z-direction showing close views of porosity and within the sample.

Section B

Semantic CT Image Segmentation Technique:

The developed semantic CT image segmentation technique, originally designed at NASA LaRC, applies the CNN to identify and segment cracks and delamination in carbon fiber due to impact. The segmentation is done on the specimens' CT scan grayscale images. This method was first developed by D.T. Delelegn [1] as his master's thesis and then improved as a NASA white paper.

There are two implemented CNN models, each identifying the two damage types separately (i.e., crack and delamination). The first model easily identifies delamination, whereas the second is optimized to detect cracks and 'linear-type' damage. Each model prediction outputs are floating numbers between (0,1) indicating how likely an area is damaged. Class label one representing a highest damage prediction certainty while zero for a no-damage area. To seek the most damaged area in the material, this probabilistic prediction value of an area-damage indication is used.

The prediction is done on the CT images with a 4 × 4 window (patch) size. Then, the predicted class labels for each patch from the two models are combined as the Red (crack) and the Green (delamination) channels of the RGB color model representing the two damage types in different colors. For further reading, refer D.T. Delelegn [1].

This segmentation technique is able to easily point out cracks or linear damage that are collocated with a delamination. This is because that the prediction of the two models are represented in the different channels of the RGB color model.

While originally developed to detect impact damage, the method was applied to ACP Handbook standards (porosity, delamination, AFP defects, etc.) with varying degrees of success. Here, the method is applied to handbook specimen #11, which is a 12 × 3 × 1.5-inch wedge configuration with medium porosity, which is easily identified in the delaminations shown in Figures E.11-7 and E.11-8.

Segmentation Output:

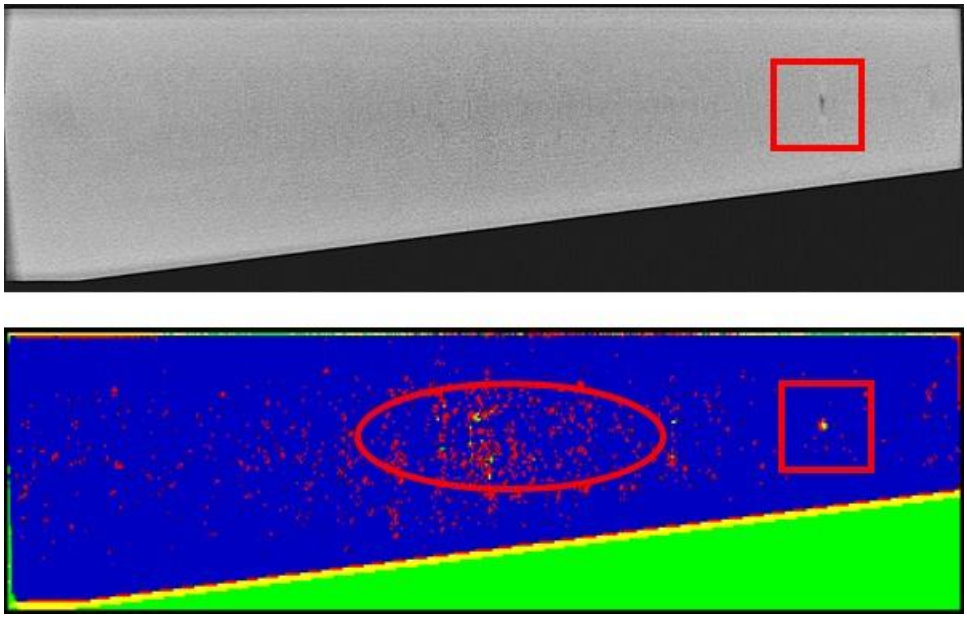

Figure E.11-7. (Top) X-ray CT slice of specimen #11 in the x-normal view. (Bottom) CNN segmentation of same slice.
The porosity identified by the SME (red box) is detected, as well as a large region of scattered indications indicative of porosity (red oval) not detected by the SME.

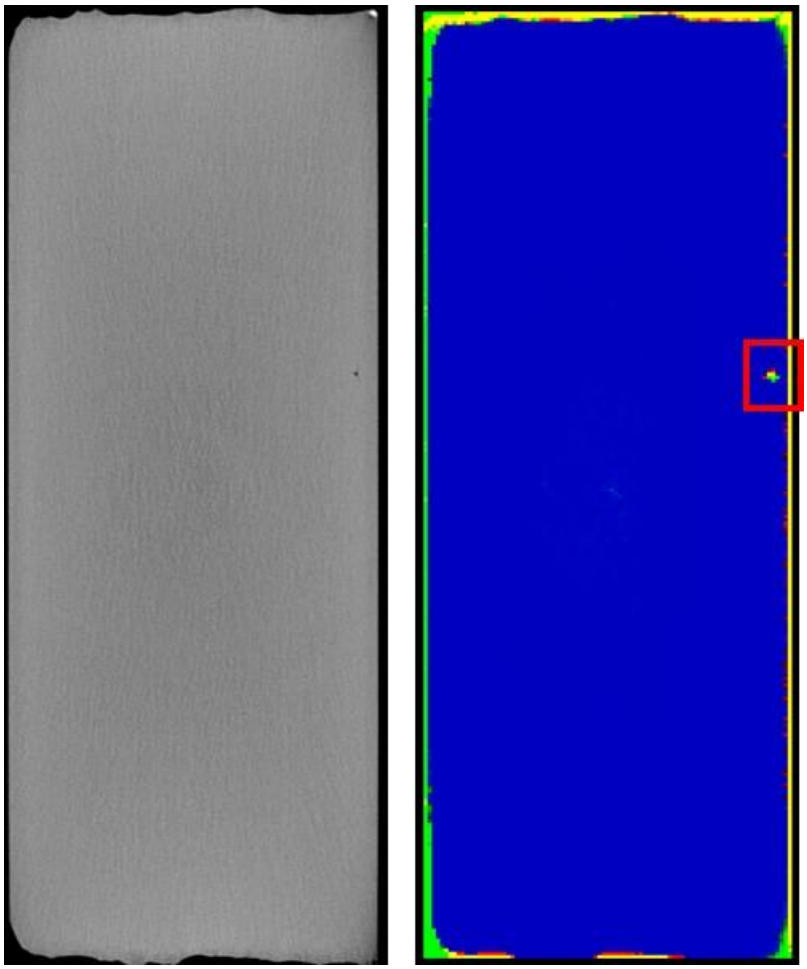

Figure E.11-8. (Left) X-ray CT slice of specimen #11 in the z-normal view. (Right) CNN segmentation results of same slice.
The porosity identified by the SME (red box) is detected. No other regions of porosity detected by segmentation algorithm

E.11.1.7 References

[1] Delelegn, Desalegn Temesgen, "Non-destructive Evaluation for Composite Material," Master of Science Thesis, Old Dominion University, August 2018

E.12 Specimen #12: NASA-W-20MP

Structure	Material	Details	Dimensions (inches)	Partner Methods	
Uni-ply (0/90/45)	IM7/8552	Wedge Interleaved 20° with medium porosity	12 × 3 × 1	NASA	E.12.1 XCT

Figure E.12-1. Photographs of Specimen #12: NASA-W-20MP.

E.12.1 *Method: X-ray Computed Tomography (XCT)*

E.12.1.1 Partner: NASA

E.12.1.2 Technique Applicability: ★★★

XCT is capable of imaging the porosity and delaminations in this specimen.

E.12.1.3 Laboratory Setup

The microfocus XCT system at NASA LaRC is a commercially available Avonix (Nikon C2) Metrology System designed for high-resolution NDE inspections. The system is an advanced microfocus X-ray system, capable of resolving details down to 5 μm, and with magnifications up to 60X. Supplied as complete, the system is a large-dimension radiation enclosure with X-ray source, specimen manipulator, and an amorphous silica detector, as shown in Figure E.12-2. The imaging controls are housed in a separate control console. The detector, visible behind the specimen in Figure E.2-4b, is a Perkin-Elmer, 16-bit, amorphous-silicon digital detector with a 2000 × 2000-pixel array.

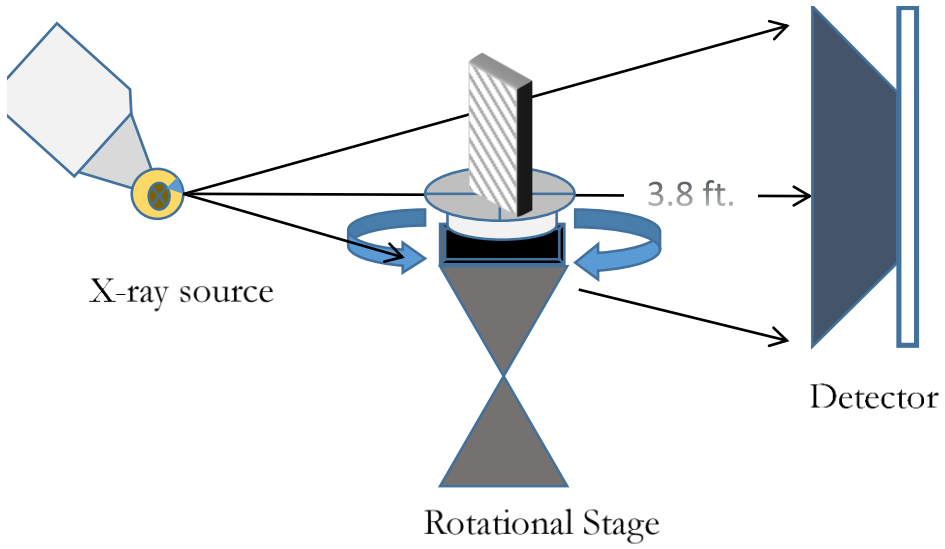

Figure E.12-2. XCT system components.

A consistent Cartesian coordinate system is used to define slice direction as illustrated in Figure E.12-3. Slices normal to the X-, Y-, and Z-directions are shown in Figure E.12-3a, b, and c, respectively.

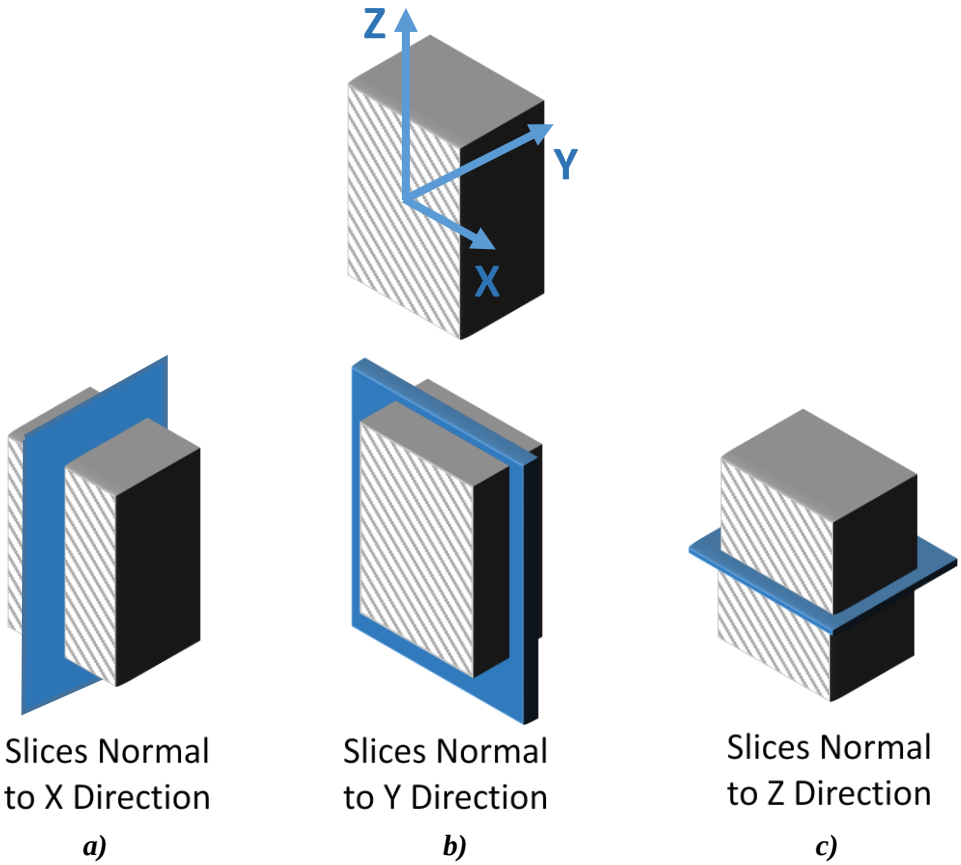

Figure E.12-3. Slice direction nomenclature.

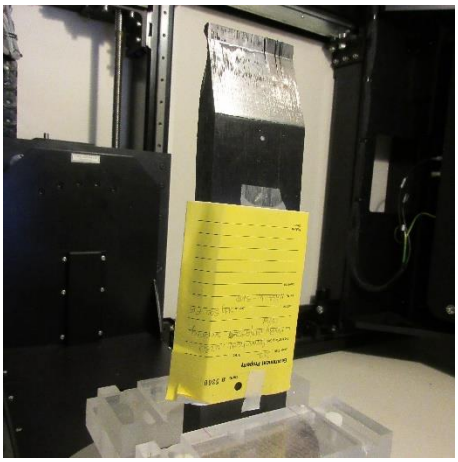

Figure E.12-4. Specimen orientation within the system.

E.12.1.4 Equipment List and Specifications:

- Avonix 225 CT System
- 225 kV microfocus X-ray source with 5 µm focal spot size
- 15 or 30 kg Capacity, 5-axis, fully programmable manipulator
- Detector: Perkin Elmer XRD 1621 – 2000 × 2000 pixels with 200 µm pitch
- 10 µm spatial resolution for specimens 1.5 cm wide

- Thin panels 10 × 10 inches – full volume 200 μm spatial resolution

E.12.1.5 Settings

Table E.12-1. Data collection settings.

Source Energy	150 kV
Current	50 μA
Magnification	1.65 X
Filter	NF
# Rotational angles	3142
Exposure time / frame	1.0 sec.
Max Histogram Grey Level	30 K
# Averages	8
Resolution (μm)	120.947 μm
Array Dimensions (pixels)	Set 1: 1999 × 362 × 1998 Set 2: 1998 × 686 × 1997

The specimen is placed vertically (rotated about the smallest dimension) on the rotational stage located between the radiation source and the detector. The rotational stage is computer controlled and correlated to the position of the sample. As the sample is rotated the full 360° (~0.11° increments), the detector collects radiographs at each rotated angle as the X-ray path intersects the sample. 3D reconstruction of the collection of radiographs produces a volume of data that can then be viewed along any plane in the volume. The closer the sample can be placed to the X-ray source, the higher the spatial resolution that can be obtained.

E.12.1.6 Inspection Results

Section A

Specimen #12, NASA-W-20MP, is a wedge panel fabricated from IM7/8552, with an objective of achieving medium porosity and delaminations. XCT was performed on this specimen in NASA LaRC's CT system with the settings defined in Section E.12.1.5. Countless instances porosity as well as disbonds are easily viewed in the CT slices corresponding to the different viewing directions, as highlighted in the figures below.

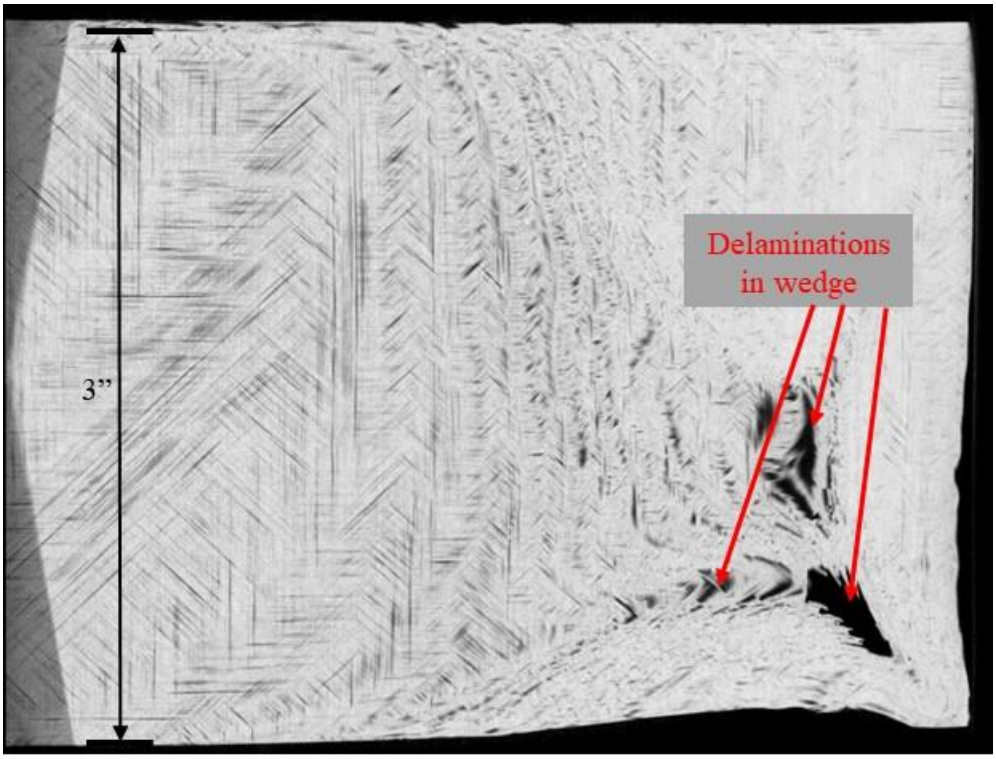

Figure E.12-5. CT slices from the y-direction showing porosity and delaminations within the sample.

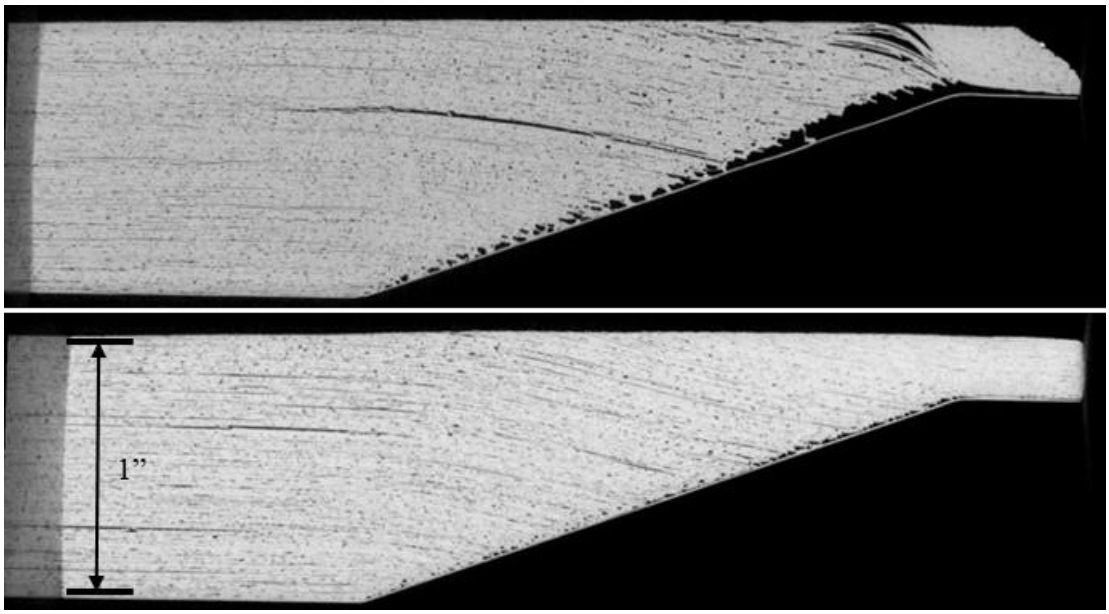

Figure E.12-6. XCT slices from the z-direction showing close views of porosity and delaminations within the sample.

From the analysis, large delaminations can be seen as well as gross porosity throughout the entire specimen. The darker regions represent the air gaps as the bulk material is much denser. The porosity and disbonds are detected at all depths in the specimen as shown in Figure E.12-5 and E.12-6. In Figure E.12-7 it can be seen that much of the delaminations in the sample occurred along the wedged portion of the sample.

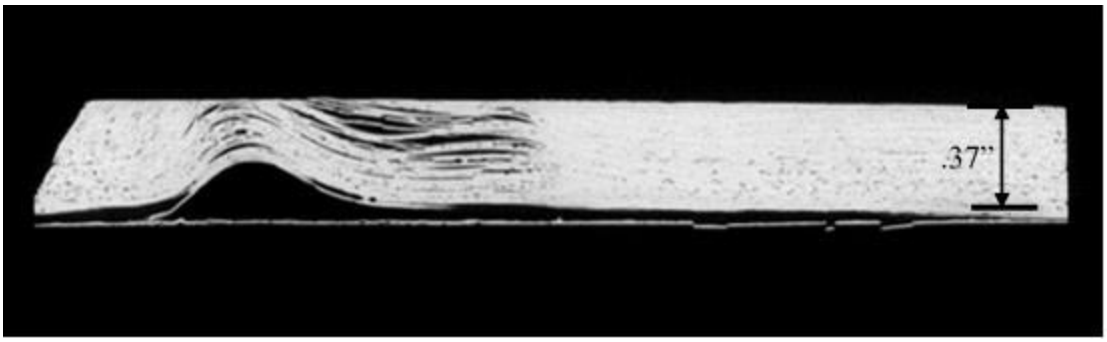

Figure E.12-7. XCT slices from the z-direction showing close views of porosity and delaminations within the sample.

Section B

Semantic CT Image Segmentation Technique:

The developed semantic CT image segmentation technique, originally designed at NASA LaRC, applies a CNN to identify and segment cracks and delamination in carbon fiber due to impact. The segmentation is done on the specimens' CT scan grayscale images. This method was first developed by D.T. Delelegn [1] as his master's thesis, and then improved as a NASA white paper.

There are two implemented CNN models each identifying the two damage types, i.e. crack and delamination, separately. The first model easily identifies delamination whereas the second is optimized to detect cracks and 'linear-type' damage. Each model prediction outputs are floating numbers between [0,1] indicating how likely an area is damaged. Class label one ("1") representing a highest damage prediction certainty while zero ("0") for a no-damage area. This probabilistic prediction value of an area damage indication is used to seek the most damaged area in the material.

The prediction is done on the CT images with a 4 × 4 window (patch) size. Then, the predicted class labels for each patch from the two models are combined as the Red (crack) and the Green (delamination) channels of the RGB color model representing the two damage types in different colors. For further reading, refer D.T. Delelegn [1].

This segmentation technique is able to easily point out cracks or linear damage that are collocated with a delamination. This is because that the prediction of the two models are represented in the different channels of the RGB color model.

While originally developed to detect impact damage, the method was applied to ACP Handbook standards (porosity, delamination, AFP defects, etc.) with varying degrees of success. Here, the method is applied to handbook specimen #12, which is a 12 × 3 × 1-inch wedge configuration with medium porosity, which is easily identified in the delaminations shown in Figures E.12-8 and E.12-9.

Segmentation Output:

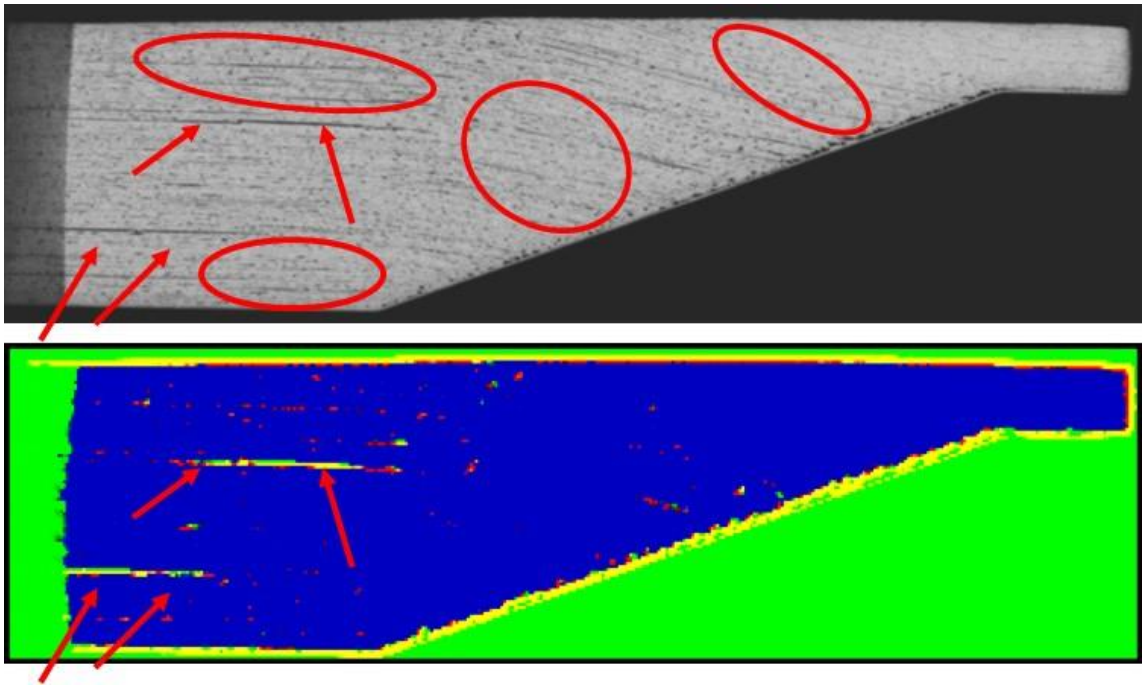

Figure E.12-8. (Top) XCT slice from the z-normal direction showing porosity and delaminations within the sample. (Bottom) Segmentation of the same slice.
Segmentation detected the larger regions of porosity that formed delaminations (red arrows), but not the smaller regions clearly visible to the SME (red ovals).

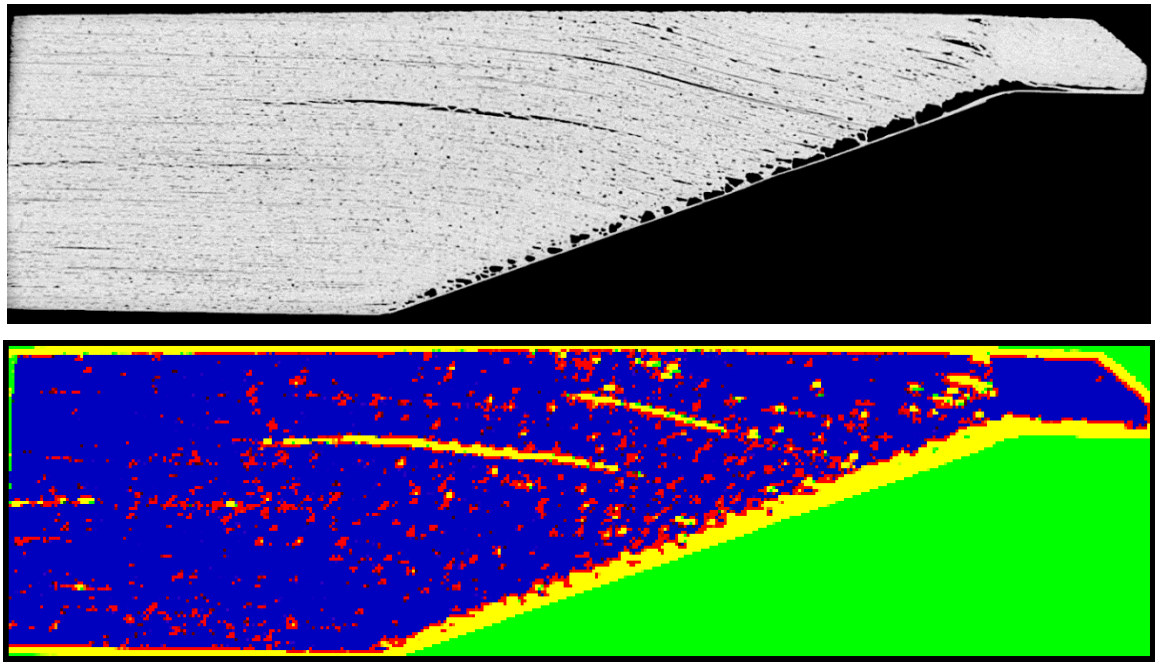

Figure E.12-9. (Top) XCT slices from the z-normal direction showing close views of porosity and delaminations within the sample. (Bottom) segmentation of a specimen from XCT slices from the z-normal direction showing the CT slice with both delaminations and porosity within the sample. Segmentation of this XCT slice detected porosity comparable to SME findings.

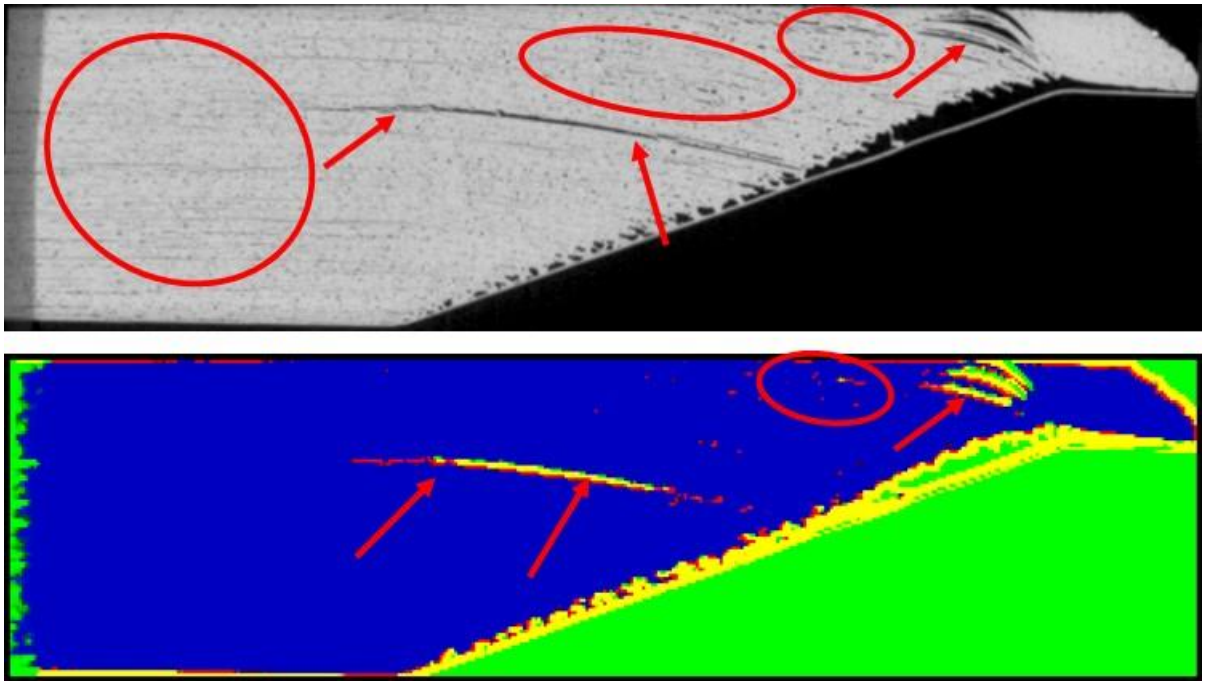

Figure E.12-10. (Top) XCT slices from the z-normal direction showing porosity and delaminations within the sample. (Bottom) segmentation results of the slice. Segmentation detected the larger regions of porosity that formed delaminations (red arrows), but not the smaller regions of porosity clearly visible to the SME (red ovals).

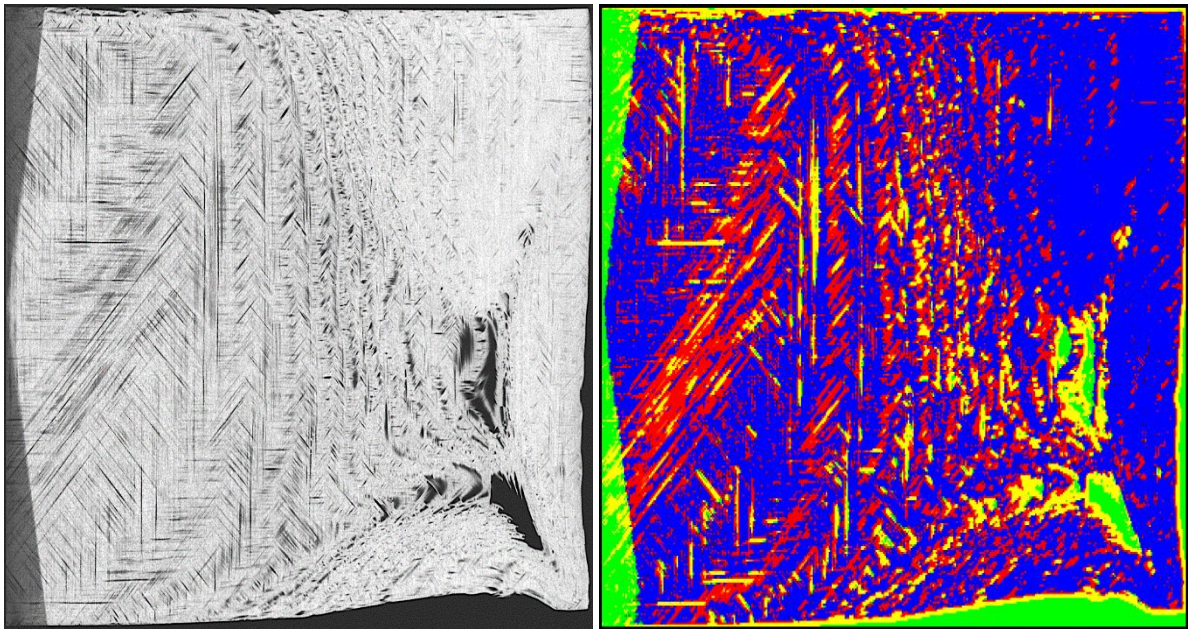

Figure E.12-11. (Left) CT slices from the y-normal direction showing porosity and delaminations within the sample. (Right) CNN segmentation results showing porosity and delaminations.

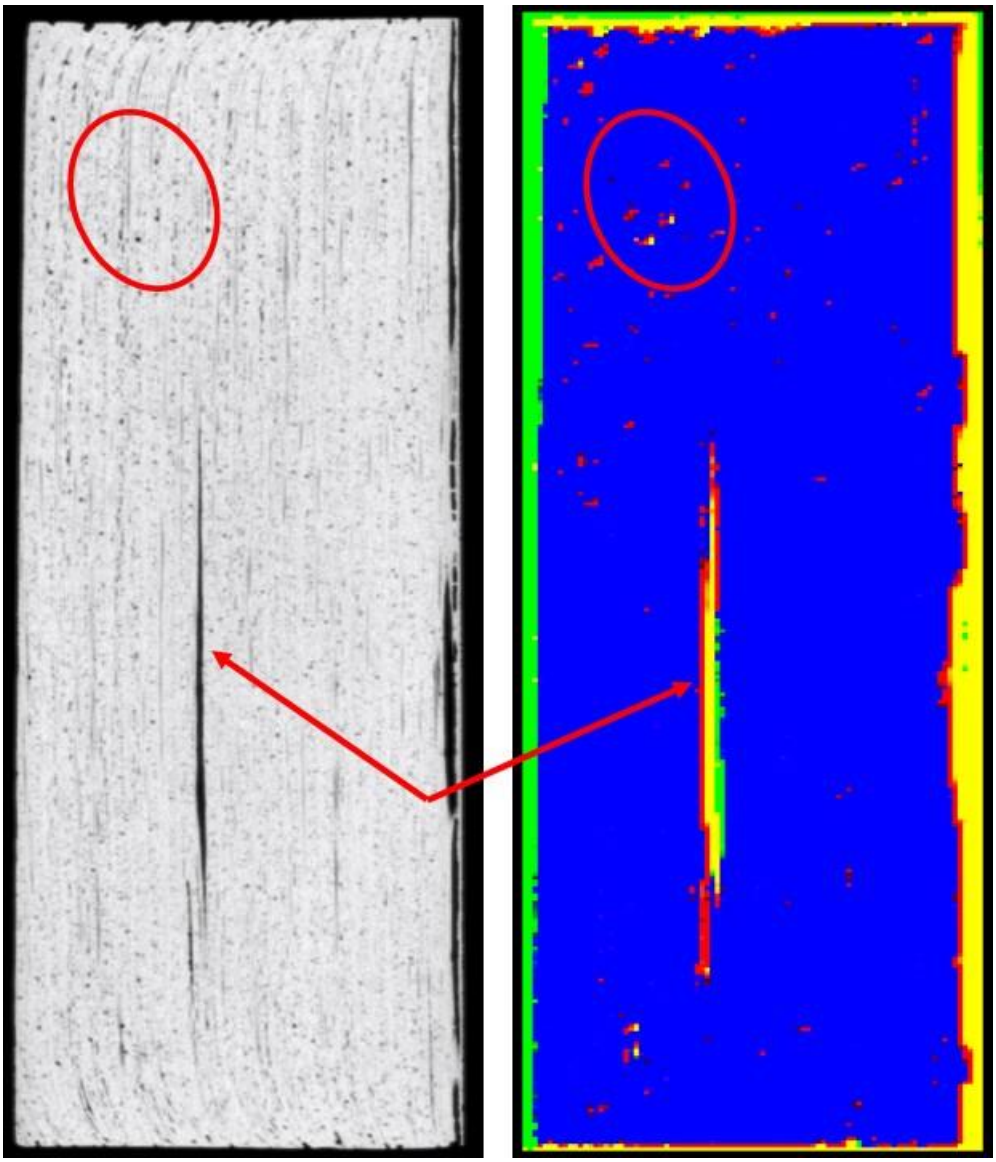

Figure E.12-12. (Left) CT slices from the x-normal direction showing porosity and delaminations within the sample. (Right) CNN segmentation results showing porosity and delaminations. While segmenation detected the large delamination (red arrows) and larger diameter porosity (red ovals), it did not detect the smaller, fine distributed porosity visible to the SME.

E.12.1.7 References

[1] Delelegn, Desalegn Temesgen, "Non-destructive Evaluation for Composite Material," Master of Science Thesis, Old Dominion University, August 2018

E.13 Specimen #13: NASA-W-IL-20MP

Structure	Material	Details	Dimensions (inches)	Partner Methods	
Uni-ply (0/90/45)	IM7/8552	Wedge Interleaved 20° with medium porosity	12 × 3 × 1.5	NASA	E.13.1 XCT

Figure E.13-1. Photographs of Specimen #12: NASA-W-IL-20MP.

E.13.1 *Method: X-ray Computed Tomography (XCT)*

E.13.1.1 Partner: NASA

E.13.1.2 Technique Applicability: ★★★

XCT is capable of imaging the porosity and delaminations in this specimen.

E.13.1.3 Laboratory Setup

The microfocus XCT system at NASA LaRC is a commercially available Avonix (Nikon C2) Metrology System designed for high-resolution NDE inspections. The system is an advanced microfocus X-ray system, capable of resolving details down to 5 μm, and with magnifications up to 60X. Supplied as complete, the system is a large-dimension radiation enclosure with X-ray source, specimen manipulator, and an amorphous silica detector, as shown in Figure E.13-2. The imaging controls are housed in a separate control console. The detector, visible behind the specimen in Figure E.2-4b, is a Perkin-Elmer, 16-bit, amorphous-silicon digital detector with a 2000 × 2000-pixel array.

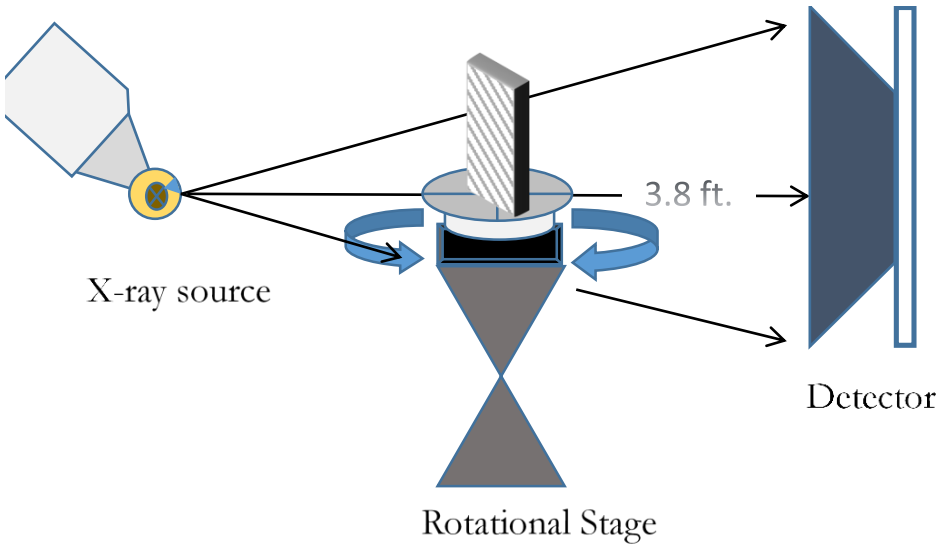

Figure E.13-2. XCT system components.

A consistent Cartesian coordinate system is used to define slice direction as illustrated in Figure E.13-3. Slices normal to the X-, Y- and Z-directions are shown in Figure E13-3a, b, and c, respectively.

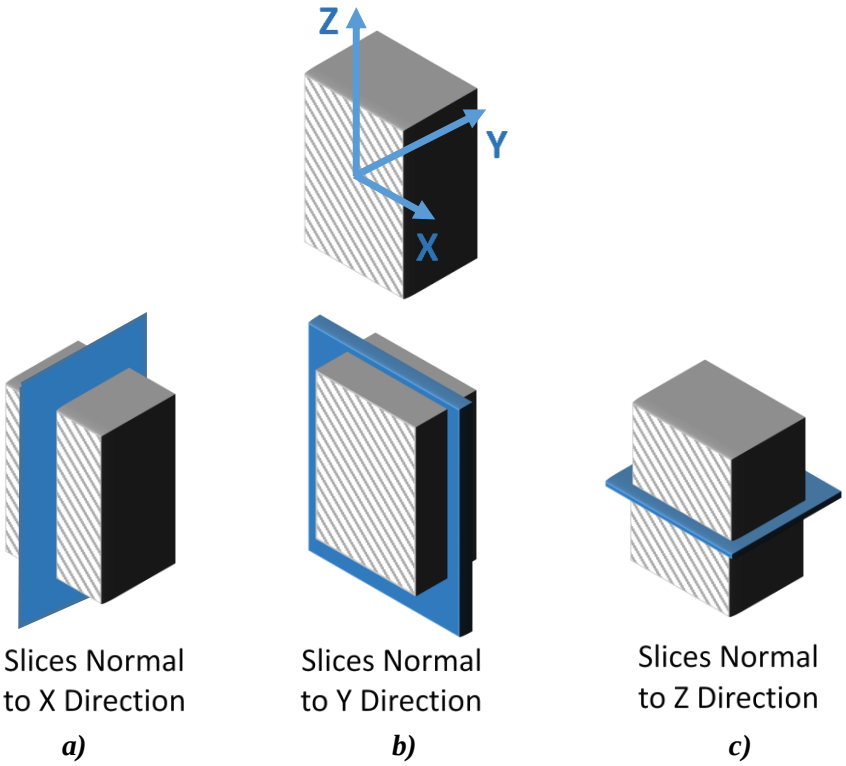

Figure E.13-3. Slice direction nomenclature.

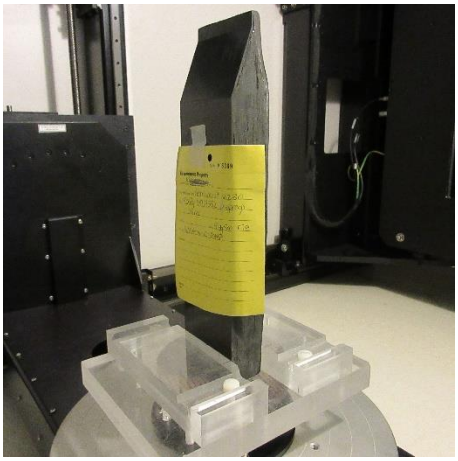

Figure E.13-4. Specimen orientation within apparatus.

E.13.1.4 Equipment List and Specifications:

- Avonix 225 CT System
- 225 kV microfocus X-ray source with 5 µm focal spot size
- 15 or 30 kg Capacity, 5-axis, fully programmable manipulator
- Detector: Perkin Elmer XRD 1621 – 2000 × 2000 pixels with 200 µm pitch
- 10 µm spatial resolution for specimens 1.5 cm wide
- Thin panels 10 × 10 inches – full volume 200 µm spatial resolution

E.13.1.5 Settings

Table E-13-2. Data collection settings.

Source Energy	150 kV
Current	50 µA
Magnification	1.65 X
Filter	NF
# Rotational angles	3142
Exposure time / frame	1.0 sec.
Max Histogram Grey Level	30 K
# Averages	8
Resolution (µm)	120.947 µm
Array Dimensions (pixels)	Set 1: 1999 × 362 × 1998 Set 2: 1998 × 686 × 1997

The specimen is placed vertically (rotated about the smallest dimension) on the rotational stage located between the radiation source and the detector. The rotational stage is computer controlled and correlated to the position of the sample. As the sample is rotated the full 360° (~0.11° increments), the detector collects radiographs at each rotated angle as the X-ray path intersects the sample. 3D reconstruction of the collection of radiographs produces a volume of data that can then be viewed along any plane in the volume. The closer the sample can be placed to the X-ray source, the higher the spatial resolution that can be obtained.

E.13.1.6 Inspection Results

Specimen #13, NASA-W-IL-20MP, is a wedge panel fabricated from IM7/8552, with an objective of achieving medium porosity and delaminations. XCT was performed on this specimen in NASA LaRC's CT system with the settings defined in Section E.13.1.5. Countless instances porosity as well as disbonds are easily viewed in the CT slices corresponding to the different viewing directions, as highlighted in the figures below.

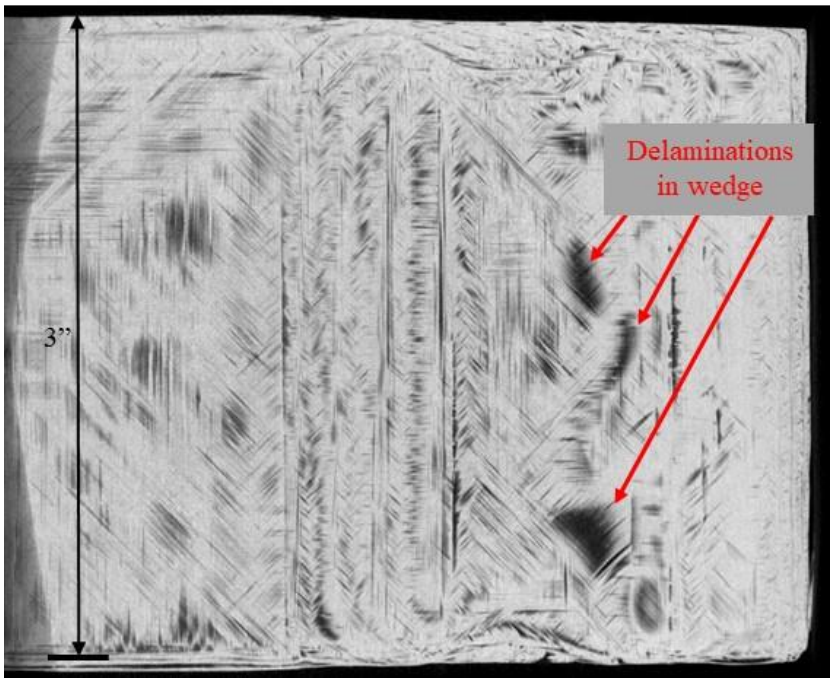

Figure E.13-5. CT slices from the y-direction showing porosity and delaminations within the sample.

From the analysis, large delaminations can be seen as well as gross porosity throughout the entire specimen. The darker regions represent the air gaps as the bulk material is much denser. The porosity and disbonds are detected at all depths in the specimen as shown in Figures E.13-6 and E.13-7. In Figure E.13-6, it can be seen that much of the larger delaminations in the sample occur along the wedged portion of the sample.

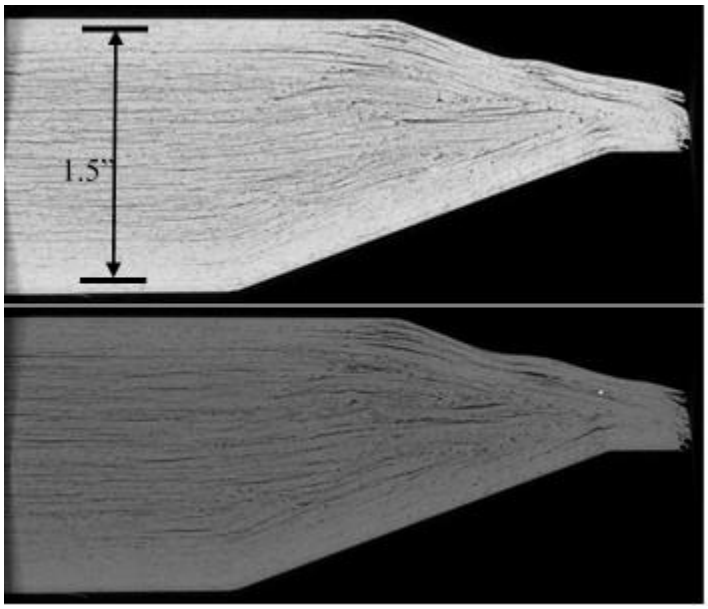

Figure E.13-6. XCT slices from the z-direction showing porosity and delaminations within the sample.

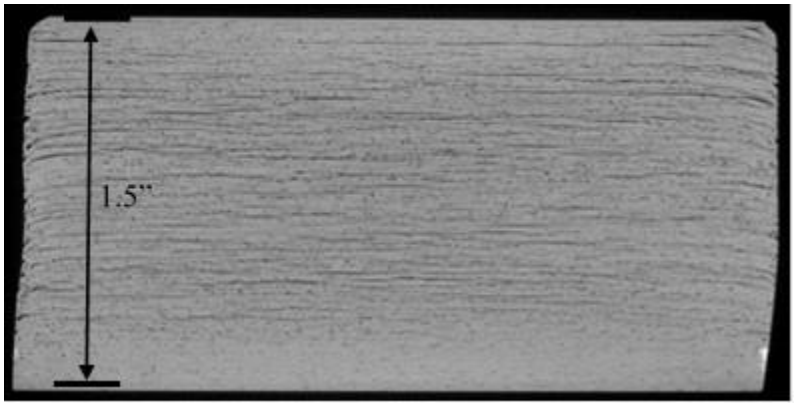

Figure E.13-7. XCT slices from the z-direction showing porosity and delaminations within the sample.

E.14 Specimen #14 – Not manufactured

E.15 Specimen #15 – Not manufactured

E.16 Specimen #16: NASA-RP-01D

Structure	Material	Details	Dimensions (inches)	Partner Methods	
Uni-ply (0/90/45)	IM7/8552	Radius Panel 0.1 inch Curve Rad with defects	4.5 × 2.5 × 4	USC	E.16.1 GWUT

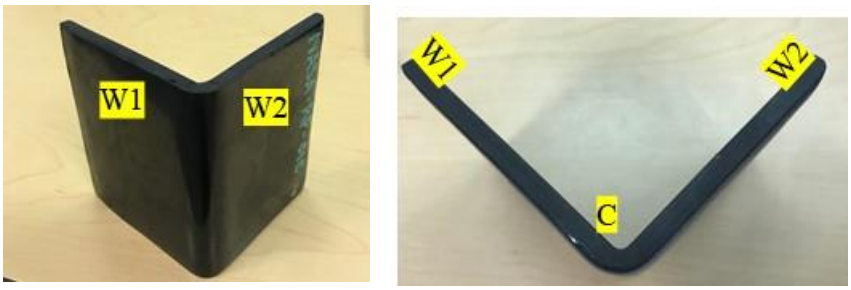

a) *b)*

Figure E.16-1. Photographs of Specimen NASA-RP-01D. (a) overall view, and (b) side view.

E.16.1 *Method: Guided Wave Ultrasound (GWUT)*

E.16.1.1 Partner: USC

E.16.1.2 Technique Applicability: ★★★

GWUT employs ultrasonic waves that propagate along waveguides by its boundaries, e.g. pipes, rods and plate-like structures, which allows waves propagate a long distance with little energy loss. GWUT shows advantage in many types of defect inspection, e.g. crack in metallic structures [1], and delamination in composite structures [2].

The specimen, NASA-RP-01D (herein referred to as 01D), is tested using hybrid piezoelectric transducers (PZT)-scanning laser Doppler vibrometer (SLDV) GWUT method in this report. General information of 01D is illustrated in the following paragraph. The relative inspection, results and system rating are illustrated in the inspection results.

Specimen 01D is shown in Figure E.16-1 with two wing parts (W1 and W2) and the connecting curve part (C). The height of the specimen is 101 mm, and the thickness is around 7 mm. The width of W1 is 75 mm (straight part without any curvature), and the width of W2 is 70 mm. No other information about 01D is available to the inspectors.

E.16.1.3 Laboratory Set Up

The same hybrid PZT-SLDV system is employed for 01D inspection, where contact type PZT is used as actuator and SLDV as sensor to excite and receive guided waves in the testing plate (Lamb waves) [1]. The overall setup, shown in Figure E.16-2 and Figure E.16-3 also remains the same as reported previously [3].

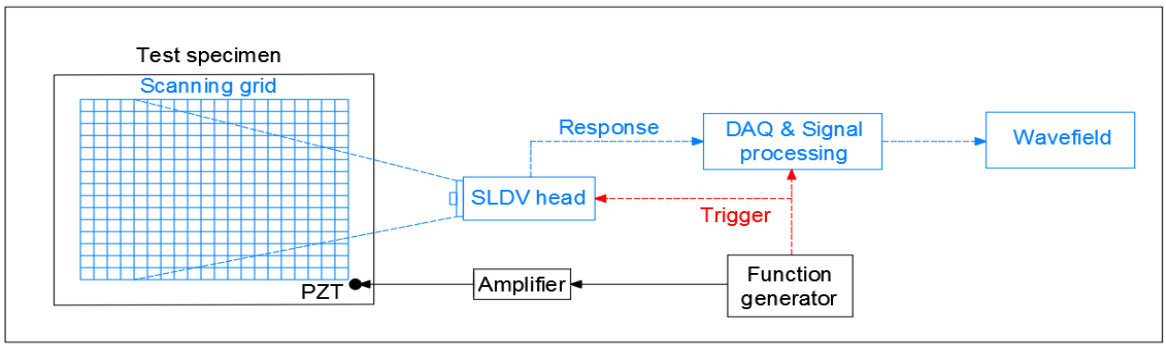

Figure E.16.-2. Schematic design of the PZT-SLDV system.

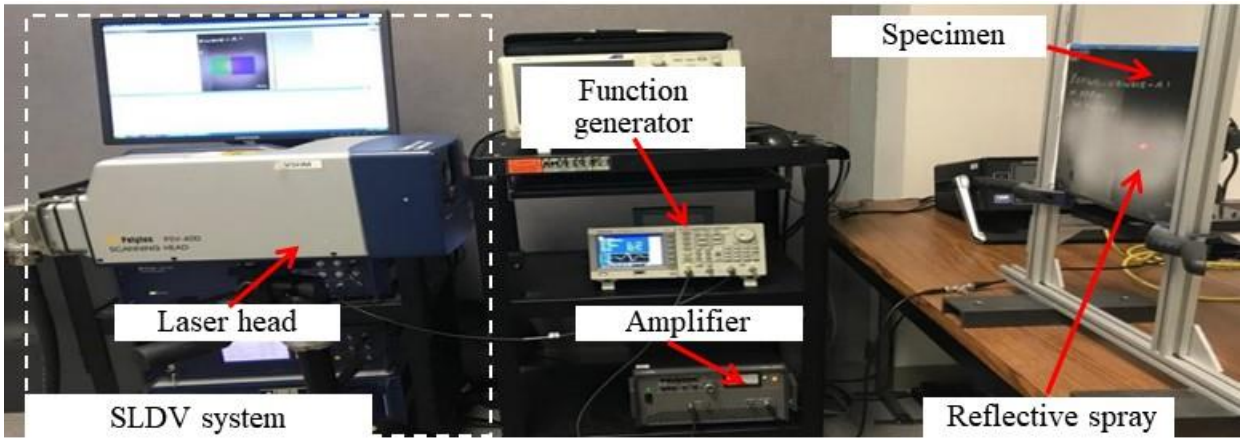

Figure E.16-3. Experimental setup of the PZT-SLDV system.

E.16.1.4 Equipment List and Specifications

The detailed specifications of the equipment and devices used for the hybrid PZT-SLDV system at USC Visualized Structural Health Monitoring (VSHM) laboratory are given in Table E.16-1. Data acquisition settings are shown in Table E.16-2.

Table E.16-1. Equipment/device specifications.

Equipment/device	Specifications
Polytec PSV-400-M2	2D scanning laser Doppler vibrometer with a frequency range up to 1 MHz with specific velocity decoders
PZT	Steminc 7-mm circular 0.5-mm thick piezoelectric transducers
Tektronix AFG3022C	2-channel arbitrary function generator with 1μHz to 25MHz
HSA 4014	High speed bipolar amplifier up to 1 MHz and 200 VA
Target Simply Balanced™ organic honey	Natural and organic honey blend performed as couplant
Albedo 100 Reflective Spray	a non-permanent, clear spray with light-reflective properties

E.16.1.5 Settings

Table E.16-2. Data collection settings.

Sampling frequency (MHz)	12.56 MHz
Spatial sampling interval (mm)	1 mm
Average	100
Velocity decoder	VD-07 10mm/s/V
Spray coating	20 layers

The inspection is divided into three parts based on the predefined area as W1, W2 and C. A 3-count toneburst at 150 kHz amplified to 50 V_{pp} is used as excitation for each test. 2D area scan is performed for each part with spatial resolution 1 mm.

Since W1 and W2 are the plate-like part without any curvatures, they are first inspected with the SLDV normal to the specimen surface. The coordinates of W1 and W2 are defined as shown in Figure E.16-4 (unit: mm). In order to have an overview of each wing, the excitation point is selected at around the middle of each wing. The excitation is at (40, 50) of W1 coordinate system, while at (30, 50) for W2. 2D area inspection is performed at each wing (W1 and W2) on both sides. For each inspection, the scanning area covers the accessible surface of the inspected wing:

around 75 mm × 100 mm for W1 and 70 mm × 100 mm for W2. For each side, the inspection area differs a little due to the curvature.

Due to the curvature of part C, the inspection is performed by placing the SLDV head as illustrated in Figure E.16-4b. The scanning area is 10 mm × 100 mm for both sides of each wing. Note that the scanning grid is the projection of the C part. The angle error is not considered in this inspection by SLDV.

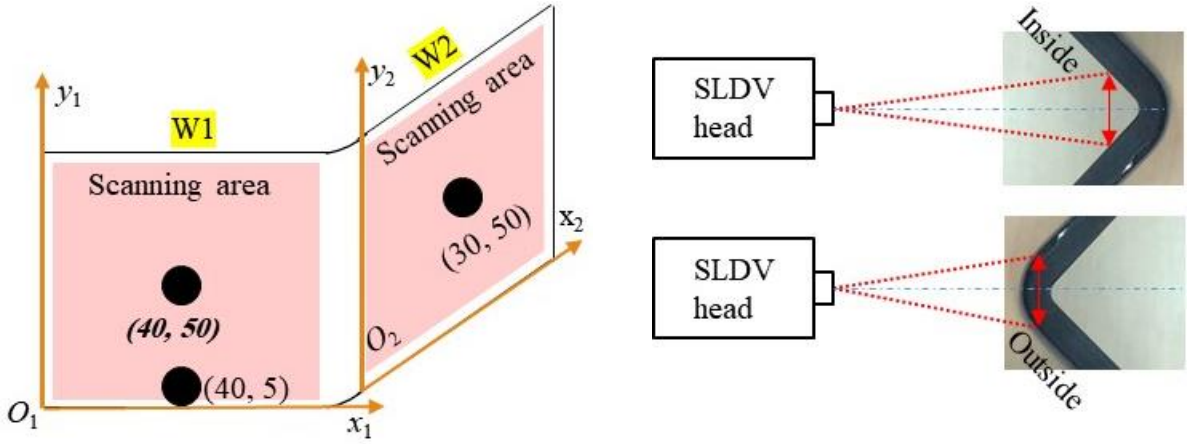

a) *b)*

Figure E.16-4. Experimental setup (a) scanning schematic design of W1 and W2, and (b) 2D area inspection.

E.16.1.6 Inspection Results

W1 (wing-1)

2D area inspection is performed at both sides of W1. The 2D time-space wavefields are obtained. The wavefield at 24 and 35 µs are plotted in Figure E.16-5a and Figure E.16-5b. In both wavefields, a stripe shape defect is clearly observed. In addition, two other defects interaction with waves are observed at $y_1 \approx 50$ mm, defined as Group-2. To visualize the defect more clearly, the energy map is plotted in Figure E.16-6a. As shown in Figure E.16-6a, a stripe shape defect with height around 6 mm is detected at pointed by a blue arrow. The defect starts at $x_1 \approx 71$ mm and exists until the end of the curve part C. This defect is defined as Group-1.

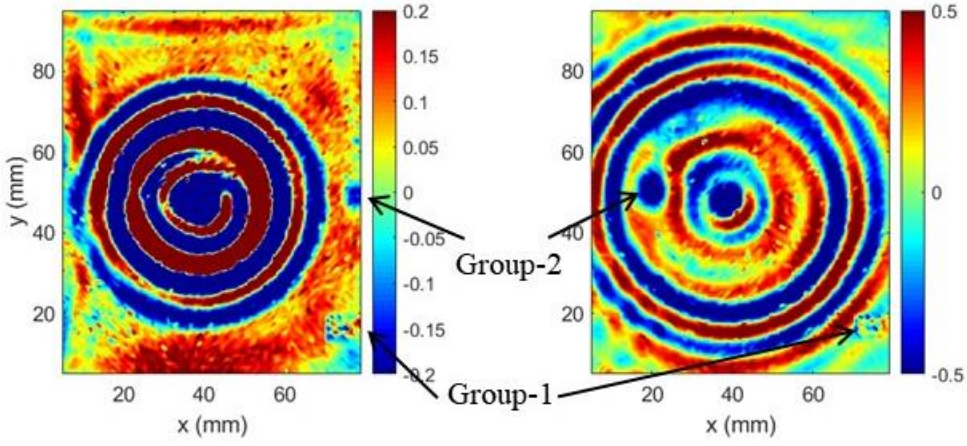

a) *b)*

Figure E.16-5. W1 wavefield on Outside at: (a) 24 µs, and (b) 35 µs.

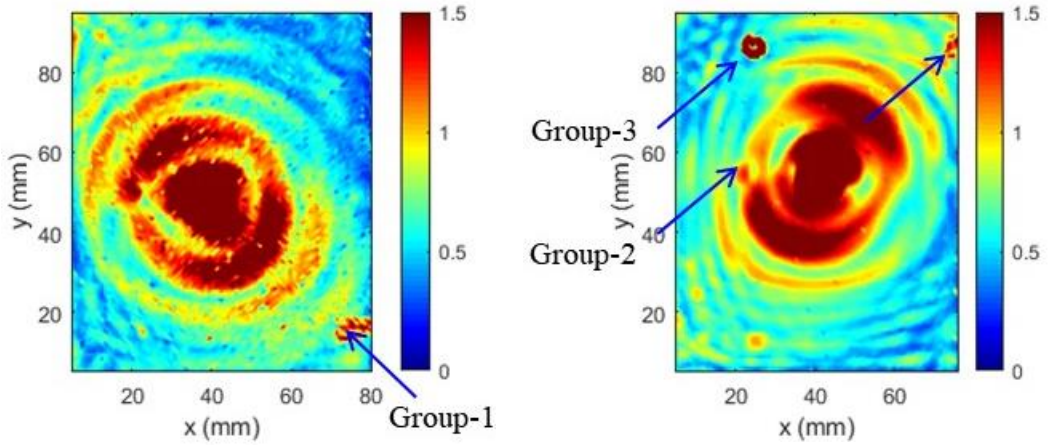

Figure E.16-6. Energy maps of W1 on: (a) outside, and (b) inside.

The energy map obtained from the wavefield on inside is plotted in Figure E.16-6b. In the energy map, a circular shape defect with diameter 6 mm is detected at around (24.5, 86) in W1 coordinate system. At the same height of the circular defect, another stripe-like defect with height 6 mm is detected at $x_1 \approx 72$ mm and exists until the end of the curve part C. These two defects are defined as Group-3. The inspection results show that the defect Group-1 is close to outside, while the Group-2 defect is close to inside.

Since Group-2 defects observed in the wavefields are not detected in the energy map. Another scan is performed on inside with actuation at (40, 5), where the excitation is located at the bottom edge of W1. The wavefield at 28 μs is plotted in Figure E.16-7a, where the Group-2 defect interaction with waves are clearly observed. The energy map generated within time range 20–30 μs where the wave interaction with Group-2 defect strongest is plotted in Figure E.16-7b.

From the inspection, it is concluded that Group-2 defects might located around the middle layer of the composites since they are not clearly observed from either side.

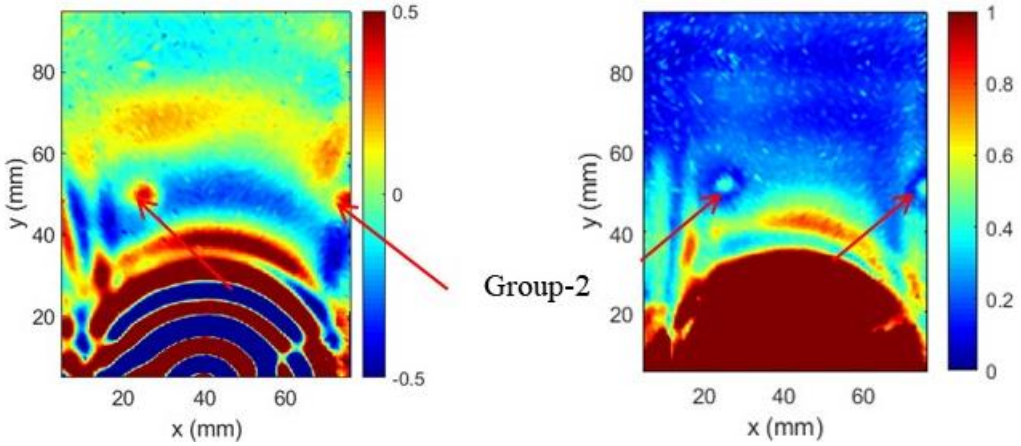

Figure E.16-1. Inspection at bottom edge of W1: (a) wavefield at 28 μs, and (b) energy map within time range 20–30 μs.

W2 (wing-2)

The same 2D area inspection is performed at both sides of W2. The relative energy maps on outside and inside are plotted in Figure E.16-8a. A small stripe shape defect with height around 6 mm is detected at pointed by a blue arrow. The defect starts at $x_2 \approx$ -3 mm and exists until the end of the curve part C. This defect matches the Group-1 defect on W1.

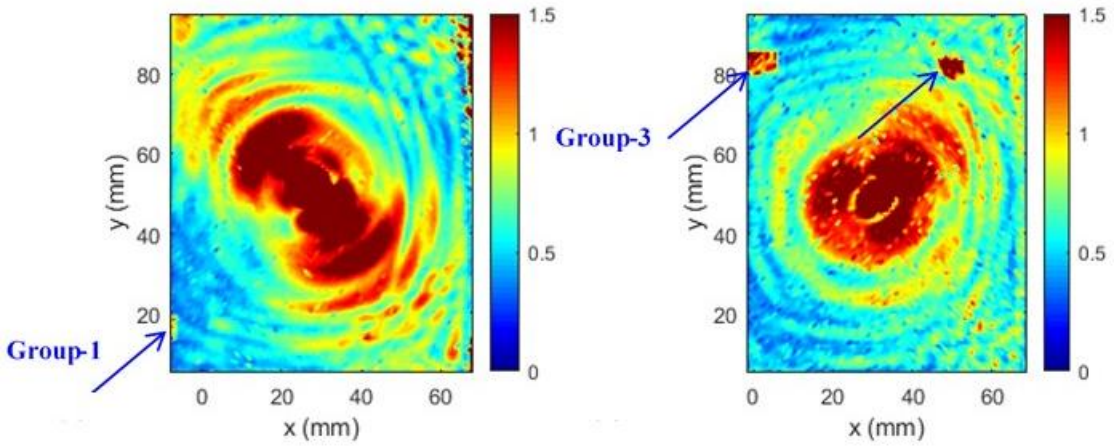

a) *b)*

Figure E.16-8. Energy maps of W2 on: (a) outside, and (b) inside.

The energy map obtained from the wavefield on inside is plotted in Figure E.16-8b. In the energy map, a half-circular shape defect with diameter 6 mm is detected at around (46.5, 86) in W2 coordinate system. At the same height of the circular defect, another stripe-like defect with height 6 mm is detected at $x_2 \approx$ 8 mm and exists until the end of the curve part C. These two defects match the height of Group-3 on W1. In addition, the stripe defect is clearly identified at the curve area. The inspection results also show that the defect Group-1 is close to outside, while the Group-3 defect is close to the inside.

The energy map generated from the wavefield on inside within time range 15–30 μs is plotted in Figure E.16-9. From the inspection result, Group-2 defect observed might be located around the middle layer of the composites since they are not clearly observed from either side.

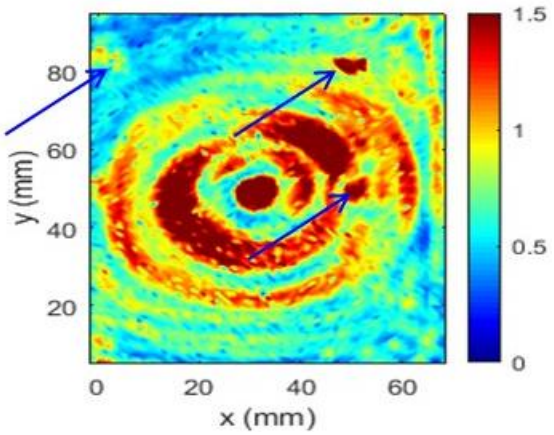

Figure E.16-9. Energy maps of W2 on inside.

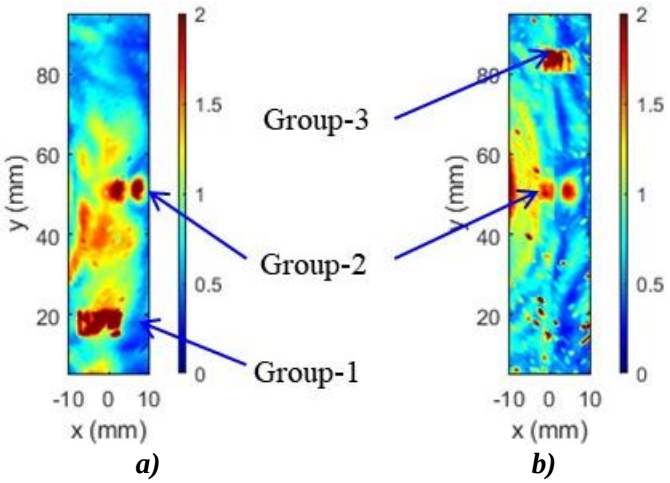

Figure E.16-10. Energy maps of C Part on: (a) outside, and (b) inside.

C part (curve part)

As shown in Figure E.16-4b, 2D area inspection is performed at both sides of the curve part. The relative energy maps on outside and inside are plotted in Figure E.16-10. The stripe shape defect is clearly observed at the curve part at y = 16, 50, and 84 mm. Group-1 stripe defect is clearly observed at outside inspection while Group-3 strip is clearly identified at inside inspection. This confirmed that Group-1 defect is close to outside surface while Group-3 defect is close to inside surface. In addition, the Group-2 defect is only detected while its shape is not identified due to its location is close to the middle layer of the plate.

With the inspection results from the above sections, the detection summary of the defect is illustrated in Figure E.16-11. Severn defects are identified which are defined as Group-1, Group-2, and Group-3. Group-1 is located at close to the surface of outside while Group-3 is close to the surface of inside. Group-2 is located close to the middle layer of the specimen.

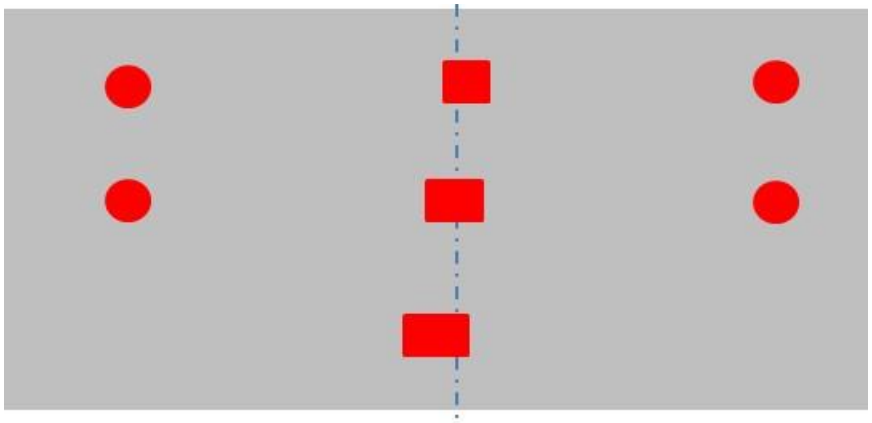

Figure E.16-11. Inspection summary of identified defects.

In conclusion, delamination on 01D specimen using the hybrid PZT-SLDV system is successful detected and quantified even without material properties. The detailed rating of the system is shown in Table E.16-3. The defects are successfully detected so that five stars are rated for this part. For defect visualization, some defect shapes are clearly identified while some are not, four

out of five stars is rated. For inspection time, the inspection time for one 2D scanning is around 30 minutes for areas illustrated in this test, which is fast. Thus, the inspection time gets four stars overall. Last, the actuator PZT is $3.60 per piece, which is cost effective. However, the SLDV is an expensive equipment, which costs $300,000 when purchasing. Thus, this part gets two stars. In the future, expensive SLDV can be replaced by customized fixed LDV and gantry system to reduce the system cost. Overall, this hybrid PZT-SLDV guided wave inspection is very robust in general with four out of five stars.

Table E.16-1. Hybrid PZT-SLDV guided wave inspection rating.

Hybrid PZT-SLDV guided wave inspection		
NASA-RP-01D Defect: delaminations	Rating	
	Detection:	★★★★★
	Defect visualization	★★★★☆
	Inspection time:	★★★★☆
	Equipment cost:	★★☆☆☆
	Overall Performance:	★★★★☆

E.16.1.7 References

[1] Yu, L.; Leckey, C. A. & Tian, Z. (2013). "Study on crack scattering in aluminum plates with Lamb wave frequency–wavenumber analysis", Smart Materials and Structures, Vol. 22, No. 6, pp065019, 2013.

[2] Tian, Z., Yu, L., & Leckey, C. (2015). "Delamination detection and quantification on laminated composite structures with Lamb waves and wavenumber analysis", Journal of Intelligent Material Systems and Structures, Vol.26, No. 13, 2015, pp. 1723-1738.

[3] Guided wave inspection on specimen A1 (A1 report, submitted)

E.17 Specimen – Not Manufactured

E.18 Specimen #18: NASA-RP-10D

Structure	Material	Details	Dimensions (inches)	Partner Methods	
Uni-ply (0/90/45)	IM7/8552	Radius Panel 1.0 inch Curve Rad with defects	4.5 × 2.5 × 4	USC	E.18.1 GWUT

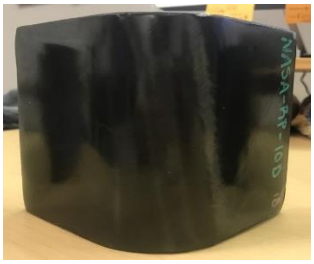

a)

b)

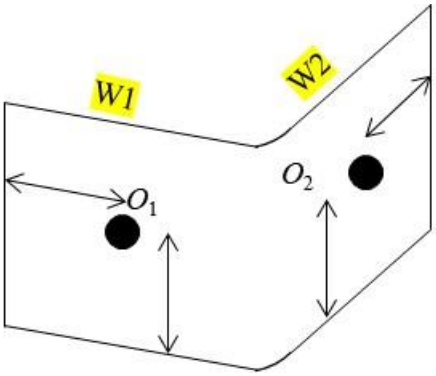

c)

Figure E.18-1. Photographs of Specimen NASA-RP-10D. (a) overall view, (b) side view, and (c) specimen setup.

E.18.1 *Method: Guided Wave Ultrasound (GWUT)*

E.18.1.1 Partner: USC

E.18.1.2 Technique Applicability: ★★★

GWUT employs ultrasonic waves that propagate along waveguides by its boundaries, e.g. pipes, rods and plate-like structures, which allows waves propagate a long distance with little energy loss. GWUT shows advantage in many types of defect inspection, e.g. crack in metallic structures [1], and delamination in composite structures [2].

The specimen, NASA-RP-10D (herein referred to as 10D), is inspected using hybrid PZT-SLDV GWUT method in this report. General information of 10D is illustrated in Section 2. The relative inspection, results and system rating are illustrated in inspection results.

The front view and side view of Specimen 10D are shown in Figure E.18-1a and Figure E.18-1b, respectively. The height of the specimen is 101 mm, and the thickness is around 7.28 mm. The length between the specimen edges is 110 mm (predefined W1 and W2 with arc length 53 mm) as shown in Figure E.18-1c. The actuator is attached at O_1 and O_2 in order to inspect the specimen from different views. No other information about 10D is available to the inspectors.

E.18.1.3 Laboratory Set up

The same hybrid PZT-SLDV system is employed for 10D inspection, where contact type PZT is used as actuator and SLDV as sensor to excite and receive guided waves in the testing plate (Lamb waves) [1]. The overall setup also remains the same as previously reported and shown in Figure E.18-2 and Figure E.18-3 [3].

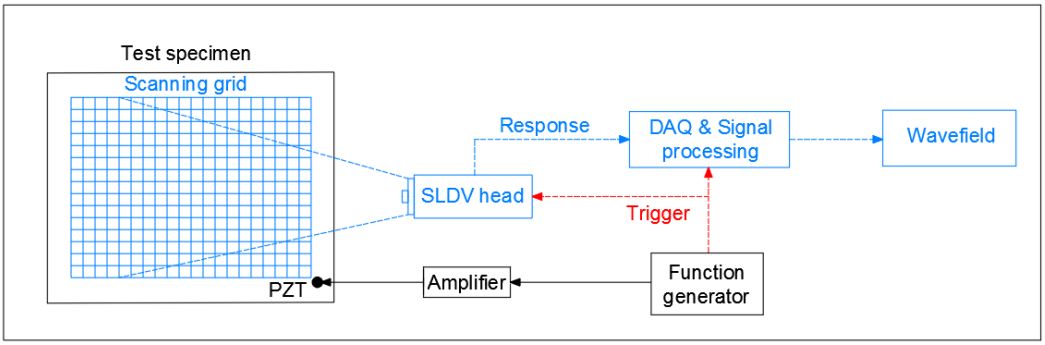

Figure E.18-2. Schematic design of the PZT-SLDV system.

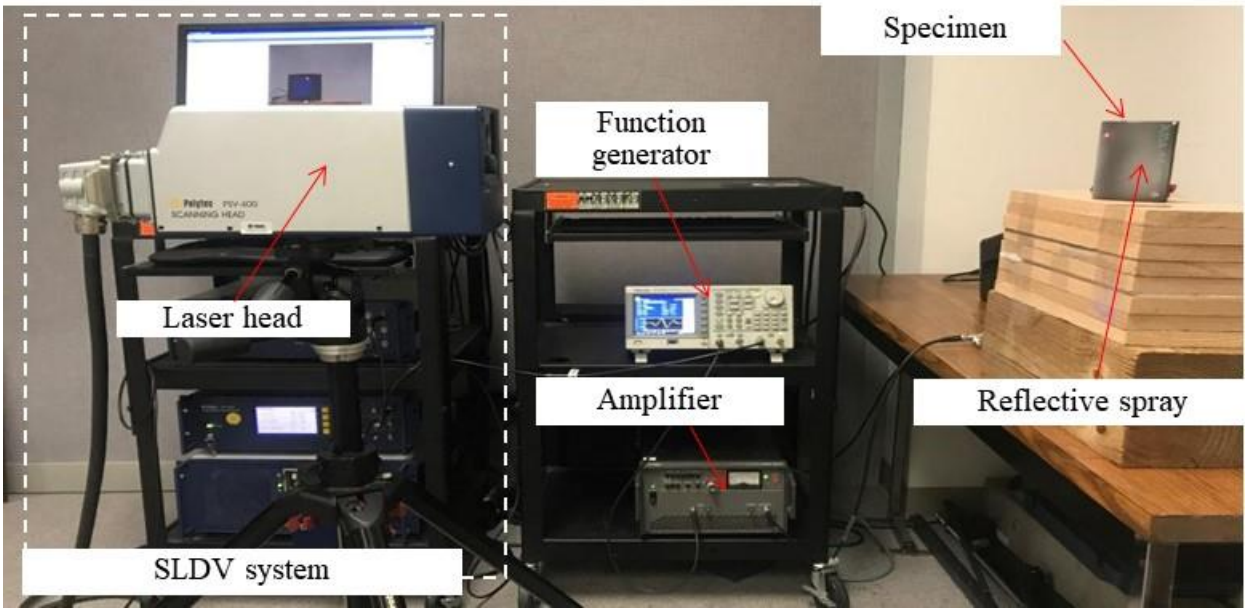

Figure E.18-3. Experimental setup of the PZT-SLDV system.

E.18.1.4 Equipment List and Specifications

The detailed specifications of the equipment and devices used for the hybrid PZT-SLDV system at USC VSHM laboratory are given in Table E.18-1. Data acquisition settings are shown in Table E.18-2.

Table E.18-1. Equipment/device specifications.

Equipment/device	Specifications
Polytec PSV-400-M2	2D scanning laser Doppler vibrometer with a frequency range up to 1 MHz with specific velocity decoders
PZT	Steminc 7-mm circular 0.5-mm thick piezoelectric transducers
Tektronix AFG3022C	2-channel arbitrary function generator with 1μHz to 25MHz
HSA 4014	High speed bipolar amplifier up to 1 MHz and 200 VA
Target Simply Balanced™ organic honey	Natural and organic honey blend performed as couplant
Albedo 100 Reflective Spray	a non-permanent, clear spray with light-reflective properties

E.18.1.5 Settings

Table E.18-2. Data collection settings.

Sampling frequency (MHz)	12.56 MHz
Spatial sampling interval (mm)	1 mm
Average	100
Velocity decoder	VD-07 10mm/s/V
Spray coating	20 layers

A three-count toneburst at 150 kHz amplified to 50 V_{pp} is used as excitation for each test. 2D area inspection is performed for both sides with different actuations. The spatial resolution is 1 mm. The inspection is performed with the setup as shown in Figure E.18-4. Since the specimen is curved, the inspection is not same as traditional SLDV scanning. The SLDV head is placed as shown in Figure E.18-4, and the scanning angle effect is not considered. 2D area inspection is performed with each actuation locations on both sides. For each inspection, the scanning area covers the accessible surface of the specimen: around 90 mm × 90 mm for both sides. For each side, the inspection area differs a little due to the curvature. Note that the scanning area is not identical to the real curved surface, and the measured wavefield is the shrink version of original wavefield in *x*-*z* plane due to the curvature.

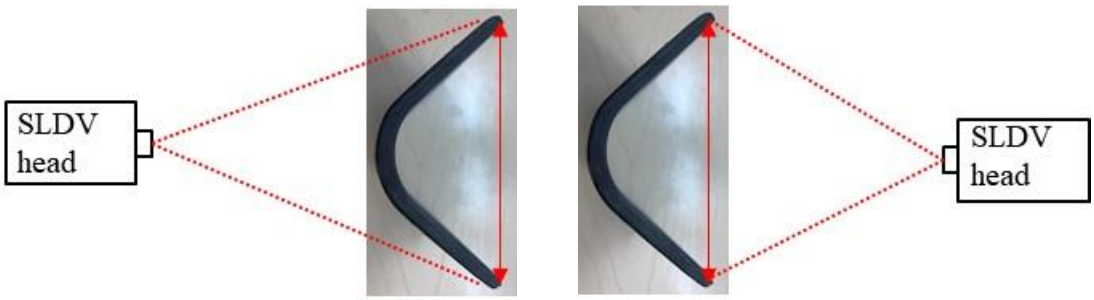

Figure E.18-4. Experimental setup (a) scanning schematic of outside surface, and (b) scanning schematic design of inside surface.

E.18.1.6 Inspection Results

Outside surface

2D area inspection is performed on the outside surface first. The 2D time-space wavefields are obtained, and the wavefields at 45 μs for W1 and W2 are plotted in Figure E.18-5a and Figure E.18-5b, respectively. One can see that the wave interaction with the defects. Two defects are detected and highlighted in black dash box and classified into two groups: Group-1 and Group-2. Group-1 might be closer to the outside surface so that the interaction is stronger (note SLDV measures surface particle velocity).

The energy map obtained from the wavefields is plotted in Figure E.18-6. In the energy map of W1, a rectangular shape defect with height around 6 mm is detected at $y \approx 80$ mm (Group-1). Another defect is detected at $y \approx 50$ mm (Group-2). These two defects exist along x direction with the same length as 60 mm. The left edge of the defects is identified as at around $x \approx 50$ mm through matching the real arc surface and the scanning area. In the energy map of W2, the same phenomenon is observed: a rectangle shape defect with height 6 mm is detected at the same height as W1 at $y \approx 80$ mm (Group-1), and Another defect is detected at $y \approx 50$ mm (Group-2). The right

edge of the defects is identified as at around $x \approx 110$ mm. The overall inspection results match the results observed in wavefields.

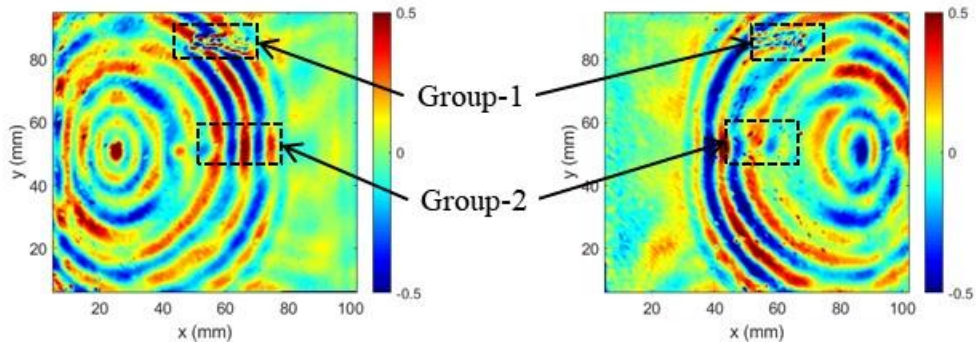

Figure E.18-5. Wavefield at 45 μs of outside surface: (a) actuator at O_1, and (b) actuator at O_2.

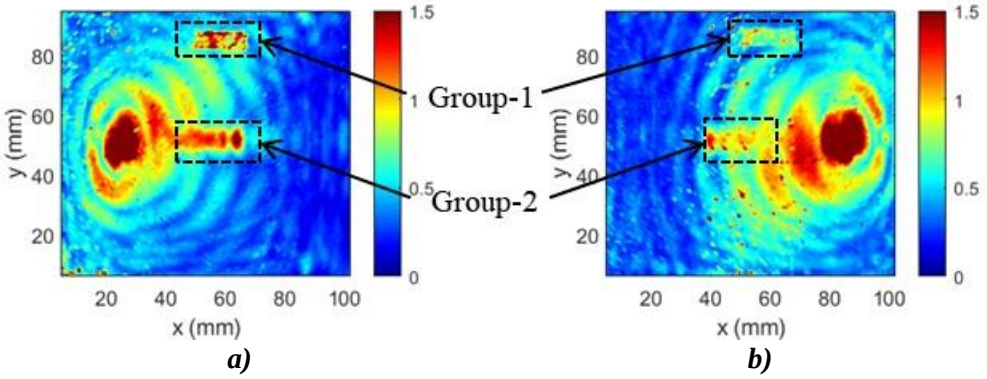

Figure E.18-6. Wavefield imaging of outside surface: (a) actuator at O_1, and (b) actuator at O_2.

From the inspection, it is concluded that Group-1 defects are located closer to outside surface, while Group-2 defects might be located around the middle layer of the composites since they are not clearly observed from either side. The defects are located around 50−110 mm along the arc surface with height around 6 mm.

Inside surface

On the inside surface, same 2D area inspection is performed. The 2D space wavefields at 45 μs for W1 and W2 are plotted in Figure E.18-7a and Figure E.18-7b, respectively. Strong wave interaction with the defects are observed, and four defects are detected and highlighted in black dash box. The detected defects are classified into two groups: Group-2 and Group-3. Group-3 might be closer to the inside surface since stronger wave interaction are observed in Group-3 defect area.

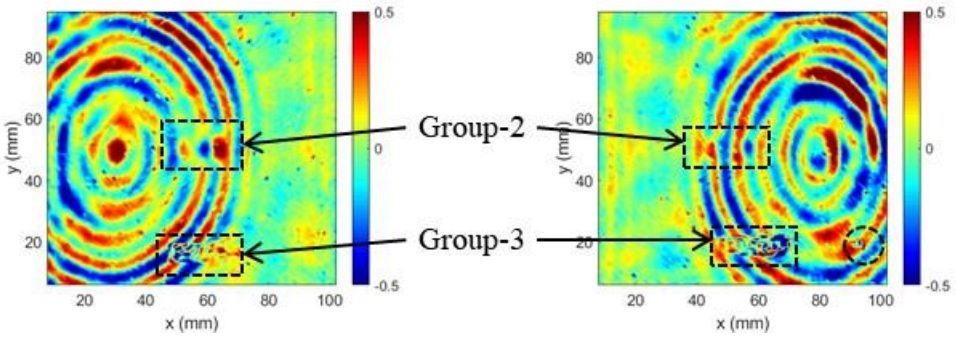

Figure E.18-7. Wavefield at 45 μs of inside surface: (a) actuator at O_1, and (b) actuator at O_2.

To visualize the defects, energy map of the wavefields are generated and plotted in Figure E.18-8. Similar defects are observed on the insider surface. In the energy map of W1, a rectangular shape defect with height around 6 mm is detected at $y \approx 20$ mm (Group-3). Another defect is detected at $y \approx 50$ mm (Group-2). These two defects exist along x direction with the same length as 60 mm. The left edge of the defects is identified as at around $x \approx 40$ mm through matching the real arc surface and the scanning area. In the energy map of W2, the same phenomenon is observed: a rectangle shape defect with height 6 mm is detected at the same height as W1 at $y \approx 20$ mm (Group-1), and Another defect is detected at $y \approx 50$ mm (Group-2). The right edge of the defects is identified as at around $x \approx 120$ mm. The overall inspection results match the results observed in wavefields.

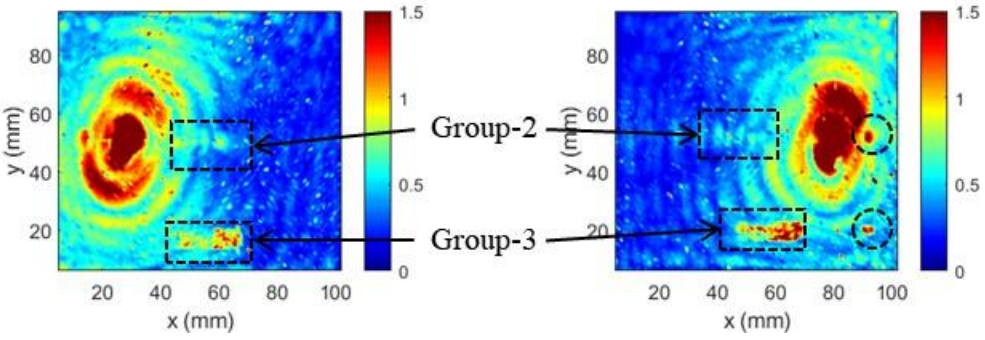

Figure E.18-8. Wavefield imaging of inside surface: (a) actuator at O_1, and (b) actuator at O_2.

From the inspection, it is concluded that Group-3 defects are located closer to the inside surface, while Group-2 defects might be located around the middle layer of the composites since they are not clearly observed from either side. The defects are located around 40–120 mm along the arc surface with height around 6 mm.

With the inspection results from the above sections, the detection summary of the defect is illustrated in Figure E.18-9. Nine defects are identified which are defined as Group-1, Group-2, and Group-3. Group-1 is located at close to the surface of outside while Group-3 is close to the surface of inside. Group-2 is located close to the middle layer of the specimen.

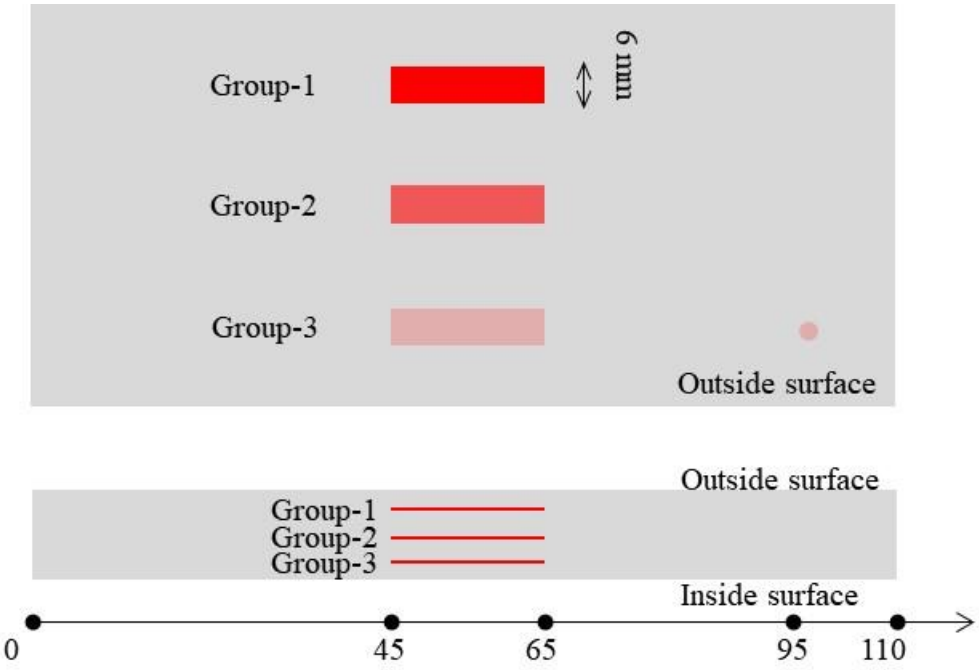

Figure E.18-9. Inspection summary of identified defects.

In conclusion, delamination on specimen 40D using the hybrid PZT-SLDV system is successfully detected and quantified even without material properties. The detailed rating of the system is shown in Table E.18-3. The defects are successfully detected so that five stars are rated for this part. For defect visualization, the defect shape is clearly identified, which is strip-like. Thus, this part gets five of five stars. For inspection time, the inspection time for one 2D scanning is around 50 minutes for areas illustrated in this test, which is fast. Thus, the inspection time gets four stars overall. Last, the actuator PZT is $3.60 per piece, which is cost effective. However, the SLDV is an expensive equipment, which costs $300,000 when purchasing. Thus, this part gets two stars. In the future, expensive SLDV can be replaced by customized fixed LDV and gantry system to reduce the system cost. Overall, this hybrid PZT-SLDV guided wave inspection is very robust in general with four out of five stars.

Table E.18-3. Hybrid PZT-SLDV guided wave inspection rating.

Hybrid PZT-SLDV guided wave inspection		
NASA-RP-10D Defect: delaminations	Rating	
	Detection:	★★★★★
	Defect visualization	★★★★★
	Inspection time:	★★★★☆
	Equipment cost:	★★☆☆☆
	Overall Performance:	★★★★☆

E.18.1.7 References

[1] Yu, L.; Leckey, C. A. & Tian, Z. (2013). “Study on crack scattering in aluminum plates with Lamb wave frequency–wavenumber analysis”, Smart Materials and Structures, Vol. 22, No. 6, pp065019, 2013.

[2] Tian, Z., Yu, L., & Leckey, C. (2015). “Delamination detection and quantification on

laminated composite structures with Lamb waves and wavenumber analysis", Journal of Intelligent Material Systems and Structures, Vol.26, No. 13, 2015, pp. 1723-1738.

[3] Guided wave inspection on specimen A1 (A1 report, submitted).

E.19 Specimen #19: NASA-RP-20D

Structure	Material	Details	Dimensions (inches)	Partner Methods	
Uni-ply (0/90/45)	IM7/8552	Radius Panel 2.0 inch Curve Rad with defects	4.5 × 2.5 × 4	USC	E.19.1 GWUT

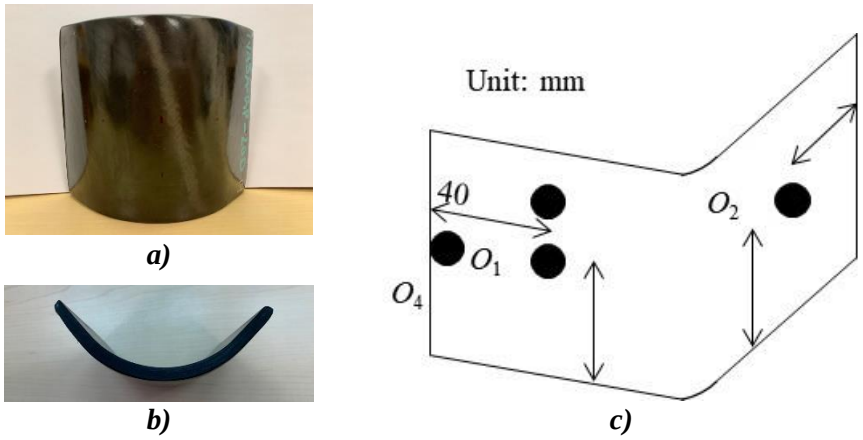

Figure E.19-1. Photographs of Specimen NASA-RP-20D. (a) overall view, (b) side view, and (c) specimen setup.

E.19.1 *Method: Guided Wave Ultrasound (GWUT)*

E.19.1.1 Partner: USC

E.19.1.2 Technique Applicability: ★★★

GWUT employs ultrasonic waves that propagate along waveguides by its boundaries, e.g. pipes, rods and plate-like structures, which allows waves propagate a long distance with little energy loss. GWUT shows advantage in many types of defect inspection, e.g. crack in metallic structures [1], and delamination in composite structures [2].

The Specimen NASA-RP-20D, (herein referred to as 20D), is inspected using hybrid PZT-SLDV GWUT method in this report. General information of 20D is illustrated below. The relative inspection, results and system rating are illustrated in the inspection results.

The front view and side view Specimen 20D are shown in Figure E.19-1a and Figure E.19-1b, respectively. The height of the specimen is 101 mm, and the thickness is around 7 mm. The length of the specimen outside surface is 140 mm as shown in Figure E.19-1c. The actuator is attached at O_1 and O_2 in order to inspect the specimen from different views. No other information about 20D is available to the inspectors.

E.19.1.3 Laboratory Set Up

The same hybrid PZT-SLDV system is employed for 20D inspection, where contact type PZT is used as actuator and SLDV as sensor to excite and receive guided waves in the testing plate (Lamb

waves) [1]. The overall setup also remains the same as reported previously and shown in Figure E.19-2 and Figure E.19-3 [3].

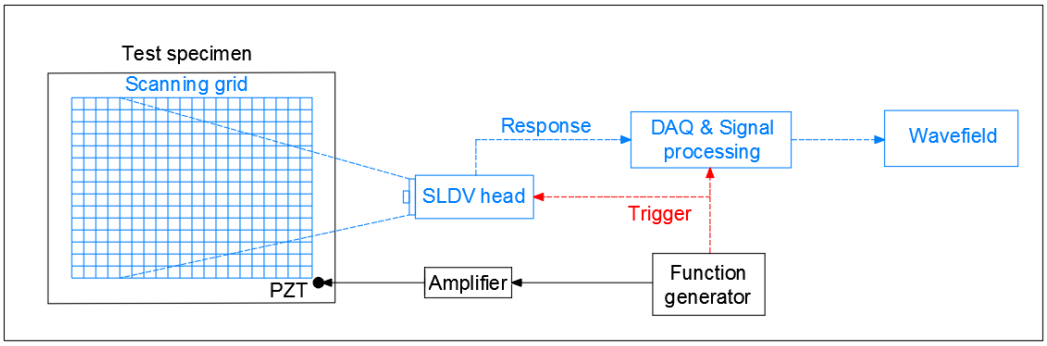

Figure E.19-2. Schematic design of the PZT-SLDV system.

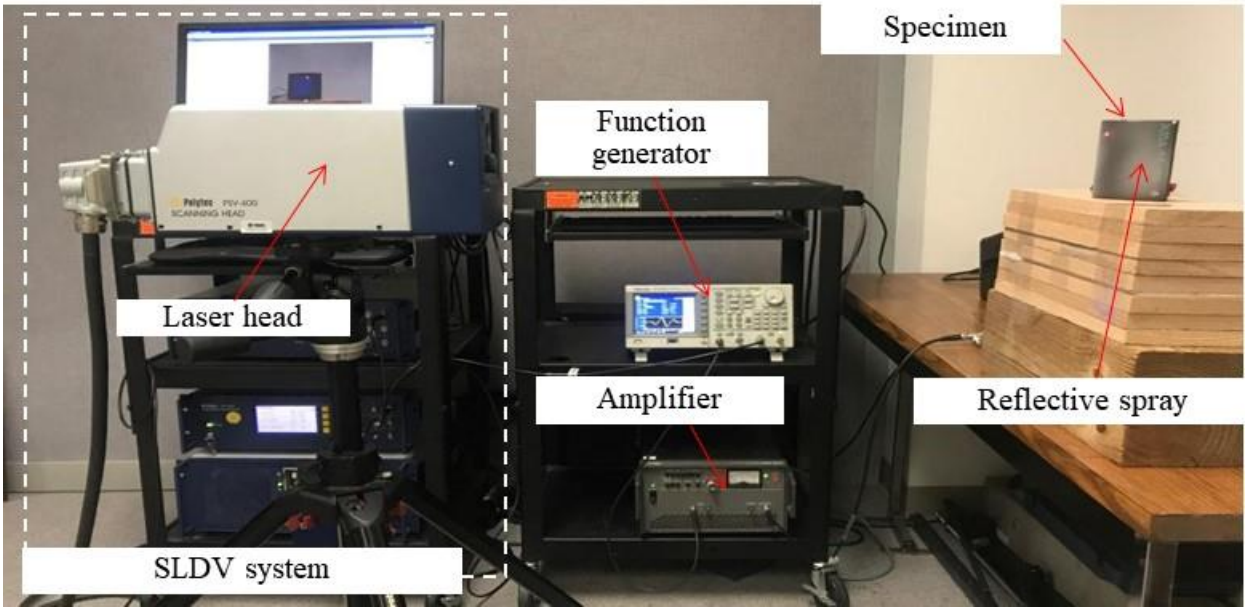

Figure E.19-3. Experimental setup of the PZT-SLDV system.

E.19.1.4 Equipment List and Specifications

The detailed specifications of the equipment and devices used for the hybrid PZT-SLDV system at USC VSHM laboratory are given in Table E.19-1. Data acquisition settings are shown in Table E.19-2.

Table E.19-1. Equipment/device specifications.

Equipment/device	Specifications
Polytec PSV-400-M2	2D scanning laser Doppler vibrometer with a frequency range up to 1 MHz with specific velocity decoders
PZT	Steminc 7-mm circular 0.5-mm thick piezoelectric transducers
Tektronix AFG3022C	2-channel arbitrary function generator with 1μHz to 25MHz
HSA 4014	High speed bipolar amplifier up to 1 MHz and 200 VA
Target Simply Balanced™ organic honey	Natural and organic honey blend performed as couplant
Albedo 100 Reflective Spray	a non-permanent, clear spray with light-reflective properties

E.19.1.5 Settings

Table E.19-2. Data collection settings.

Sampling frequency (MHz)	12.56 MHz
Spatial sampling interval (mm)	1 mm
Average	100
Velocity decoder	VD-07 10mm/s/V
Spray coating	20 layers

A three-count toneburst at 150 kHz amplified to 50 V_{pp} is used as excitation for each test. 2D area inspection is performed for both sides with different actuations. The spatial resolution is 1 mm. The inspection is performed with the setup as shown in Figure E.19-4. Since the specimen is curved, the inspection is not same as traditional SLDV scanning. The SLDV head is placed as shown in Figure E.19-4, and the scanning angle effect is not considered. 2D area inspection is performed with each actuation locations on both sides. For each inspection, the scanning area covers the accessible surface of the specimen: around 90 mm × 90 mm for both sides. For each side, the inspection area differs a little due to the curvature. Note that the scanning area is not identical to the real curved surface, and the measured wavefield is the shrink version of original wavefield in *x*-*z* plane due to the curvature.

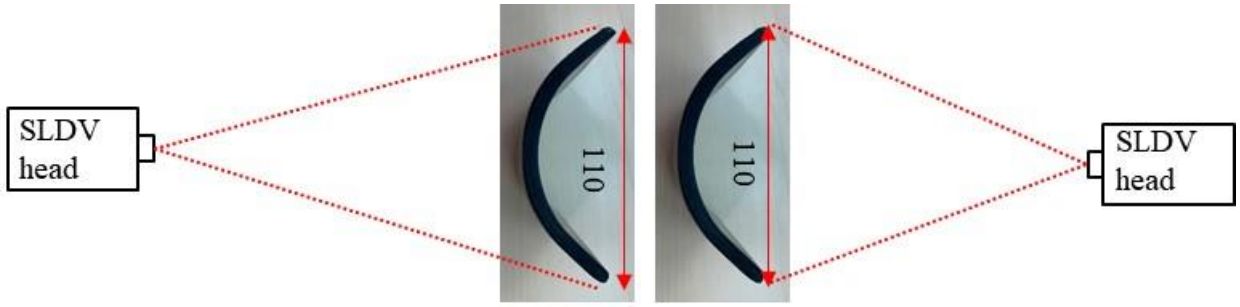

a) ***b)***

Figure E.19-4. Experimental setup (a) scanning schematic of outside surface, and (b) scanning schematic design of inside surface.

E.19.1.6 Inspection Results

Outside surface

2D area inspection is performed on the outside surface first. The 2D time-space wavefields are obtained, and the wavefields at 45 μs with actuation at O_1 and O_2 are plotted in Figure E.19-5a and Figure E.19-5b, respectively. One can see that the wave interaction with the defects. Two defects are detected and highlighted in black dash box and classified into two groups: Group-1 and Group-2. Group-1 might be closer to the outside surface so that the interaction is stronger (note SLDV measures surface particle velocity).

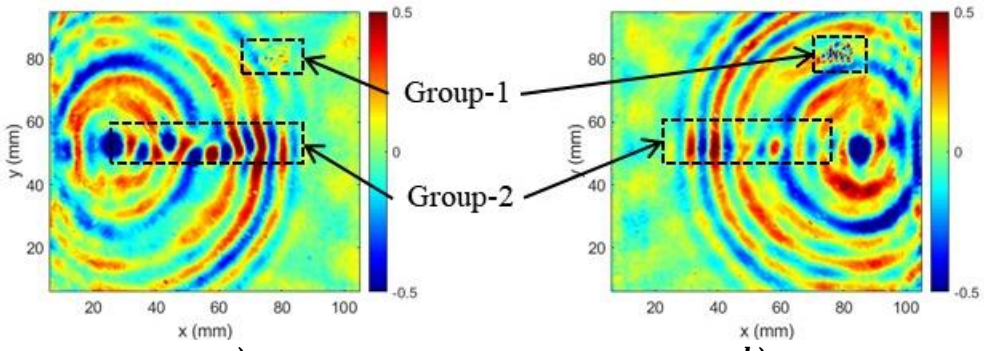

Figure E.19-5. Wavefield on inside at 45 μs of outside surface: (a) actuator at O_1, and (b) actuator at O_2.

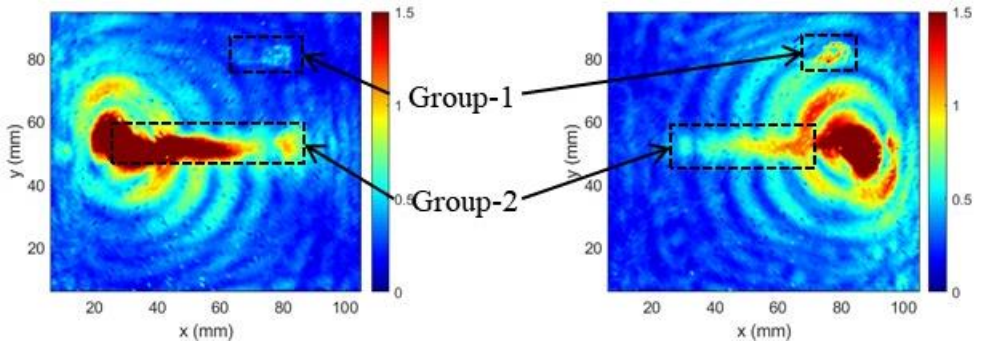

Figure E.19-6. Wavefield imaging of outside surface: (a) actuator at O_1, and (b) actuator at O_2.

The maximum amplitude image obtained from the wavefields is plotted in Figure E.19-6. In the wavefield image with actuation at O_1 (Figure E.19-6a), a rectangular shape defect with height around 6 mm is detected at $y \approx 80$ mm (Group-1). Another defect is detected at $y \approx 50$ mm (Group-2). Group-1 defect exists along x direction with from $x \approx 60$-80 mm. The range of Group-2 defect cannot be clearly identified ($x \approx 70$-80 mm approximately). In the wavefield image with actuation at O_2, the same phenomenon is observed.

Since Group-2 range along x direction is not clearly identified, another experiment with excitation at O_3 is performed. Note the excitation location has some distance to both Group-1 and Group-2 defect. The obtained wavefield at 35 μs and wavefield image are plotted in Figure E.19-7. Group-1 defect is detected in this case, and the location matches previous results. However, Group-2 defect is not obvious in both wave propagation and wavefield image. The reason can be that the interaction is very weak since waves came from oblique direction (O_3) instead of normal direction (O_2). In the future, excitation at O_4 can be performed to see if the better inspection results of Group-2 defect can be obtained.

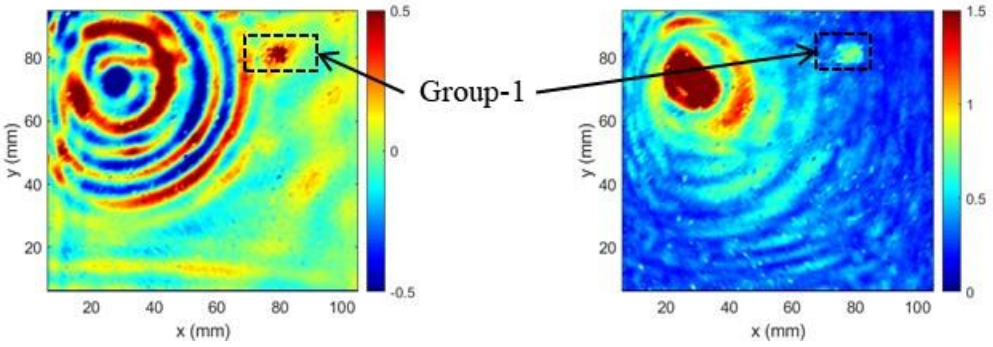

Figure E.19-7. Inspection results with actuator at O_3: (a) wavefield at 35 µs, and (b) wavefield image.

Inside surface

On the inside surface, same 2D area inspection is performed. The 2D space wavefields at 45 µs with actuation at O_1 and O_2 are plotted in Figure E.19-8a and Figure E.19-8b, respectively. Strong wave interaction with the defects are observed, and two groups of defects are detected and highlighted in black dash box. The detected defects are classified into two groups: Group-2 and Group-3. Group-3 might be closer to the inside surface since stronger wave interaction are observed in Group-3 defect area.

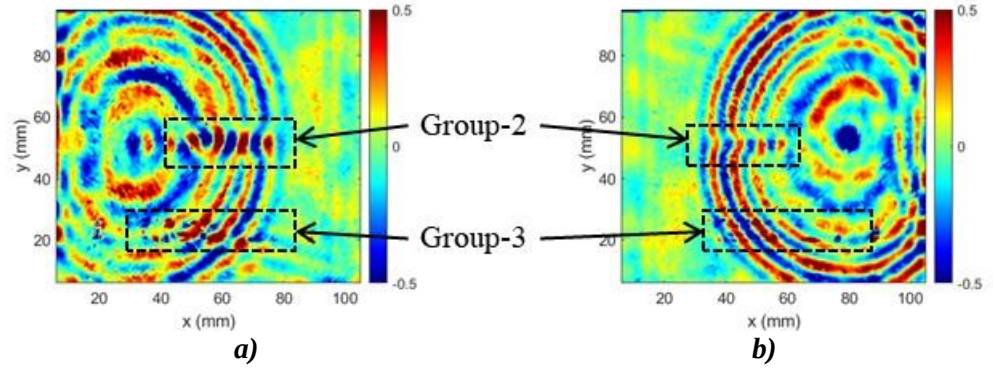

Figure E.19-8. Wavefield on inside at 45 µs of inside surface: (a) actuator at O_1, and (b) actuator at O_2.

To visualize the defects, wavefield images are generated and plotted in Figure E.19-9. Similar defects are observed on the insider surface. In the wavefield image with actuation at O_1, a large rectangular shape defect ($x \approx$ 30-80) with height around 6 mm and two small defects ($x \approx$ 20, 90) are detected at $y \approx$ 20 mm (Group-3). Another defect is detected at $y \approx$ 50 mm (Group-2) with unidentified range along x direction. In the wavefield image with actuation at O_2, the same phenomenon is observed for Group-3 defect. Group-2 defect is only detected at around $y \approx$ 30 mm.

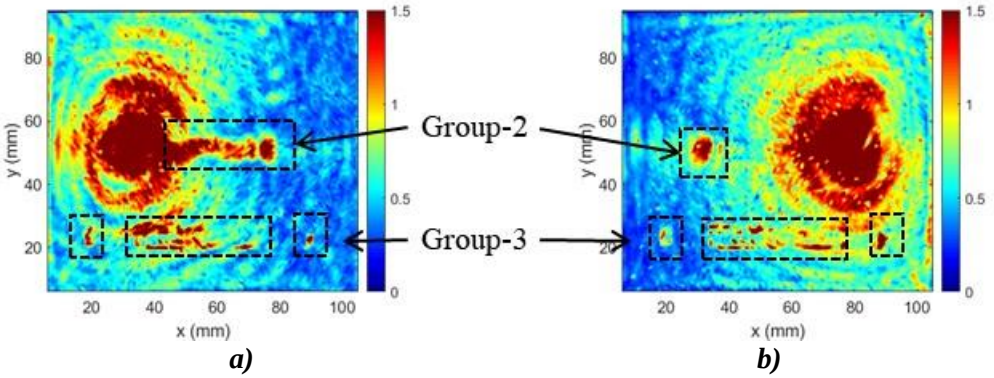

Figure E.19-9. Wavefield imaging of inside surface: (a) actuator at O_1, and (b) actuator at O_2.

From the inspection, it is concluded that Group-3 defects are located closer to the inside surface, while Group-2 defects might be located in the middle of the composites since they are not clearly observed from either side.

With the inspection results from the above sections, the detection summary of the defect is illustrated in Figure E.19-10. Five defects are identified which are defined as Group-1, Group-2, and Group-3. Group-1 is located at close to the surface of outside while Group-3 is close to the surface of inside. Group-2 is located close to the middle layer of the specimen. The figure is just for illustration purpose; please refer to the inspection results to see the defect size and locations.

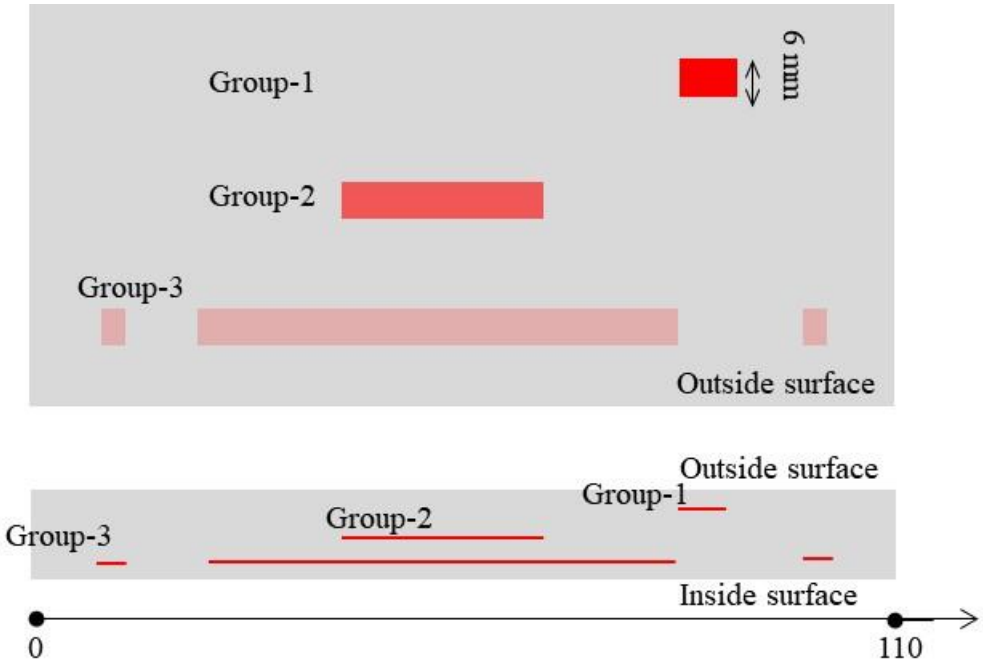

Figure E.19-10. Inspection summary of identified defects.

In conclusion, delamination on specimen 20D using the hybrid PZT-SLDV system is successfully detected and quantified even without material properties. The detailed rating of the system is shown in Table E.19-3. The defects are successfully detected so that five stars are rated for this part. For defect visualization, the large defect shape is clearly identified, which is strip-like, while the small defects and defects close to middle layer are not clearly identified. Thus, this part gets

four of five stars. For inspection time, the inspection time for one 2D scanning is around 50 minutes for areas illustrated in this test, which is fast. Thus, the inspection time gets four stars overall. Last, the actuator PZT is $3.60 per piece, which is cost effective. However, the SLDV is an expensive equipment, which costs $300,000 when purchasing. Thus, this part gets two stars. In the future, expensive SLDV can be replaced by customized fixed LDV and gantry system to reduce the system cost. Overall, this hybrid PZT-SLDV guided wave inspection is very robust in general with four out of five stars.

Table E.19-3. Hybrid PZT-SLDV guided wave inspection rating.

Hybrid PZT-SLDV guided wave inspection		
NASA-RP-20D Defect: delaminations	Rating	
	Detection:	★★★★★
	Defect visualization	★★★★☆
	Inspection time:	★★★★☆
	Equipment cost:	★★☆☆☆
	Overall Performance:	★★★★☆

E.19.1.7 References

[1] Yu, L.; Leckey, C. A. & Tian, Z. (2013). "Study on crack scattering in aluminum plates with Lamb wave frequency–wavenumber analysis", *Smart Materials and Structures*, Vol. 22, No. 6, pp065019, 2013.

[2] Tian, Z., Yu, L., & Leckey, C. (2015). "Delamination detection and quantification on laminated composite structures with Lamb waves and wavenumber analysis", *Journal of Intelligent Material Systems and Structures*, Vol.26, No. 13, 2015, pp. 1723-1738.

[3] Guided wave inspection on specimen A1 (A1 report, submitted).

E.20 Specimen #20: NASA-RP-40D

Structure	Material	Details	Dimensions (inches)	Partner Methods	
Uni-ply (0/90/45)	IM7/8552	4.0 inch radial inside curve, delams along curve and flat surfaces	4.5 × 1.25 × 6	NASA	E.20.1 PEUT
				USC	E.20.2 GWUT

Figure E.20-1. Photographs of Specimen #20: NASA-RP-40D.

E.20.1 *Method: Pulse-Echo Ultrasound Testing (PEUT)*

E.20.1.1 Partner: NASA

E.20.1.2 Technique Applicability: ★★★

E.20.1.3 Laboratory Setup

Immersion Ultrasonic Testing: NASA LaRC uses a custom designed single probe ultrasonic scanning system. The system has an 8-axis motion controller, a multi-axis gantry robot mounted above a medium-size water tank, a dual-channel, 16-bit, high-speed digitizer, and an off the shelf ultrasonic pulser receiver. The system can perform TTUT and PEUT inspections. TT inspection employs two aligned ultrasonic probes, one transmitter and one receiver, placed on either side of a test specimen. Pulse-echo inspection is a single-sided method where a single ultrasonic probe is both transmitter and receiver. In each method data is acquired while raster scanning the ultrasonic probe(s) in relation to a part. Figure E.20-2 shows a simplified block diagram of a scanning Pulse-echo inspection.

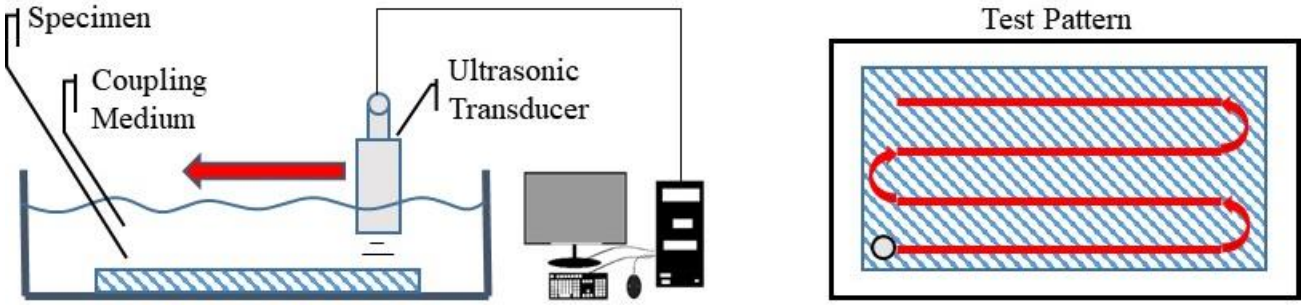

Figure E.20-2. Ultrasonic system components.

E.20.1.4 Equipment List and Specifications:

- Pulser/Receiver: Olympus 5073PR
- Digitizer: AlazarTech ATS9462, dual channel, 16 bit, 180 MS/s
- Sensor: Olympus 2” spherical focus immersion ultrasonic transducer
- Motion system: open looped stepper motor based X-YY-Z gantry robot
- Motion Controller: Galil DMC-4183
- Acquisition Software: FastScan, custom developed at NASA LaRC
- Signal Processing Software: DataViewer, custom developed at NASA LaRC

E.20.1.5 Settings

Table E.20-1. Data collection settings.

Resolution (horizontal) [in/pixel]	0.01
Resolution (vertical) [in/pixel]	0.02
Probe frequency [MHz]	10
Focal Length [in]	2
Array Dimensions [pixels]	311 × 301

The specimen is placed flat against the zero position of the tank raised above the glass bottom by several metal washers. The test probe is computer controlled and correlated to the position on the sample. It is also focused to a point 1 mm below the surface of the test material. The specimen

remains in place while the transducer follows a preprogrammed test grid across the surface as indicated in Figure E.20-2. At each point, ultrasonic data are collected from individual pulses. Larger step sizes between data collection result in lower image resolution. These data points are reconstructed into a data cube displaying spatial coordinates as time progresses. 2D reconstruction of the collection of ultrasonic responses create flattened slices at varying depths within the material.

E.20.1.6 Inspection Results

Specimen #20 is a curved profile with an inner radius of four inches fabricated from IM7/8552 with the objective of achieving large delaminations throughout the bulk of the sample. PEUT was performed on this specimen in NASA's immersion tank specified above.

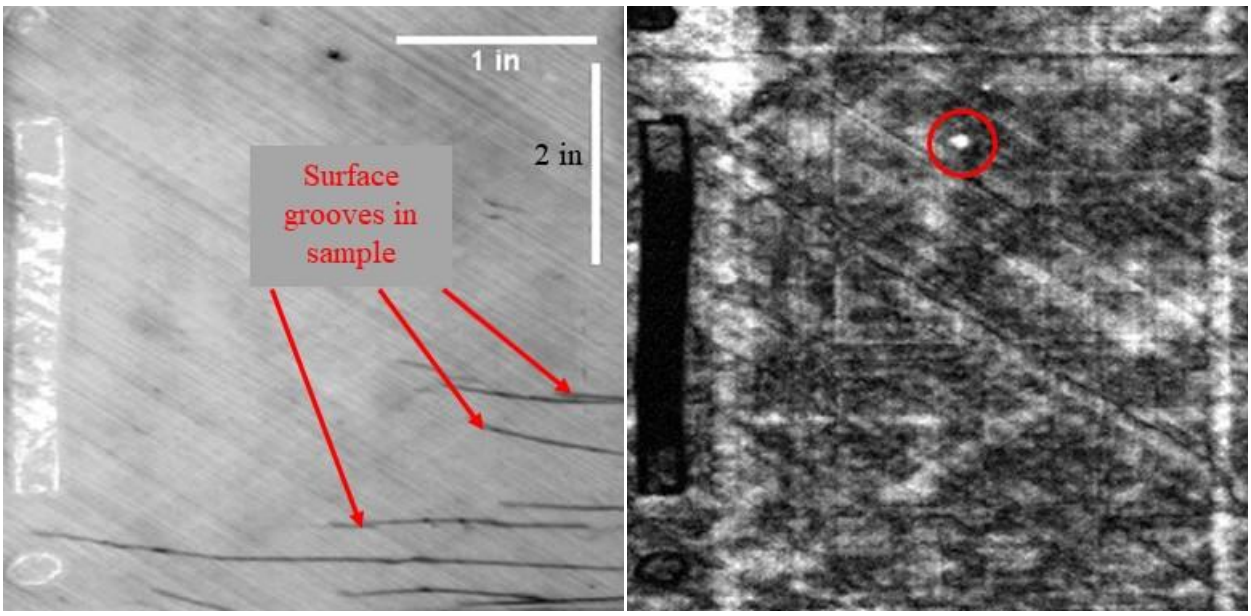

a) *b)*

Figure E.20-3. (a) Surface flaws and (b) near surface void

The data scan was performed in such a manner that the resolution in the vertical direction differs from that of the horizontal direction, hence the multiple scale bars occupying the same image. A large delamination appears just below the surface ply of the specimen in Figure E.20-3a. The delamination is a large impedance mismatch that causes a high-amplitude signal reflection within the specimen. Dark streaks in this image are low-amplitude surface reflections due to scattering from surface cracks. Figure E.20-3b highlights a small void within the sample. Delaminations are indicated at three depths; .046 inch, .625 inch, and 1.23 inches from left to right. The back surface reflection image, C-Scan, in Figure E.20-4b below displays a portion of the finadelamination and the acoustic shadow generated from the prior disbonds.

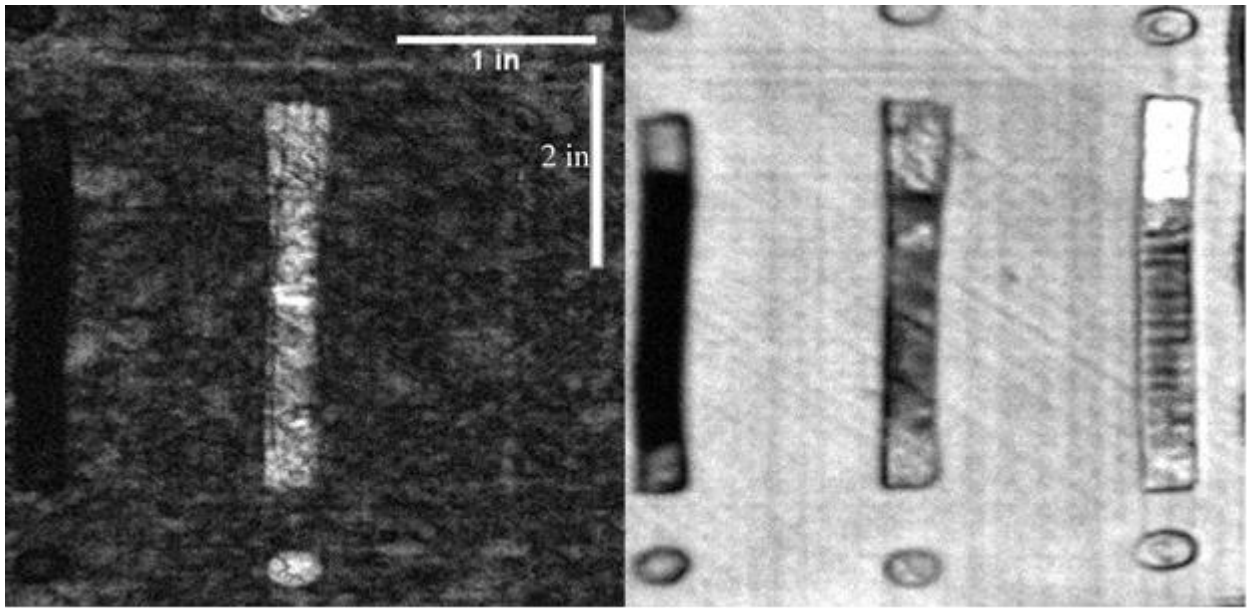

a) ***b)***

Figure E.20-4. (a) Interior delaminations and (b) back-surface reflection.

E.20.2 *Method: Guided Wave Ultrasound (GWUT)*

E.20.2.1 Partner: USC

E.20.2.2 Technique Applicability: ★★★

GWUT employs ultrasonic waves that propagate along waveguides by its boundaries, e.g. pipes, rods and plate-like structures, which allows waves propagate a long distance with little energy loss. GWUT shows advantage in many types of defect inspection, e.g. crack in metallic structures [1], and delamination in composite structures [2].

The Specimen, NASA-RP-40D (herein referred to as 40D), is tested using hybrid PZT-SLDV GWUT method in this report. General information of 40D is illustrated in the following paragraph. The relative inspection, results and system rating are illustrated in the inspection results.

The front view and side view Specimen 40D are shown in Figure E.20-5a and Figure E.20-5b, respectively. The height of the specimen is 101 mm, and the thickness is around 7 mm. The outside arc length of the specimen is 160 mm (predefined W1 and W2 with arc length 75 mm) as shown in Figure E.20-5c. No other information about 40D is available to the inspectors.

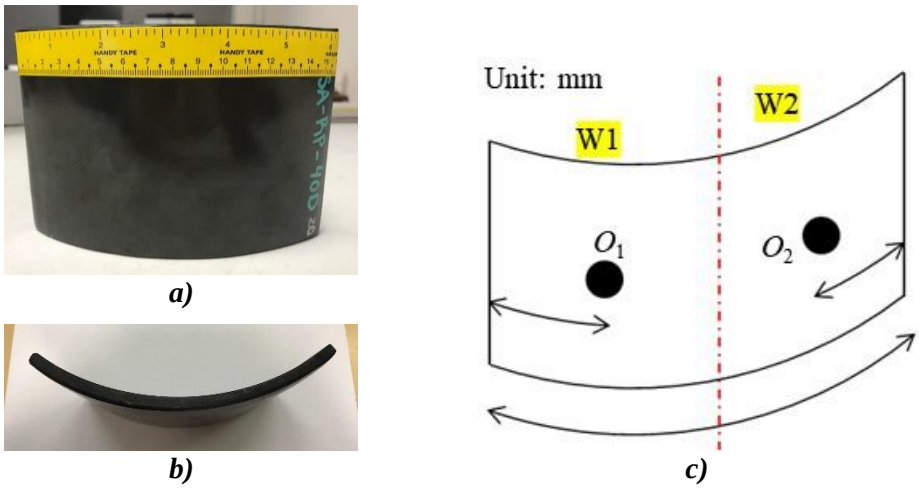

Figure E.20-5. Photographs of Specimen NASA-RP-40D. (a) Overall view, (b) side view, and (c) specimen setup.

E.20.2.3 Laboratory Set up

The same hybrid PZT-SLDV system is employed for 40D inspection, where contact type PZT is used as actuator and SLDV as sensor to excite and receive guided waves in the testing plate (Lamb waves) [1]. The overall setup remains the same as shown in Figure E.20-6 and Figure E.20-7 [3].

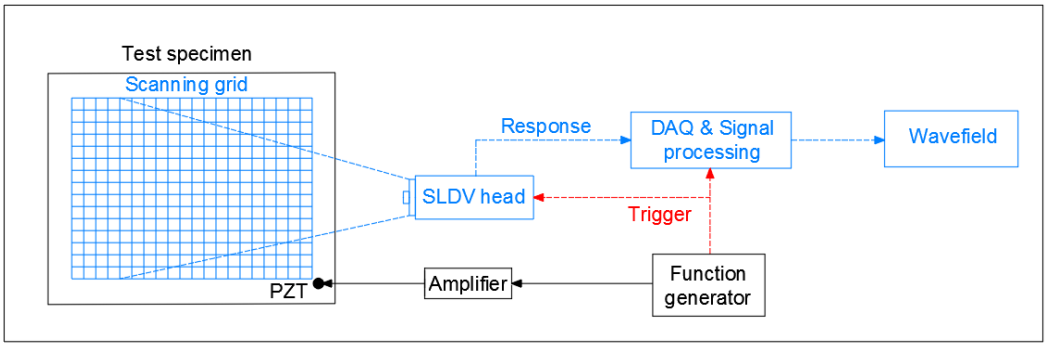

Figure E.20-6. Schematic design of the PZT-SLDV system.

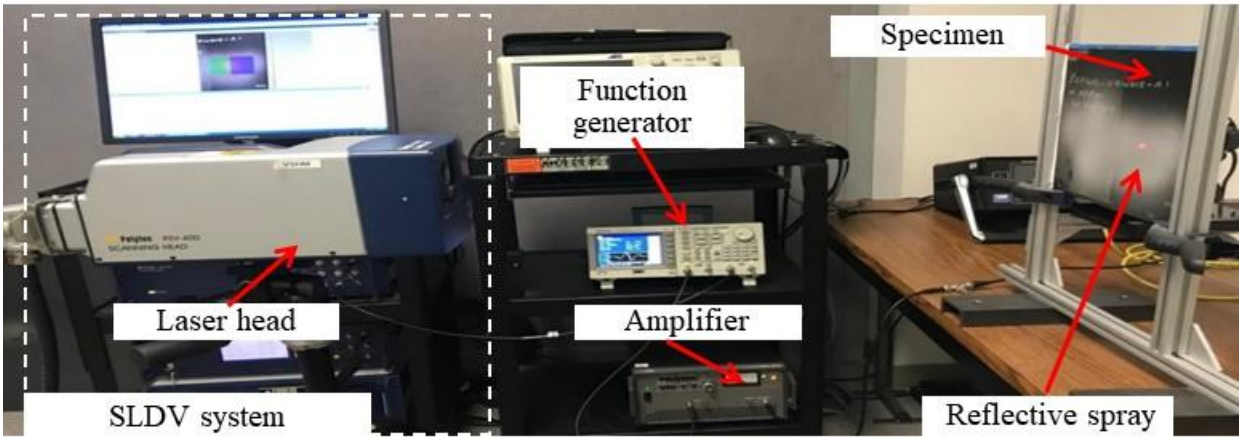

Figure E.20-7. Experimental setup of the PZT-SLDV system.

E.20.2.4 Equipment List and Specifications

The detailed specifications of the equipment and devices used for the hybrid PZT-SLDV system at USC VSHM laboratory are given in Table E.16-2. Data acquisition settings are shown in Table E.16-3.

Table E.20-2. Equipment/device specifications.

Equipment/Device	Specifications
Polytec PSV-400-M2	2D scanning laser Doppler vibrometer with a frequency range up to 1 MHz with specific velocity decoders
PZT	Steminc 7-mm circular 0.5-mm thick piezoelectric transducers
Tektronix AFG3022C	2-channel arbitrary function generator with 1μHz to 25MHz
HSA 4014	High speed bipolar amplifier up to 1 MHz and 200 VA
Target Simply Balanced™ organic honey	Natural and organic honey blend performed as couplant
Albedo 100 Reflective Spray	a non-permanent, clear spray with light-reflective properties

E.20.2.5 Settings

Table E.20-3. Data collection settings.

Sampling frequency (MHz)	12.56 MHz
Spatial sampling interval (mm)	1 mm
Average	100
Velocity decoder	VD-07 10mm/s/V
Spray coating	20 layers

The inspection is divided into two parts based on the predefined area as W1 and W2. A three-count toneburst at 150 kHz amplified to 50 V_{pp} is used as excitation for each test. 2D area inspection is performed for each part with spatial resolution 1 mm.

Since the specimen is curved, the inspection is not as traditional SLDV scanning. The SLDV head is placed normal to the actuator location, and the scanning angle effect is not considered. The actuator is attached at O_1 for W1 inspection and O_2 for W2 inspection as shown in Figure E.20-6c. 2D area inspection is performed at each wing (W1 and W2) on both sides. For each inspection, the scanning area covers the accessible surface of the inspected wing: around 90 mm × 90 mm for both wings. For each side, the inspection area differs a little due to the curvature. Note that the scanning area is not identical to the real arc surface, and the measured wavefield is the shrink version of original wavefield in *x-z* plane due to the curvature.

E.20.2.6 Inspection Results

Outside surface

2D area inspection is performed on the outside surface first. The 2D time-space wavefields are obtained, and the wavefields at 45 μs for W1 and W2 are plotted in Figure E.20-8a and Figure E.20-8b, respectively. One can see that the wave interaction with the defects. Four defects are detected and highlighted in black dash box and classified into two groups: Group-1 and Group-2. Group-1 might be closer to the outside surface so that the interaction is stronger (note SLDV measures surface particle velocity).

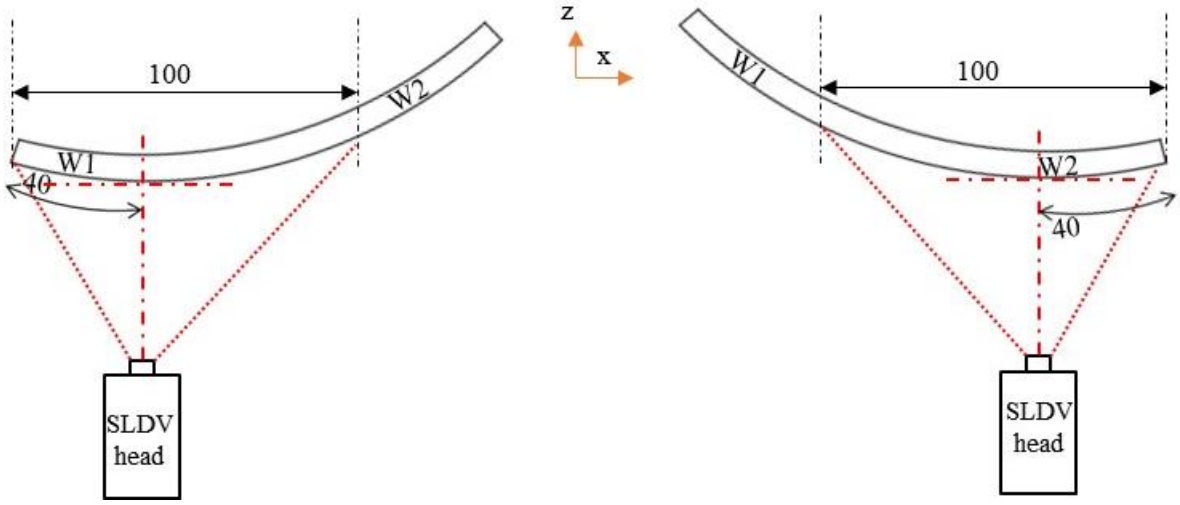

a) *b)*

Figure E.20-8. Experimental setup (a) scanning schematic design of W1 and (b) scanning schematic design of W2.

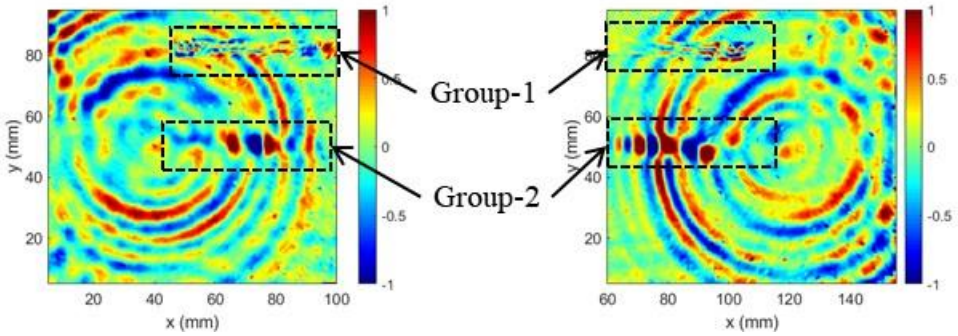

a) *b)*

Figure E.20-9. Wavefield on outside at 45 µs: (a) W1, and (b) W2.

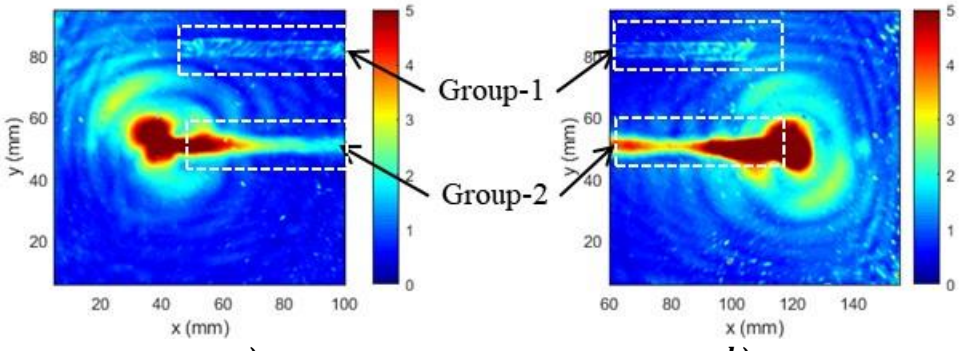

a) *b)*

Figure E.20-10. Energy map of outside surface: (a) W1, and (b) W2.

The energy map obtained from the wavefields is plotted in Figure E.20-10. In the energy map of W1, a rectangular shape defect with height around 6 mm is detected at $y \approx 80$ mm (Group-1). Another defect is detected at $y \approx 50$ mm (Group-2). These two defects exist along x direction with

the same length as 60 mm. The left edge of the defects is identified as at around $x \approx 50$ mm through matching the real arc surface and the scanning area. In the energy map of W2, the same phenomenon is observed: a rectangle shape defect with height 6 mm is detected at the same height as W1 at $y \approx 80$ mm (Group-1), and Another defect is detected at $y \approx 50$ mm (Group-2). The right edge of the defects is identified as at around $x \approx 110$ mm. The overall inspection results match the results observed in wavefields.

From the inspection, it is concluded that Group-1 defects are located closer to outside surface, while Group-2 defects might be located around the middle layer of the composites since they are not clearly observed from either side. The defects are located around 50−110 mm along the arc surface with height around 6 mm.

Inside surface

On the inside surface, same 2D area inspection is performed. The 2D space wavefields at 45 μs for W1 and W2 are plotted in Figure E.20-11a and Figure E.20-11b, respectively. Strong wave interaction with the defects are observed, and four defects are detected and highlighted in black dash box. The detected defects are classified into two groups: Group-2 and Group-3. Group-3 might be closer to the inside surface since stronger wave interaction are observed in Group-3 defect area.

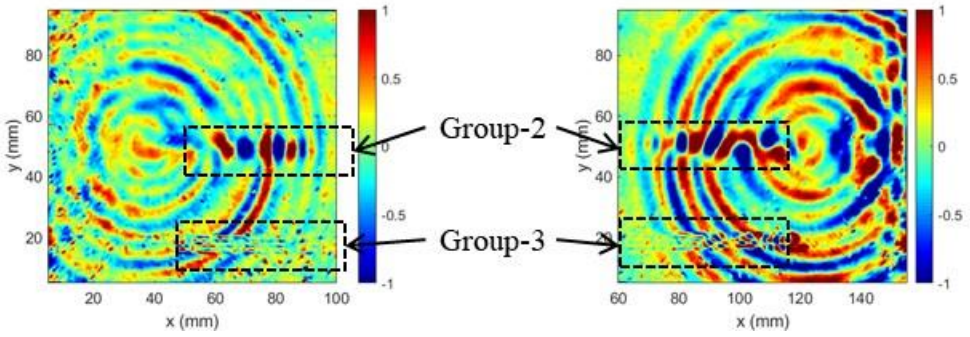

Figure E.20-11. Wavefield on inside at 45 μs: (a) W1, and (b) W2.

To visualize the defects, energy map of the wavefields are generated and plotted in Figure E.20-12. Similar defects are observed on the insider surface. In the energy map of W1, a rectangular shape defect with height around 6 mm is detected at $y \approx 20$ mm (Group-3). Another defect is detected at $y \approx 50$ mm (Group-2). These two defects exist along x direction with the same length as 60 mm. The left edge of the defects is identified as at around $x \approx 40$ mm through matching the real arc surface and the scanning area. In the energy map of W2, the same phenomenon is observed: a rectangle shape defect with height 6 mm is detected at the same height as W1 at $y \approx 20$ mm (Group-1), and Another defect is detected at $y \approx 50$ mm (Group-2). The right edge of the defects is identified as at around $x \approx 120$ mm. The overall inspection results match the results observed in wavefields.

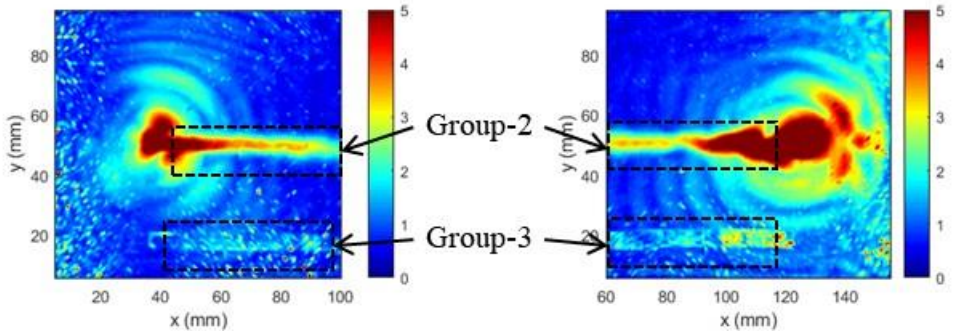

Figure E.20-12. Wavefield on inside at 45 µs: (a) W1, and (b) W2.

From the inspection, it is concluded that Group-3 defects are located closer to the inside surface, while Group-2 defects might be located around the middle layer of the composites since they are not clearly observed from either side. The defects are located around 40–120 mm along the arc surface with height around 6 mm.

E.20.2.7 Inspection Summary and Conclusions

With the inspection results from the above sections, the detection summary of the defect is illustrated in Figure E.20-13. Nine defects are identified which are defined as Group-1, Group-2, and Group-3. Group-1 is located at close to the surface of outside while Group-3 is close to the surface of inside. Group-2 is located close to the middle layer of the specimen.

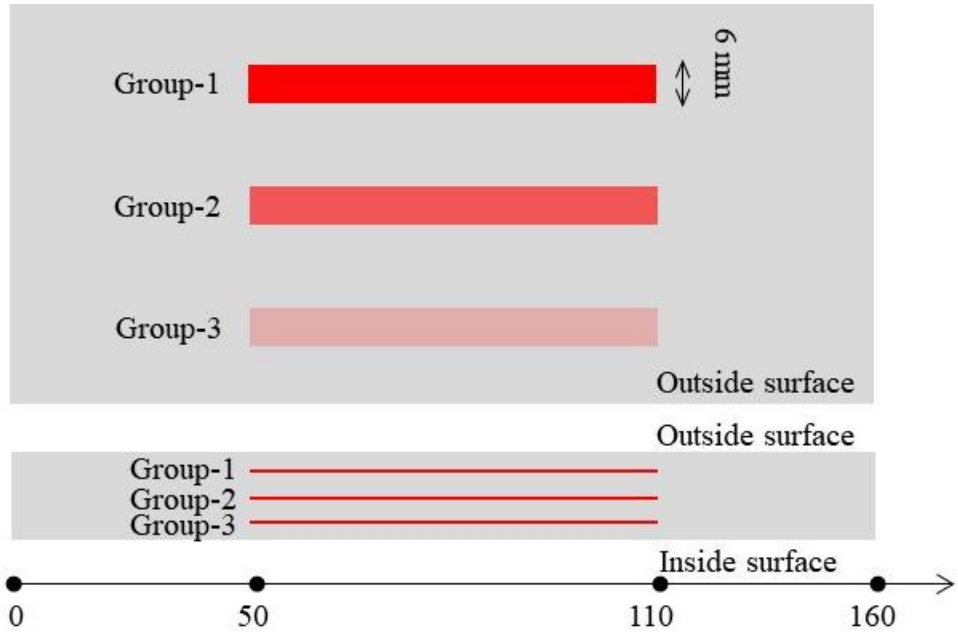

Figure E.20-13. Inspection summary of identified defects.

In conclusion, delamination on specimen 40D using the hybrid PZT-SLDV system is successfully detected and quantified even without material properties. The detailed rating of the system is shown in Table E.20-4. The defects are successfully detected so that five stars are rated for this part. For defect visualization, the defect shape is clearly identified, which is strip-like. Thus, this part gets five of five stars. For inspection time, the inspection time for one 2D scanning is around

50 minutes for areas illustrated in this test, which is fast. Thus, the inspection time gets four stars overall. Last, the actuator PZT is $3.60 per piece, which is cost effective. However, the SLDV is an expensive equipment, which costs $300,000 when purchasing. Thus, this part gets two stars. In the future, expensive SLDV can be replaced by customized fixed LDV and gantry system to reduce the system cost. Overall, this hybrid PZT-SLDV guided wave inspection is very robust in general with four out of five stars.

Table E.20-4. Hybrid PZT-SLDV guided wave inspection rating.

Hybrid PZT-SLDV guided wave inspection		
NASA-RP-40D Defect: delaminations	Rating	
	Detection:	★★★★★
	Defect visualization	★★★★★
	Inspection time:	★★★★☆
	Equipment cost:	★★☆☆☆
	Overall Performance:	★★★★☆

E.20.2.8 References

[1] Yu, L.; Leckey, C. A. & Tian, Z. (2013). "Study on crack scattering in aluminum plates with Lamb wave frequency–wavenumber analysis", *Smart Materials and Structures*, Vol. 22, No. 6, pp065019, 2013.

[2] Tian, Z., Yu, L., & Leckey, C. (2015). "Delamination detection and quantification on laminated composite structures with Lamb waves and wavenumber analysis", *Journal of Intelligent Material Systems and Structures*, Vol.26, No. 13, 2015, pp. 1723-1738.

[3] Guided wave inspection on specimen A1 (A1 report, submitted).

REPORT DOCUMENTATION PAGE

Form Approved
OMB No. 0704-0188

1. REPORT DATE *(DD-MM-YYYY)*	2. REPORT TYPE	3. DATES COVERED *(From - To)*
03/01/2020	Technical Memorandum	

4. TITLE AND SUBTITLE
Nondestructive Evaluation (NDE) Methods and Capabilities Handbook

Volume II Appendices - Appendix E Volume 1

5a. CONTRACT NUMBER

5b. GRANT NUMBER

5c. PROGRAM ELEMENT NUMBER

6. AUTHOR(S)
Howell, Patricia A. (Editor)

5d. PROJECT NUMBER

5e. TASK NUMBER

5f. WORK UNIT NUMBER
826611.04.07.02.02

7. PERFORMING ORGANIZATION NAME(S) AND ADDRESS(ES)
NASA Langley Research Center
Hampton, VA 23681-2199

8. PERFORMING ORGANIZATION REPORT NUMBER
L-21114

9. SPONSORING/MONITORING AGENCY NAME(S) AND ADDRESS(ES)
National Aeronautics and Space Administration
Washington, DC 20546-0001

10. SPONSOR/MONITOR'S ACRONYM(S)
NASA

11. SPONSOR/MONITOR'S REPORT NUMBER(S)
NASA/TM-2020-220568/Vol II/Pt 2

12. DISTRIBUTION/AVAILABILITY STATEMENT
Unclassified - Unlimited
Subject Category 37 Mechanical Engineering
Availability: NASA STI Program (757) 864-9658

13. SUPPLEMENTARY NOTES

14. ABSTRACT
This Handbook is a guidance document that facilitates the selection of appropriate Nondestructive Evaluation (NDE) techniques and provides recommended protocols for detecting and characterizing common flaw types in complex composite structures. It seeks to reduce the time required to develop qualified inspection processes for composite aircraft structures during the development, certification, and manufacturing phases by providing a reference that helps minimize trial and error and provides guidance on best practices, techniques, and settings, for specific flaw types and geometries.

15. SUBJECT TERMS
Nondestructive Evaluation; Inspection; Handbook; Composites; Carbon Fiber Reinforced Polymer; Ultrasound,; Thermography; X-ray CT

16. SECURITY CLASSIFICATION OF:			17. LIMITATION OF ABSTRACT	18. NUMBER OF PAGES	19a. NAME OF RESPONSIBLE PERSON
a. REPORT	b. ABSTRACT	c. THIS PAGE			STI Help Desk (email: help@sti.nasa.gov)
					19b. TELEPHONE NUMBER *(Include area code)*
U	U	U	UU	109	(443) 757-5802